ABSTRACT

CHEN, YUFEI. Structure Elucidation of Anthraquinone dyes by using Electrospray Quadrupole – Time-Of-Flight tandem Mass Spectrometry. (Under the direction of Dr. Nelson Vinueza Benitez).

Mass spectrometry (MS) has gained popularity in the field of analytical chemistry. With a combination of high sensitivity and high mass accuracy for both precursor and product ions in both MS and tandem MS modes, quadrupole–time-of-flight (Q-TOF) mass spectrometers have been widely accepted by scientific community as powerful and robust instruments for chemical analysis.

Anthraquinones are widely occurring in both nature and industries such as natural pigments, dyes, drug intermediates, and metabolic enzyme substrates. Anthraquinone dyes are commonly founds as commercial colorants used for dyeing polyester fibers with high wash fastness properties. Herein we use liquid chromatography mass spectrometry (LC-MS) to study several anthraquinone dyes from the Max Weaver Dye library in order to understand the different fragmentation pathways of this type of dye under tandem mass spectrometry conditions and to create a database of exact mass measurements and MS/MS spectra. In the future, the database would be potentially extended to cover not only dyestuff, but also drugs, alkaloids, ligands and metabolic enzymes.

Diode array detector (DAD) chromatograms and MS spectra were used to verify the formulas on the labels of the collected dyes. An HPLC method was to separate components of the dye samples and aided in avoiding the ion suppression. The protonated molecules formed upon positive-mode electrospray ionization (ESI) were subjected to several consecutive ion isolation and targeted collision-induced dissociation (CID) events, which revealed fragmentation patterns. These fragments facilitate the identification of amino, methylamino,

sulfamide (with aliphatic amine and/or aromatic amine), sulfone and thioether group, aromatic or aliphatic amine anthraquinones. Based on the CID results structure elucidation of anthraquinones has been established as way to identify group functionalities attached to this moiety.

© Copyright 2015 Yufei Chen

All Rights Reserved

Structure Elucidation of Anthraquinone dyes by using Electrospray Quadrupole – Time-Of-Flight tandem Mass Spectrometry

by
Yufei Chen

A thesis submitted to the Graduate Faculty of
North Carolina State University
in partial fulfillment of the
requirements for the degree of
Master of Science

Textile Chemistry

Raleigh, North Carolina

2015

APPROVED BY:

_____	_____
Nelson Vinueza Benitez Committee Chair	David Muddiman
_____	_____
Michael Bereman	Stephen Michielsen

BIOGRAPHY

Yufei Chen was born in Zhengzhou, Henan Province, China on March 13, 1989. He won first prize of the Chinese Chemistry Olympiad (Henan Province Division) in 2006 and was admitted by Zhejiang University, which boasts one of the top three chemistry departments in China. At Zhejiang University Yufei received his Bachelor of Engineering in Polymer Materials and Engineering in 2011. During his senior year of undergraduate studies, Yufei began to work on the synthesis of hyper-branched aggregation induced emission polymers. His experiences led him to pursue a Master of Science degree in Textile Chemistry at NC State, where his research is currently focused on dyes, biofuels, and mass spectrometry.

ACKNOWLEDGMENTS

Here I express my sincere gratitude to my advisor, Dr. Nelson R Vinueza, for his visionary guidance, insightful advices and genuine supports in my master program, without which this thesis would not have been accomplished to its least content. Additionally, I appropriate the help from Dr. David Hinks and Dr. Keith Beck. I would also like to thank our group member, Alexis Owens, Emily Lichtenberger, Kelsey Boes, Min Li and Nadia Sultana, all of whom have been always so supportive, helpful and collaborative to the research work described here. In addition, I really appreciate the kindness, care and helpful experience offered by COT officers Traci Figura and Amanda Padbury. Finally, I would like to thank my parents and girlfriend for their consistent support on my studies at NC State, and all those lovely close friends that I have made here in Raleigh, including Ju Dong, Xiaoyin Ji, Xiang Lu, Xiuzhu Fei and Jingyao, Li, just to name a few. Thanks for all their generous supports whenever and wherever I needed. I feel so blessed to meet all of them in my first two years exploration in United States.

TABLE OF CONTENTS

LIST OF TABLES

LIST OF FIGURES

1. Introduction

Anthraquinone derivatives are present in a variety of compounds—such as alkaloids, ligands, and dyes¬—making them an attractive field of research.[1-4] The identification of these compounds can be challenging due to the different matrices in which these compounds can be found. Mass spectrometry offers a fast and effective method of analysis due to its versatility and sensitivity. Different fragmentation paths of several anthraquinone derivatives were investigated using tandem mass spectrometry as a way to identify group functionalities attached to the anthraquinone moiety for more rapid identification.

The following literature review will discuss the history and principles of mass spectrometry, as well as the coupled separation technique of liquid chromatography. A hybrid instrument such as this provides a high degree of molecular structure information in contrast to current optical and chromatographic dye analysis techniques.

Verification of selected dyes will be performed by analyzing DAD chromatography and MS spectra. MS/MS events on isolated ions will be performed. By using these results, fragmentation pathways from different functionalities will be learned and structure elucidation will be established.

2. Literature Review

2.1 Mass spectrometry (MS)

2.1.1 Brief History of MS

In the simplest terms, mass spectrometry contains two parts: ion source and mass analyzer.

The ion source generates gas-phase ions from analytes—organic or inorganic. These ions are separated by their different mass-to-charge ratios (m/z) and then detected qualitatively or quantitatively by their respective m/z and abundance. The analytes can be ionized by electrons, photons, excited atoms, or electrostatically charged droplets. Ions can consist of single ionized atoms, clusters, molecules, or their fragments or associates, depending on the ionization method. In mass analyzer, ion separation is affected by electric and magnetic fields. These diverse types of ion sources and mass analyzers are based on different principles and therefore have different performance characteristics adapted to different scenarios and needs. Hybrid apparatus can combine those different performance characteristics offered by various types of analyzers into one mass spectrometer to provide a unique applications for different fields of research.

Today, MS is mostly under the purview of the analytical chemistry field. In 1886, Eugen Goldstein discovered that tubes with a perforated cathode emit a glow at the cathode end. Goldstein concluded that in addition to the already-known cathode rays—later recognized as electrons moving from the negatively charged cathode toward the positively charged anode—there is another ray that travels in the opposite direction. Because these latter rays passed through the holes, or channels, in the cathode, Goldstein called them Kanalstrahlen, or canal rays.[5] Canal rays were composed of positive ions which were converted from the residual gas inside the tube. Wihelm Wien, a student of Hermann von Helmholtz, found that strong electric or magnetic fields deflected the canal rays, and in 1899 he constructed a device with parallel electric and magnetic fields that separated the positive rays according to their charge-to-mass ratio (Q/m).[6] Wien found that the charge-to-mass ratio depended on the nature of the gas in the

discharge tube. In the 1900s, Wien's work was improved by J. J. Thomson who heightened the vacuum inside the tube and created the mass spectrograph.[7] Thomson's device was able to actually measure *Q/m* of the particles (electrons) that comprised cathode rays, which indirectly determined the mass of an electron.[8]

Developments of mass spectrometers continued over several decades leading to the discovery of new isotopes, as well as their accurate masses and relative abundances.[9] By the 1940s, chemists realized mass spectrometry's potential and it was established as an analytical tool, mostly for quantitative analysis.[8] Time-of-flight (TOF) mass analyzers were developed in 1946. Other developments of mass analyzers include ion cyclotron resonance (ICR) in 1948,[9] quadrupole and ion traps in 1953,[9] and orbitrap in the 2005.[10] M. A. Baldwin and F. W. McLafferty started to utilize a new type of instruments which coupled HPLC with mass spectrometers in the 1970s. Their goal was to combine sample separation and mass analysis.[11]

Typically, in a mass spectrometry experiment, a sample, which could be solid, liquid, or gas, is ionized by an ion source. These ions are then separated by their different mass-to-charge ratio. The ions are detected by a mechanism capable of detecting charged particles. Results are displayed as spectrum of the relative abundance of ions detected as a function of the mass-to-charge ratio. The atoms or molecules in the sample can be identified by correlating known masses to the identified masses or through a characteristic fragmentation pattern.

2.1.2 Quadrupole Mass Analyzer

A quadrupole mass analyzer is a combination of four hyperbolically or cylindrically shaped rod electrodes extending in the z-direction and mounted in a square configuration

(Figure 1).[12] The pairs of opposite rods (A and A or B and B) are each held at the same potential which is composed of a Direct Current and an Alternating Current component.

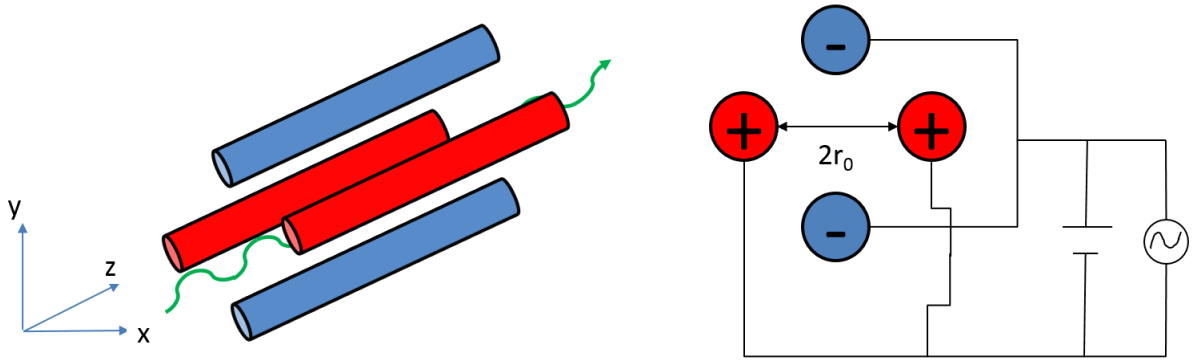

Figure 1 Cross section of a quadrupole for the cylindrical approximation

As a mass analyzer, quadrupoles operate with both radio frequency (RF) and direct current (DC) voltage components applied to the rods. The reduced Mathieu parameters q_M and a_M are used to characterize the amplitudes of both components:[13]

$$q_M = \frac{4eV}{(m/z)\omega^2 r_0^2}, \; a_M = \frac{8eU_{dc}}{(m/z)\omega^2 r_0^2} \quad (1)$$

where e is the charge of an electron, V and ω are the amplitude and angular frequency of the RF voltage, respectively. U_{dc} is the value of the DC voltage, and r_0 is the inscribed radius of the quadrupole. Under normal (mass-analyzing) operational conditions, only ions within a narrow m/z window are transmitted. This is the RF-only operational mode (a_M=0). Quadrupoles can also serve as either high-mass or low-mass filters for ions with m/z values above or below a certain cut-off value, depending on how the voltages are tuned.[14]

2.1.3 Time-of-Flight Mass Analyzer

The first time-of-flight (TOF) mass analyzer was developed in 1946 by W. E. Stephens.[15] A TOF operates under a simple principle demonstrated by its conspicuous long flight tube: ions are accelerated at same time by electric field with acceleration voltage U_a into the long flight tube, a field-free region. Potential energy obtained from U_a are equal among all ions and will be converted to kinetic energy (KE):

$$\mathrm{KE}=\frac{1}{2}mv^2 \quad (2)$$

where m is the mass and v is the velocity. Since mass and velocity are inversely proportional, the smaller the mass the faster the ion travels. Therefore, the lower mass ions will arrive at the detector earlier than the higher mass ions.

To compare two ions with different m/z, they must be accelerated at same time or a sufficiently short time interval. This is a difficult demand and brought forth the advent of the pulsed ion source, which can be realized either by pulsing ion packages out of a continuous beam or more conveniently by employing a true pulsed ionization method.[12]

Early TOFs were linear, which means ions are accelerated towards the flight tube to enter into a field-free region were they separated by their velocities before reaching the detector positioned at the other extremity of the flight tube. This linear TOF has a low resolving power due to initial spreads in the time, space and kinetic energy (KE) distributions of ions. (This applies only when U_a is constant, which is known as continuous extraction).Higher values of U_a (10-30 kV) minimize the contribution of the KE spread, but other factors still limit the

resolving power.(Figure 2 shows effects and reasons)[16]

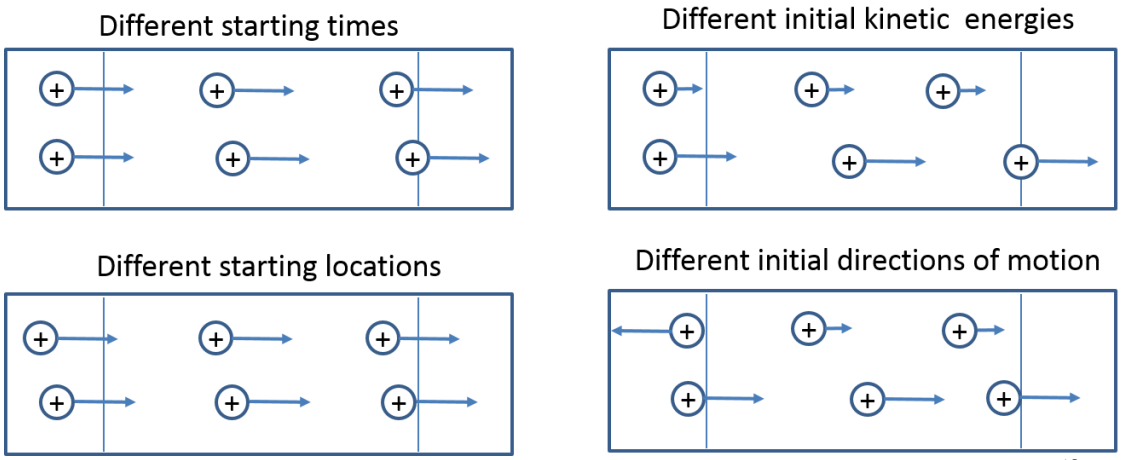

Figure 2 Effects of initial time, space, and kinetic energy distributions on mass resolution in TOF-MS.[16]

To improve the resolving power of TOF, Mamyrin devised the reflectron in 1994.[17] The reflectron acts as an ion mirror that focuses ions of different kinetic energies in time. A simple reflectron consist of a retarding electric field located behind the field free drift region opposed to the ion source. In practice, a reflectron is comprised of a series of ring-shaped electrodes at increasing potential. The reflection voltage U_r is set to about 1.05–1.10 times the acceleration voltage U_a in order to ensure that all ions are reflected within the homogeneous portion of the electric field of the device (Figure 3). The ions penetrate the reflectron until they reach zero kinetic energy and are then expelled from the reflectron in the opposite direction. The kinetic energy of the leaving ions remains unaffected, however their flight paths vary according to their differences in kinetic energy. Ions carrying more kinetic energy will fly deeper into the decelerating field, and thus spend more time within the reflectron than less energetic ions. Thereby, the reflectron effects a correction in time- of-flight that substantially improves the resolving power of the TOF analyzer.[16,18-20] In addition, the reflectron provides (imperfect)

focusing with respect to angular spread of the ions leaving the source and it corrects for their spatial distribution.[17,19] Adjusting the reflectron at a small angle with respect to the ions exiting from the source allows the reflectron–detector to be placed adjacent to the ion source (Mamyrin design).[21]

The ability of the reflectron to compensate for the initial energy spread of ions largely increases the resolving power of TOF. The resolution of a reflectron-TOF is better than a common linear TOF.

Figure 3 Principle of operation of reflectron

After the development of reflectron, the TOF has the following advantages: 1. High mass range, according to its principle, the m/z range is unlimited;[22] 2. Fast sacnning, complete mass spectrum is obtained within several microseconds; 3. High sensitivity; 4. The TOF instrument design and construction is comparatively simple and inexpensive to an ICR and orbitrap; 5. Recent instruments allow for accurate mass measurements and tandem MS experiments.[23]

2.1.4 Q-TOF Mass Spectrometry

As a combination of high sensitivity and high mass accuracy for both precursor and

product ions in both MS and tandem MS modes, quadrupole–time-of-flight (Q-TOF) mass spectrometers have been widely accepted by scientific community as powerful and robust instruments with unique capabilities with ion sources such as electrospray ionization (ESI), matrix-assisted laser desorption ionization (MALDI) and atmosphere pressure chemical ionization (APCI).

Schematic of a Q-TOF is presented in Figure 4. Samples are ionized from an ambient ion sources, such as ESI or APCI, and ions travel through an ion guide (Figure 4) into a quadrupole, where ions can be selected for tandem mass spectrometry experiments at the collision cell. The octopole ion guide helps to focus on the ions entering the instrument and as well as the hexapole. Octopole and hexapole provides both radial and axial collisional damping of ion motion. The ions are thermalized in collisions with neutral gas molecules, reducing both the energy spread and the beam diameter and resulting in better transmission into and through both the quadrupole[24] and TOF[25] analyzers. After leaving the hexapoles, ions are re-accelerated in the axial direction to the necessary energies with near-thermal energy spreads.

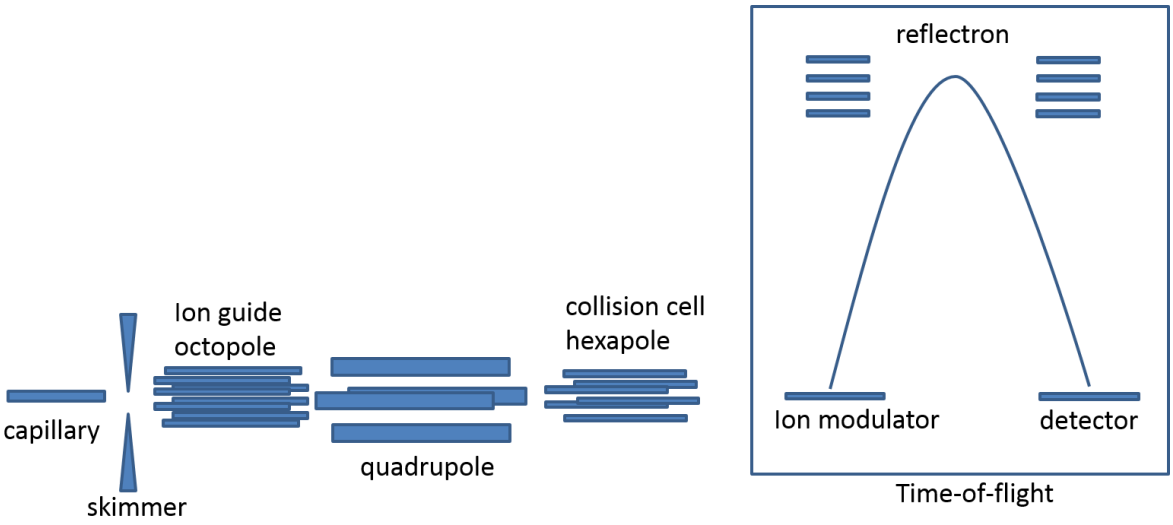

Figure 4 Quadrupole time-of-flight mass analyzer schematic

For MS/MS, quadrupole is operated in the mass filter mode to transmit only the parent ion of interest. The target ion is then accelerated before it enters the collision cell (hexapole), where it undergoes collision induced dissociation (CID) after the first few collisions with neutral gas molecules (usually argon or nitrogen). The resulting fragment ions (in addition to the remaining parent ions) are collisionally cooled and focused.

2.1.5 Electrospray Ionization

In 1984, Masamichi Yamashita and John Fenn developed a new ionization technique which was Electrospray ionization (ESI). This soft method allows less fragmentation or even no fragmentation during ionization.[26] Now, ESI has become the most widely used ionization technique due to its ability to be applicable for a vast variety of analytes such as inorganic and organic compounds. Due to its multiple-charged feature, polymers, lipids, peptides and proteins with high molecular mass are able to be ionized. In addition, ESI allows coupling with

liquid chromatography enhancing the field of MS analysis.

During the ESI process, three major steps are required to generate ions in gas from electrolyte solution: (a) The production of charged droplets at the electrospray capillary tip; (b) Shrinkage of the charged droplets due to solvent evaporation and Rayleigh fissions(also called Coulomb explosion); (c) the actual mechanism by which gas phase ions are produced from these droplets. The stages (a) to (c) occur in the atmospheric pressure region of the apparatus (see Figure 5).

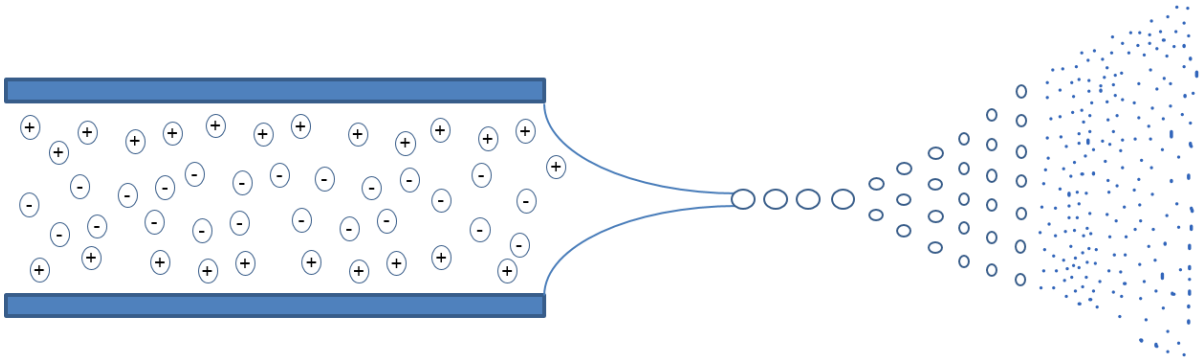

Figure 5 Illustration of major processes in the atmospheric pressure region of an ESI ion source run in the positive ion mode.

In positive mode, the electric field, which is near the spray capillary tip, will polarize the solution. Under this polarization influence of the electric field, the solution will be sufficiently conducting. Then the positive ions in the solution will move to the surface of the meniscus and negative ions will move away from the meniscus. The downfield forces due to the polarization cause a distortion of the meniscus into a cone pointing downfield. The increase of surface due to the cone formation is resisted by the surface tension of the liquid[27]. This liquid cone is named as Taylor cone.[28] The liquid cone tip becomes unstable if the electric field is high enough.

Therefore, a fine jet emerges from the cone tip. The surface of the jet is charged by an excess of cations. The repulsion between the charges on the jet causes the jet to break up into small charged droplets.[29]

The charged droplets will then shrink due to solvent evaporation while the charge remains constant. The energy required for the solvent evaporation is provided by the thermal energy of the ambient gas, air at atmospheric pressure in most cases. As the droplet gets smaller the repulsion between the charges at the surface increases, and at a certain droplet radius, this repulsion overcomes the cohesive force of the surface tension. An instability results and leads to fission of the droplet that typically releases a jet of small, charged progeny droplets. The condition for the instability, also called Rayleigh fission or Coulomb explosion, is given by the Rayleigh equation[30]:

$$Q_{Ry} = 8\pi(\varepsilon_0 \gamma R^3)^{\frac{1}{2}} \qquad (3)$$

where Q_{Ry} is the charge on the droplet, γ is the surface tension of the solvent, R is the radius of the droplet, and ε_0 is the vacuum permittivity.

Droplets at constant charge will experience the Rayleigh fission at or near the Rayleigh limit which is provided by equation(2), and then emit a jet of small, mono disperse charged product droplets. This shrinkage process has been confirmed by a number of experiments.[31-33] The loss of mass on fission is less than 1% of the parent droplet but the loss of charge is much larger, that is, some 15–25% of the charge of the parent droplet.[34]

Having repeated Rayleigh fissions, the parent droplets become smaller and smaller, and

eventually will convert to very small charged droplets which are the precursors of the gas-phase ions. The mechanisms by which the gas phase ions are produced from the very small ‘‘final’’ droplets is still not cleared. Two main assumptions are provided.

Malcolm Dole developed the charge residue model (CRM) in 1968.[35] The CRM assumes that the surface area of parent droplets decreases due to collisions with heated drying gas and/or heated capillary. Figure 6 presents the CRM.

As the parent droplet reduces in size, the charges on the surface move closer together, this results in Rayleigh fission. The offspring droplets that are formed from the parent droplet further reduce in size through the evaporation of solvent molecules. Each offspring droplet contains one analyte molecule. As the solvent molecules evaporate from the offspring droplets, charge is deposited onto the surface of the analyte, thus producing gas-phase ions. The CRM applies by default to large molecules (MDa) since each droplet is only able to contain one molecule.

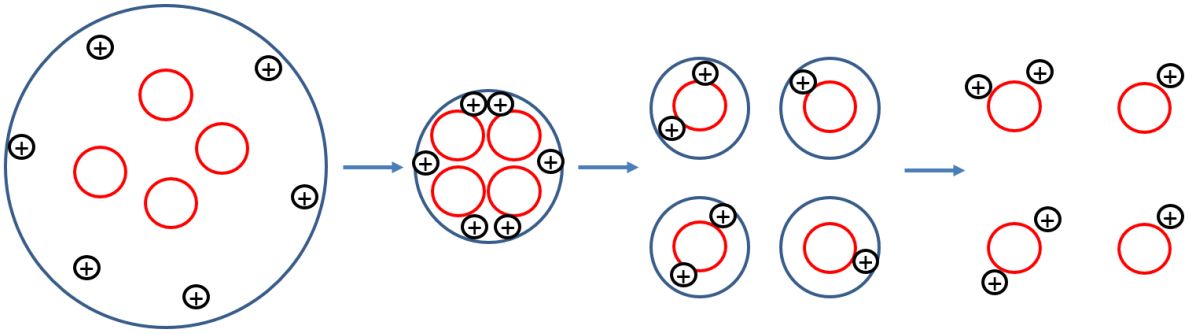

Figure 6 Charge residue model schematic

The Charged Residue Mechanism works well for macro molecules. It has allowed quantitative predictions of the protein charge state in the gas phase using a simple correlation

between charge state and protein mass and is well supported for proteins of widely varying mass.[34]

The ion evaporation model (IEM) was proposed by Iribarne and Thomson in 1976.[36] Like the CRM, the IEM assumes the evaporation and dissociation of parent droplets into offspring droplets. As the radius of the offspring droplet continues to decrease, the charge density and electric field increase.[9] The surface charge density is sufficiently lower than the Rayleigh limit, which causes the ejection of an ion from the offspring droplet instead of droplet dissociation. Figure 7 presents the IEM schematic. In MS experiments, the IEM is well-supported for small ions.[37] However, unlike the CRM, it does not apply for very large ions.

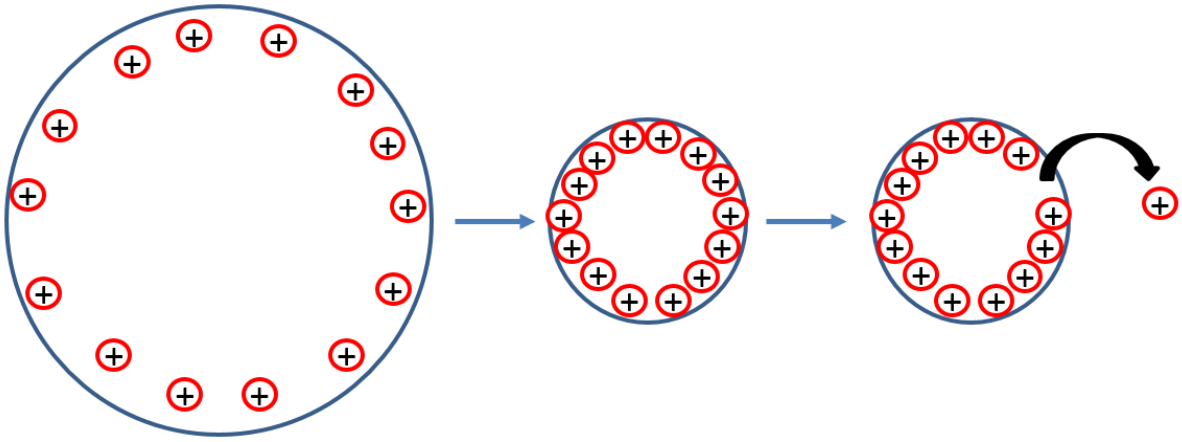

Figure 7 Ion evaporation model schematic

As a summary, the real mechanism is possibly a combination of CRM and IEM. The authors propose that the lower charge states are due to an ion evaporation stage (IEM) that precedes the charged residue formation (CRM) of the protein.

2.2 High Performance Liquid Chromatography (HPLC)

Most materials in our surroundings are mixtures of two or more components. Mixtures can be separated into their components by several physical methods. The choice of separation techniques is based on the type of mixture and difference in the chemical properties of the components of mixture, such as polarity, size, H-bonding, π-π interaction, etc. Depending on these involved properties, chromatography can be classified into five modes of separation based on interaction between the stationary and mobile phase: adsorption (normal-phase), partition, ion exchange, molecular exclusion (size exclusion), and affinity chromatography.

Chromatography is a separation technique used to separate the different components in a liquid mixture. It was introduced by Michael Tswett.[38] Chromatography involves the sample being dissolved in a particular solvent called mobile phase. The mobile phase may be a gas or liquid. The mobile phase is then passed through another phase called stationary phase. In this process, the different properties of components leads to different interaction with both mobile phase and stationary phase. The various components of the mixture travel at different speeds, causing them to separate. There are different types of chromatographic techniques such as column chromatography, thin layer chromatography, paper chromatography, gas chromatography and liquid chromatography (LC).

Generally, LC is coupled with a diode array detector (DAD).[39] The UV and visible light absorption of the sample is continuously measured at single or multiple selected wavelengths.

Liquid chromatography–mass spectrometry (LC-MS, or HPLC-MS) is an analytical chemistry technique that is actually a combination of the physical separation, function

of HPLC, with the mass analysis, function of MS. HPLC-MS gained its popularity on a variety of aspects and applications. A typical HPLC system contains mobile phase reservoirs, a degasser, pump, auto-sampler, column and column oven, and detector. Figure 8 presents a schematic of an HPLC system.

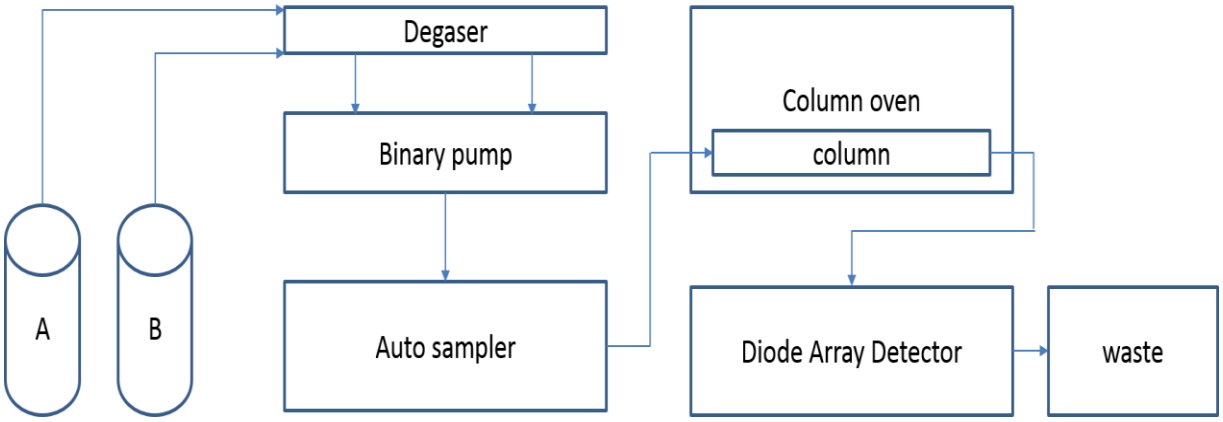

Figure 8 HPLC schematic

The HPLC system used in this experiment utilizes a Reverse-phase chromatography (RPC) method. RPC is one of the most popular modes of separation used in chromatography. In normal-phase chromatography, the stationary phase is polar and the mobile phase is non-polar. RPC is the reverse of normal-phase chromatography, hence the name. The stationary phase is non-polar and the mobile phase is polar. Typical stationary phases consist of long hydrocarbon chains, such as octadecyl (C18), octyl (C8), and phenyl, attached to a support (silica or cross-linked polymer), while the mobile phase uses polar solvents such as methanol, acetonitrile, and tetrahydrofuran (THF). These solvents are typically mixed with water.[40]

2.3 Anthraquinone Dyes

2.3.1 Anthraquinones

Anthraquinones are a series of aromatic compounds containing a 9,10-anthraquinone skeleton as the basic structure (Figure 9). These compounds are widely occurring in both nature and industries such as natural pigments, dyes, drug intermediates, and metabolic enzyme substrates[41].

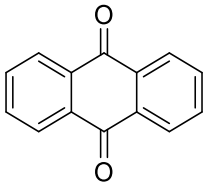

Figure 9 9,10-anthraquinone

2.3.2 Dyes

Dyes are classified as colorants which have an absorbance of light in the visible spectrum (380 to 780 nm) and are able to present visible colors. The first uses of dyes by prehistoric human were "natural" dyes from plants, animals, and minerals.[42] In 1856, William Henry Perkin developed the first commercially synthetic dye product aniline purple (mauve) based on his work on synthetic anilin.[43,44] Later, synthetic dyes followed, such as fuchsine, safranine, and induline, and then synthetic dyes started the occupation of dying industry.[43,44] Nowadays, most of the dyes are synthetically produced.

Disperse dyes were first developed for dyeing cellulose acetate in the 1920s. The introduction of polyester fibers by Imperial Chemical Industries into the textile market in 1948

allowed disperse dyes to become one of the fastest growing dye classes,[45] since only disperse dyes were able to be used for dyeing polyester. Disperse dyes are nonionic molecules with very low water solubility, which is beneficial for dyeing hydrophobic fibers, such as cellulose acetate, polyester, and nylon. The slight water solubility is due to the presence of polar substituents in their molecular structures and low molecular weight.[46,47]

Disperse dyes could be categorized into three main classes based on the chemical skeleton: anthraquinone, azo, and nitrodiphenylamine. Anthraquinone disperse dyes yield bright colors ranging from reds, violets, blues, and greens with relatively low washfastness.[42,43,47] However, environmental regulations during manufacture of anthraquinone dyes have increased production costs, which have caused dyestuff manufacturing companies to gradually replace some anthraquinone dyes with less expensive alternatives.[47,48] Even though, many anthraquinone dyes are still commercially important for dyed polyester with high wash fastness properties.

A database is needed due to the extensive utilization of anthraquinone dyes. By using mass spectrometry, the rapid structure analysis method could be developed and MS or MS/MS database could be obtained. Structure elucidation information provided further fast identification on known anthraquinone compounds and prediction on the unknown structure. Due to the wide occurrence of the widely occurring of anthraquinone, the database would be potentially extended to cover not only dyestuff, but also drugs, alkaloids, ligands and metabolic enzymes.

3. Materials

3.1 Solvents

HPLC grade acetonitrile was purchased from J.T.Baker, Deionized water was obtained from ELGA Purelab Ultra AN MK2.

3.2 Other supplies

Disposable Luer-slip plastic syringes (1 mL), Millex-GV 13 mm, 0.22 μm polyvinylidene fluoride (PVDF) filters, syringe needles (0.52 mm O.D. x 0.26 mm I.D., 25 gauge), and Fisherbrand 15 x 45 mm, 1-dram glass vials were purchased from Fisher Scientific. Amber screw top glass vials (2 mL) were purchased from Agilent Technologies (Part number: 5188-6535).

3.3 Dyes

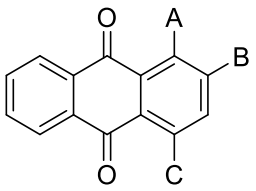

Figure 10 Common structure of selected anthraquinone derivatives.

Selected compounds are categorized by organic functionalities at three substituted positions: **A** with amino group: $–NH_2$ (A1) and $–NHCH_3$ (A2); **B** with sulfamide (with aliphatic amine (B1) and/or phenyl group (B2)), sulfone (B3), thioether (B4) and bromine (B5); **C** with aromatic (C1 and C2) or aliphatic amine (C3) and thioether (C4). Different combinations were

selected to compare different fragments. From which to understand the fragmentation pathways based on the group functionalities present in the molecule. This study would be helpful to determine the substitution on the unknown anthraquinone. All anthraquinone derivatives were collected from **Max A. Weaver Dye Library** at College of Textile, NCSU. Structures of all categorization of functionalities from selected dyes are presented in Figure 11 below:

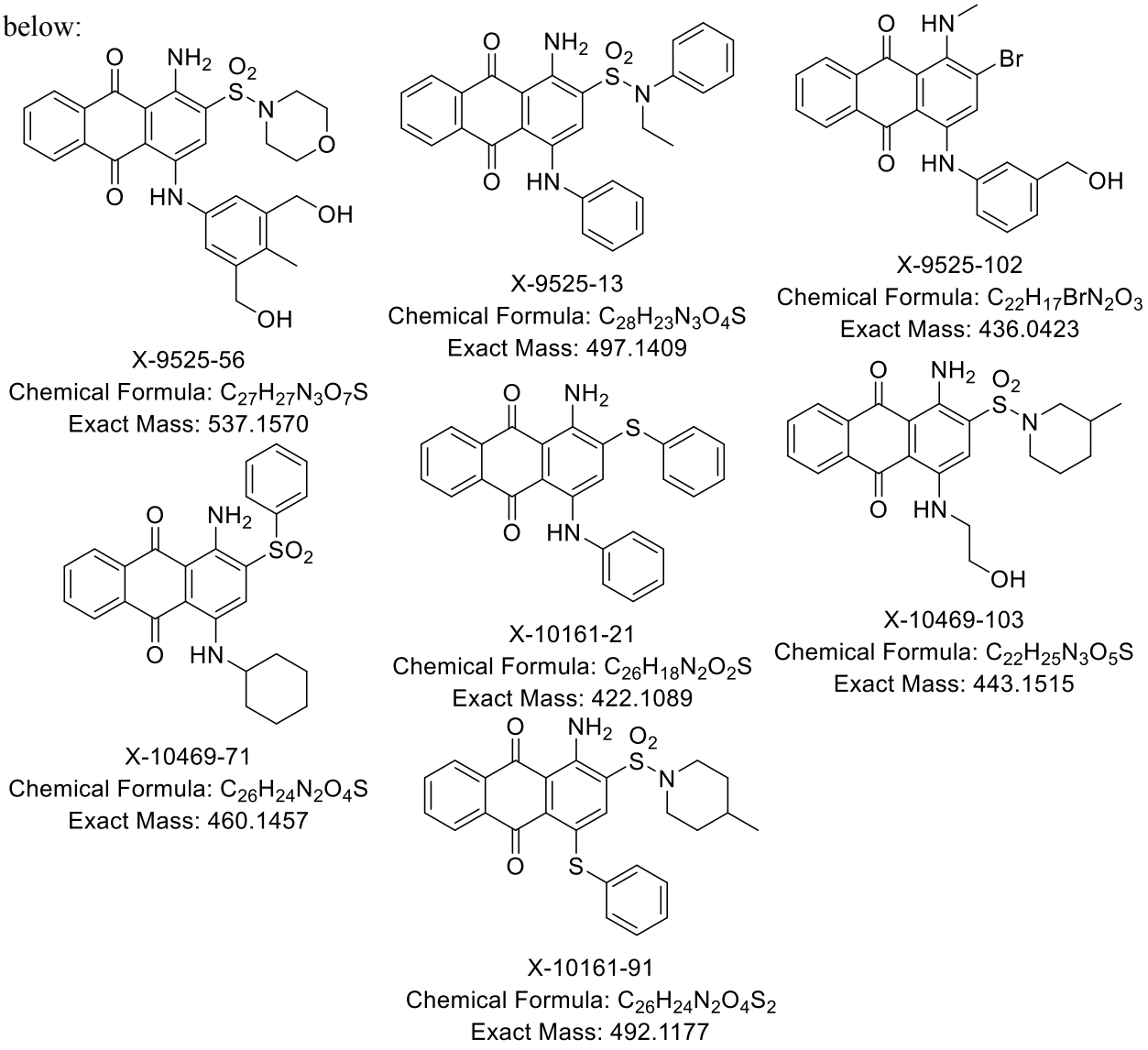

Figure 11 Sturctures and information of selected anthraquinone dyes

A1: X-9525-56, X-10469-13, X-10161-91, X-10469-71, X-9525-13, X-10161-21; **A2:** X-9525-102; **B1:** X-9525-56, X-10469-13, X-10161-91; **B2:** X-10469-71; **B3:** X-9525-13; **B4:** X-10161-21; **B5:** X-9525-102; **C1:** X-9525-13, X-10161-21; **C2:** X-9525-56, X-9525-102; **C3:** X-10459-71, X-10469-73; **C4:** X-10161-91. All anthraquinone dyes structures are presented in APPENDIX. *A*

4. Instrumentation and Experiments

4.1 Sample preparation

All dye powders were prepared for analysis by weighing and dissolving 1 mg of the dye in 1 mL of acetonitrile in a 1-dram Fisherbrand 15 x 45 mm, glass vial. A 1:100 dilution of the stock solution to 1 mL was performed to avoid saturating of the mass spectrometer detector. The diluted samples were filtered using 1-mL disposable Luer-slip plastic syringes and PVDF filters (Fisher Scientific) into 2-mL Agilent amber screw top glass LC vials (Part number: 5188-6535) for analysis.

4.2 HPLC purification

4.2.1 Mobile Phase

Solvents for these experiments were composed of water as the aqueous phase (mobile phase A) and acetonitrile as the organic phase (mobile phase B). The mobile phase was prepared based on the number of samples analyzed. For 20 samples, based on a 5 minute total run time and 0.5 mL/min flow rate.

4.2.2 HPLC Parameters

LC: Chromatographic purification was performed with an Agilent Poroshell^{TM} 120 EC – C18, 2.7 μm, 3.0 x 100 mm reverse-phase column. The isocratic method used is 5% of mobile phase A and 95% of mobile phase B. The flow rate was 0.5 mL/min, the total run time was 5 minutes, and the equilibration time between samples was 1 minute. The injection volume of each sample was 1 μL.

DAD: Agilent Technologies 1260 liquid chromatograph is equipped with a photodiode array detector (DAD). The DAD was used on a 190 – 780 nm wavelength scan.

4.3 MS and Tandem MS (MS/MS)

MS: The Agilent Technologies 1260 liquid chromatography is coupled to an Agilent Technologies 6520 Accurate-Mass Quadrupole–Time-of-Flight (Q-TOF) mass spectrometry equipped with an electrospray ionization (ESI) source. Ionization was carried out in positive ionization mode. Mass spectrometer conditions were: nebulizer pressure, 35 psig; capillary voltage, 4000 V; drying gas flow, 12 L/min at 350°C; fragmentor voltage, 175 V.

CID: Tandem MS were performed using MS/MS acquisition function of Agilent MassHunter Acquisition interface. The analyte ions of interest were isolated using a narrow window (~1.3). Collision energy was 20 eV

The LC-Q-TOF was operated using an HP xw4600 Workstation computer. Data collection and analysis were performed respectively using Agilent MassHunter Acquisition and Agilent MassHunter Qualitative Analysis B.06.00. Calibration of the mass spectrometer

was performed per manufacturer settings.

5. Results and Analysis

5.1 Purification

The dyes collected from **Max A. Weaver Dye Library** are synthetic but impure, with unknown purities and unknown additions such as auxiliary chemicals. To avoid ion suppression and other influence from these unknown stuffs, HPLC purification method was developed. Figure 12 presents an example comparison between direct injection (without purification) and HPLC purification of same sample X-9525-13.

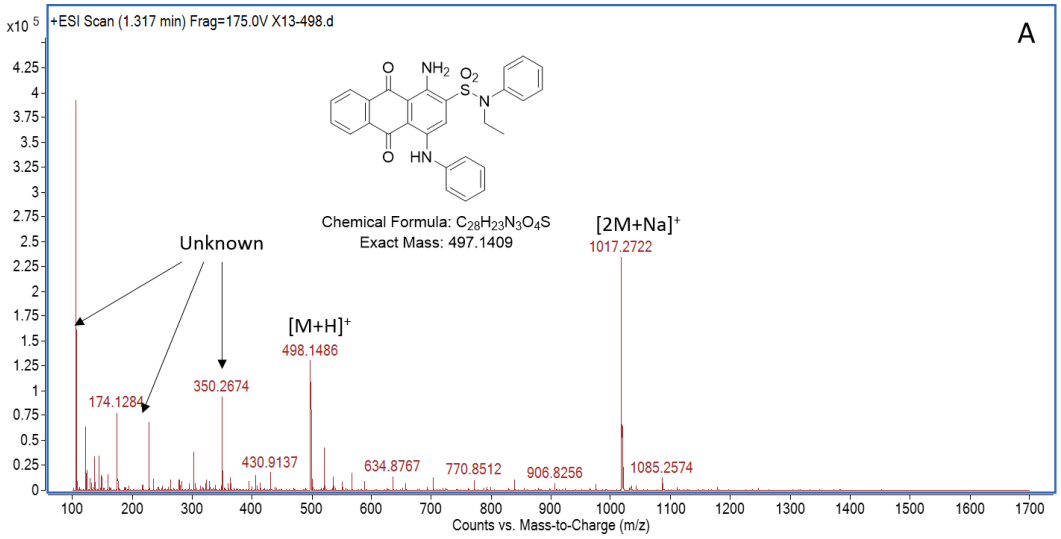

Figure 12 Full MS spectrum of direct injection, DAD and EIC after HPLC purification and r.t. MS spectrum

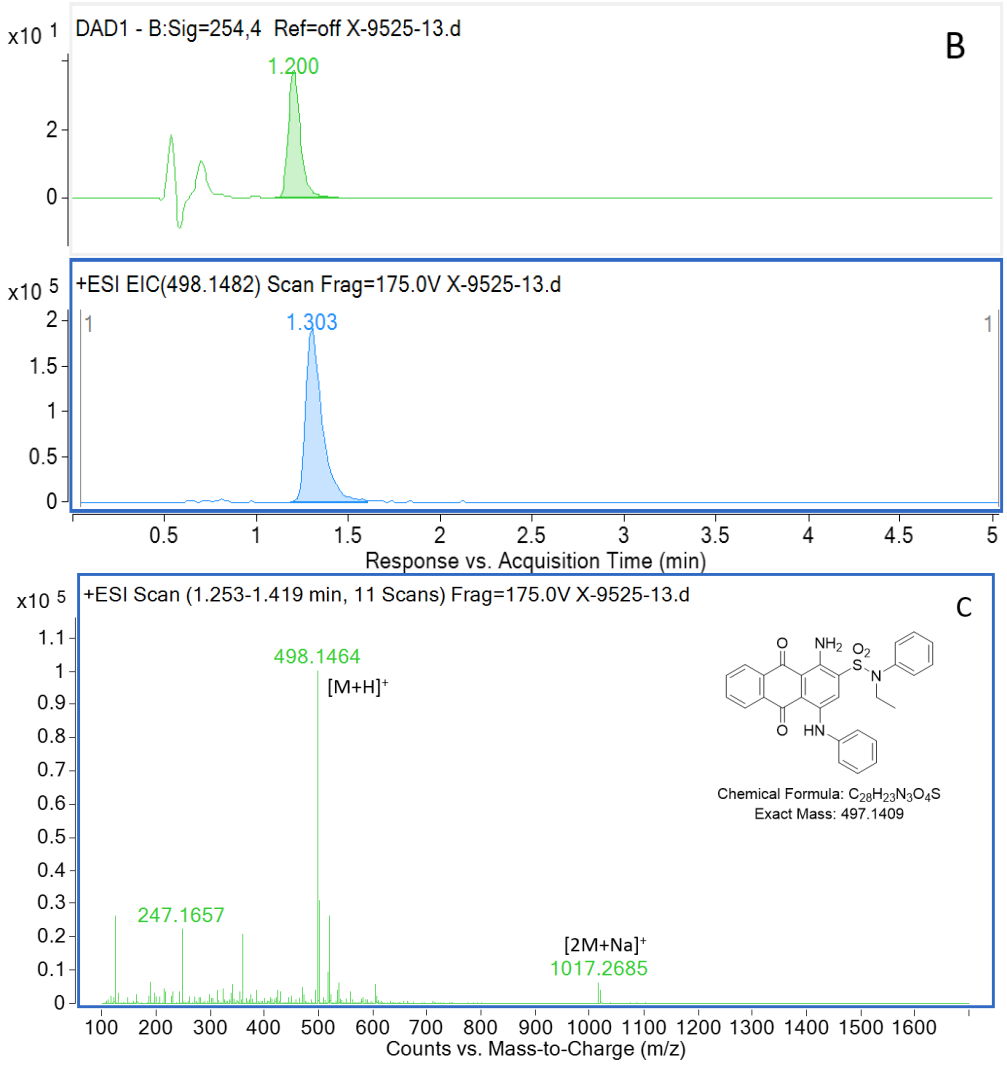

Figure 13 continued

Figure 12A shows an unclear MS spectrum: a variety of unknown signals were presented with the expected signal $[M+H]^+$ at same time. Sodium cluster $[2M+Na]^+$ were making more convoluted the spectrum. Figure 12C presents a more clear spectrum after purification, in which the expected $[M+H]^+$ signal was the most significant one. Figure 12B is the DAD and EIC chromatogram that shows the clear absorbance of the dye at 254 nm to indicate that sample has been well-purified.

For most of the samples, the HPLC purification provided good enhancement. Although in some of them the protonated molecule ($[M+H]^+$) were not the most significant signal in the spectra.

The retention time (r.t.), theoretical m/z and observed m/z information are listed in Table 1 in section 5.2. All 254 nm DAD chromatograms and MS spectra at the retention time from HPLC purified samples are listed in APPENDICES. B. 254 nm DAD chromatograms ， extracted ion chromatograms and MS spectra at retention time.

5.2 Verification by DAD and MS

Retention time (RT) was obtained from 254 nm DAD chromatogram and used to extract MS spectrum. For each sample, an Extracted Ion chromatography (EIC) was performed at the desired RT, the observed m/z were the expected values, and compared with the theoretical value all of them have an error below of 5ppm (Table 1).

Table 1 Sample verification of all selected anthraquinone dyes.

Dye	DAD r.t. (min)	EIC r.t. (min)	Theoretical m/z	Observed m/z	ppm Error
X-9525-9	1.087	1.189	492.1588	492.1573	-3.05
X-9525-10	1.180	1.278	506.1744	506.1734	-1.98
X-9525-11	1.260	1.354	506.1744	506.1725	-3.75
X-9525-12	1.373	1.463	520.1901	520.1881	-3.84
X-9525-13	1.200	1.303	498.1482	498.1464	-3.61
X-9525-14	1.573	1.670	534.2057	534.2038	-3.56
X-9525-15	1.420	1.525	532.1092	532.1078	-2.63
X-9525-16	1.413	1.503	512.1639	512.1624	-2.93
X-9525-71	1.507	1.644	520.1901	520.1885	-3.08
X-9525-51	0.773	0.917	622.1854	622.1823	-4.98
X-9525-56	0.640	0.739	538.1642	538.1653	2.04
X-9525-60	0.933	1.047	620.2061	620.2071	1.61
X-9525-102	1.007	1.116	437.0495	437.0478	-3.89

Table 1 Continued

Dye	DAD r.t. (min)	EIC r.t. (min)	Theoretical m/z	Observed m/z	ppm Error
X-9525-103	0.980	1.073	467.0601	467.0582	-4.01
X-10161-21	1.527	1.627	423.1162	423.1173	2.60
X-10161-70	1.193	1.306	468.1013	468.0997	-3.42
X-10161-91	1.080	1.175	493.1250	493.1237	-2.64
X-10469-71	1.400	1.472	461.1530	461.1516	-3.04
X-10469-103	0.747	0.821	444.1588	444.1572	-3.60
X-10469-110	0.627	0.698	432.1224	432.1209	-3.47

Certain samples have a signal of radical cation $[M]^{+\cdot}$ in MS spectrum as well as the protonated molecule, which has been observed and discussed previously.[49-51] Current conclusion of the generation of radical cation refer to a slightly oxidation from the charged metal capillary at the ESI source. Figure 13 below shows an example of radical cation generated by ESI in this research:

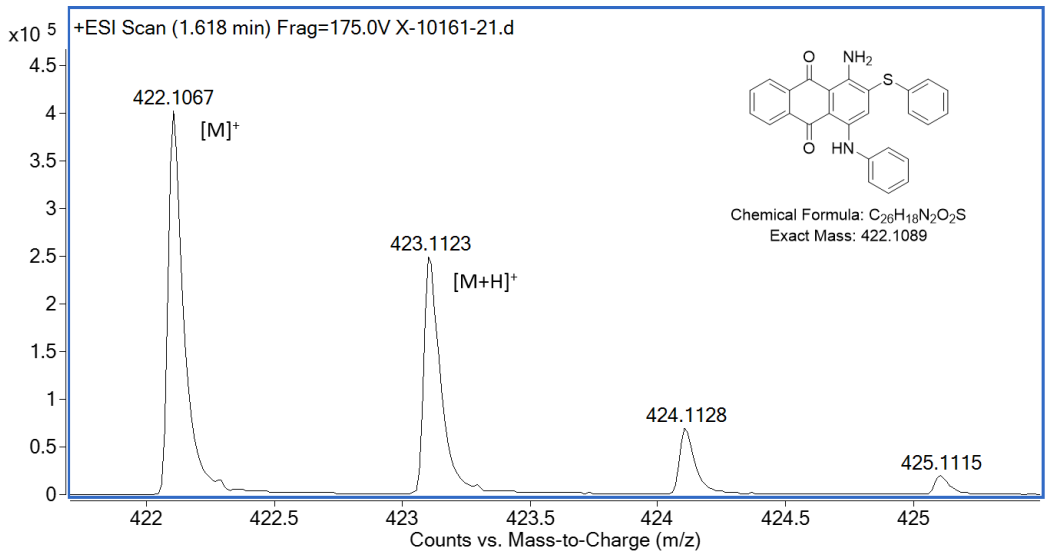

Figure 14 Radical cation and protonated ion of X-10161-21

5.3 MS/MS Data Analysis

As important part of a structure elucidation, fragments pathway analysis of each analytes has been performed. Table 2 shows a summary of all observed fragments from each type of functionalities. For each type of fragment pathway, examples are presented in subtitled section later, respectively. All MS/MS spectra are presented in APPENDICES. C.

Table 2 Categorization of collected samples based on functionalities and the fragments pathway of each type of group. (Aq is the anthraquinone skeleton)

Position	Group	Fragments
A1	$Aq-NH_2$	None
A2	$Aq-NH$ \	$-CH_3$

Table 2 Continued

Position	Group	Fragments
B1	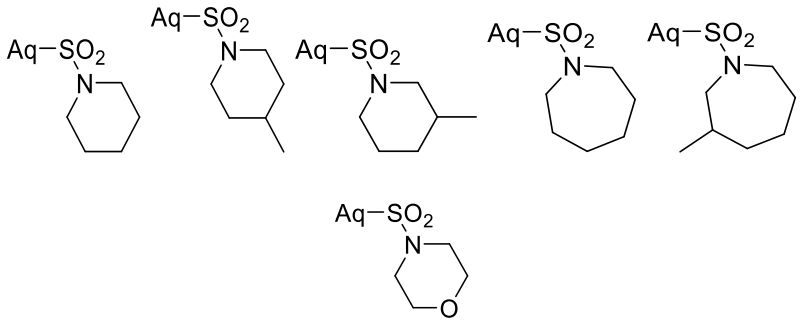	-Ni-ring -SO_2Ni-ring -SONi-ring
B2	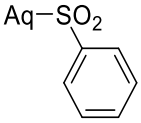	-SO_2Ph
B3	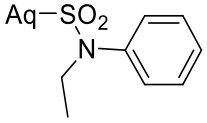	-NCH_2Ph -NEtPh -SO_2NEtPh
B4	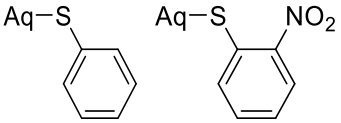	-S-Ph -S-Ph-NO_2 -Ph -Ph-NO_2
B5	Aq—Br	None

Table 2 Continued

Position	Group	Fragments
C1	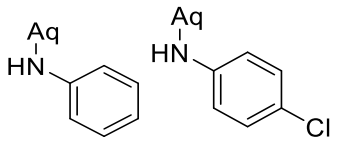	None
C2	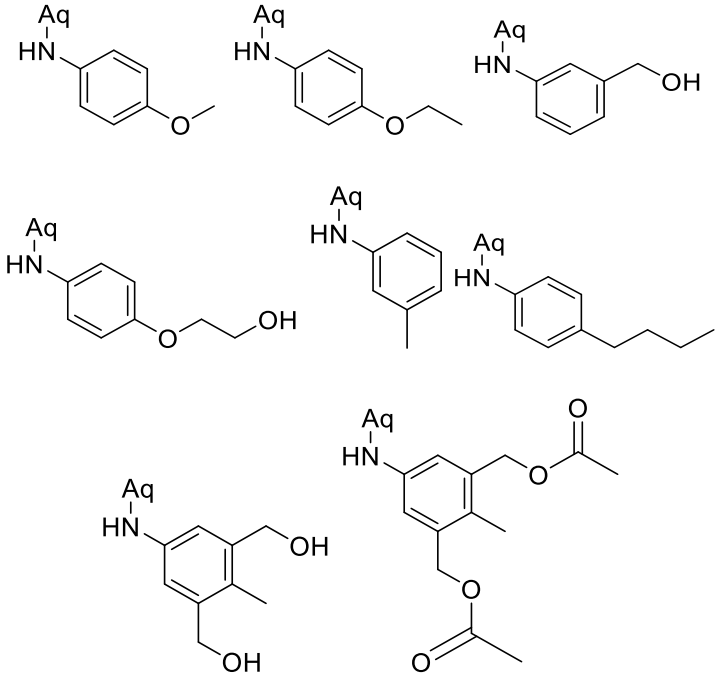	-R -OR -COR -$OOCCH_3$ -H_2O -C_2H_4OH
C3	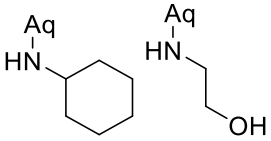	-CH_2CH_2OH -C_3H_6 -C_4H_8 -C_6H_{10}
C4	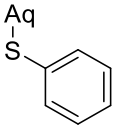	-Ph

5.3.1 Position A, fragment pathway from Aq-NH_2

No fragments were observed.

5.3.2 Position A, fragment pathway from Aq-NH-CH_3

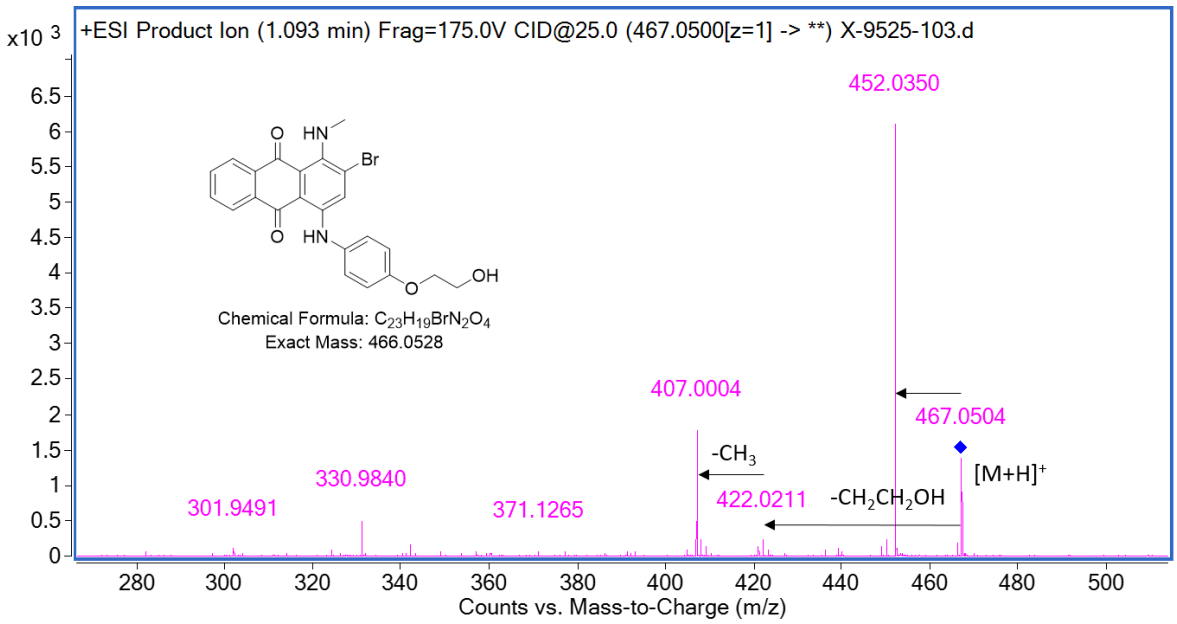

Figure 15 Fragment pathway of Aq-NH-CH_3, from sample X-9525-103

-CH_3 loss from Aq–NH-CH_3 in position A was observed in X-9525-102 and X-9525-103. The $[M+H-CH_3]^+$ caused by -CH_3 loss seems to be the main fragment. Figure 14 above shows example from X-9525-103.

5.3.3 Position B, fragment pathway from Aq-SO_2-Nring

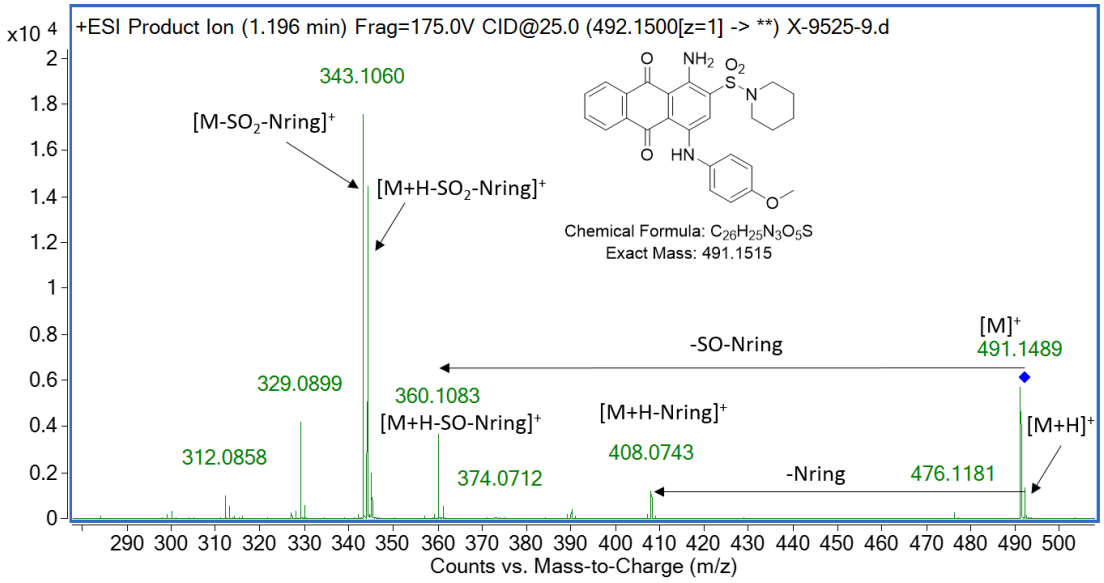

Figure 16 Fragment pathway of Aq-SO2-Nring, from sample X-9525-9

Figure 15 above shows an example from X-9525-9. Foreseeable –Ni-ring loss, -SO-Ni-ring loss and -SO2-Ni-ring loss of Aq–SO2-Ni-ring in position B was observed for dyes X-9525-9, X-9525-10, X-9525-11, X-9525-12, X-9525-14, X-9525-60, X-10161-91, X-10469-103, X-9525-71, X-9525-51, X-9525-56 and X-10469-110. The SONi-ring loss indi-cates a potential rearrangement. Figure 16A presents the rearrangement and B presents a proposed rearrangement mechanism.

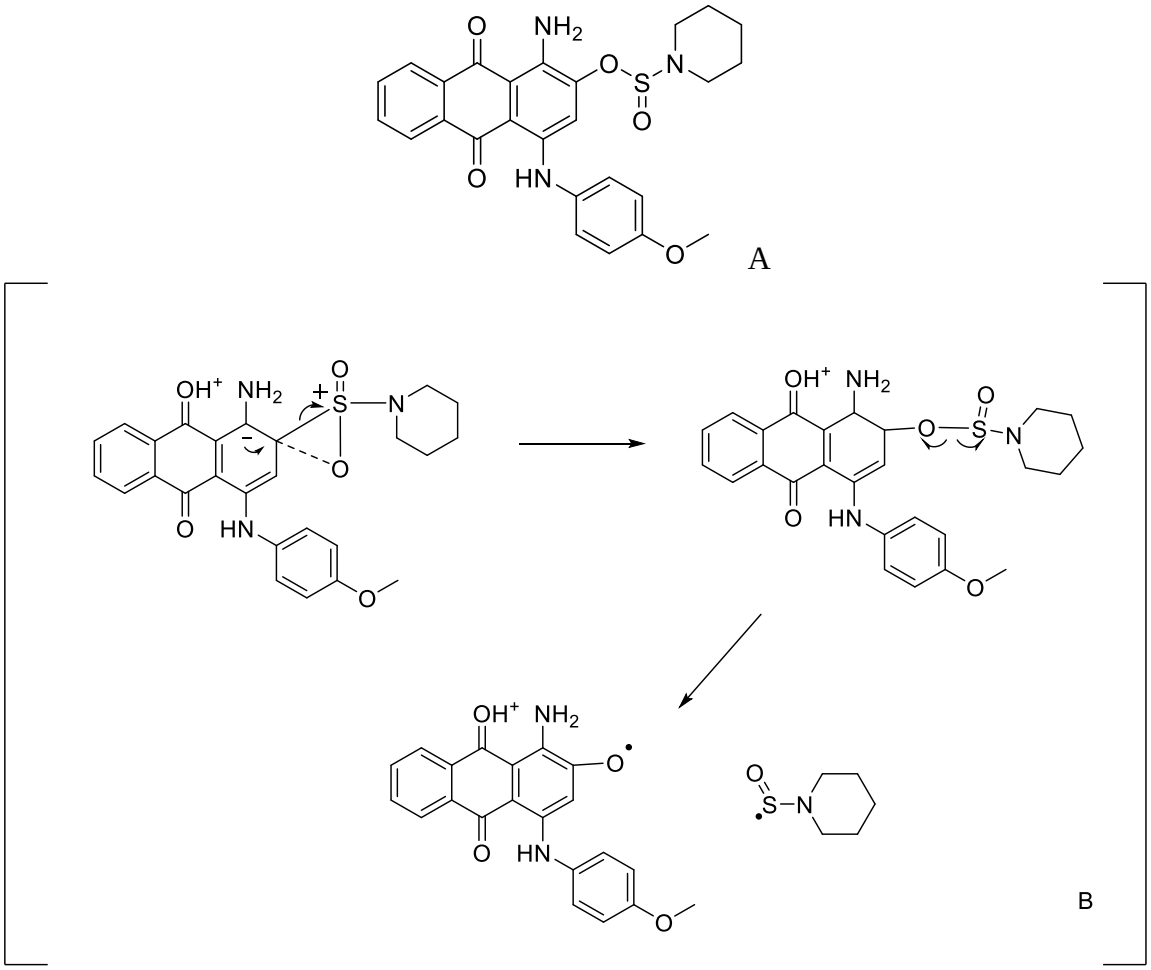

Figure 17 A is the possible structure after the rearrangement; B is a proposed mechanism or rearrangement.

5.3.4 Position B, fragment pathway from Aq-SO_2-Ph

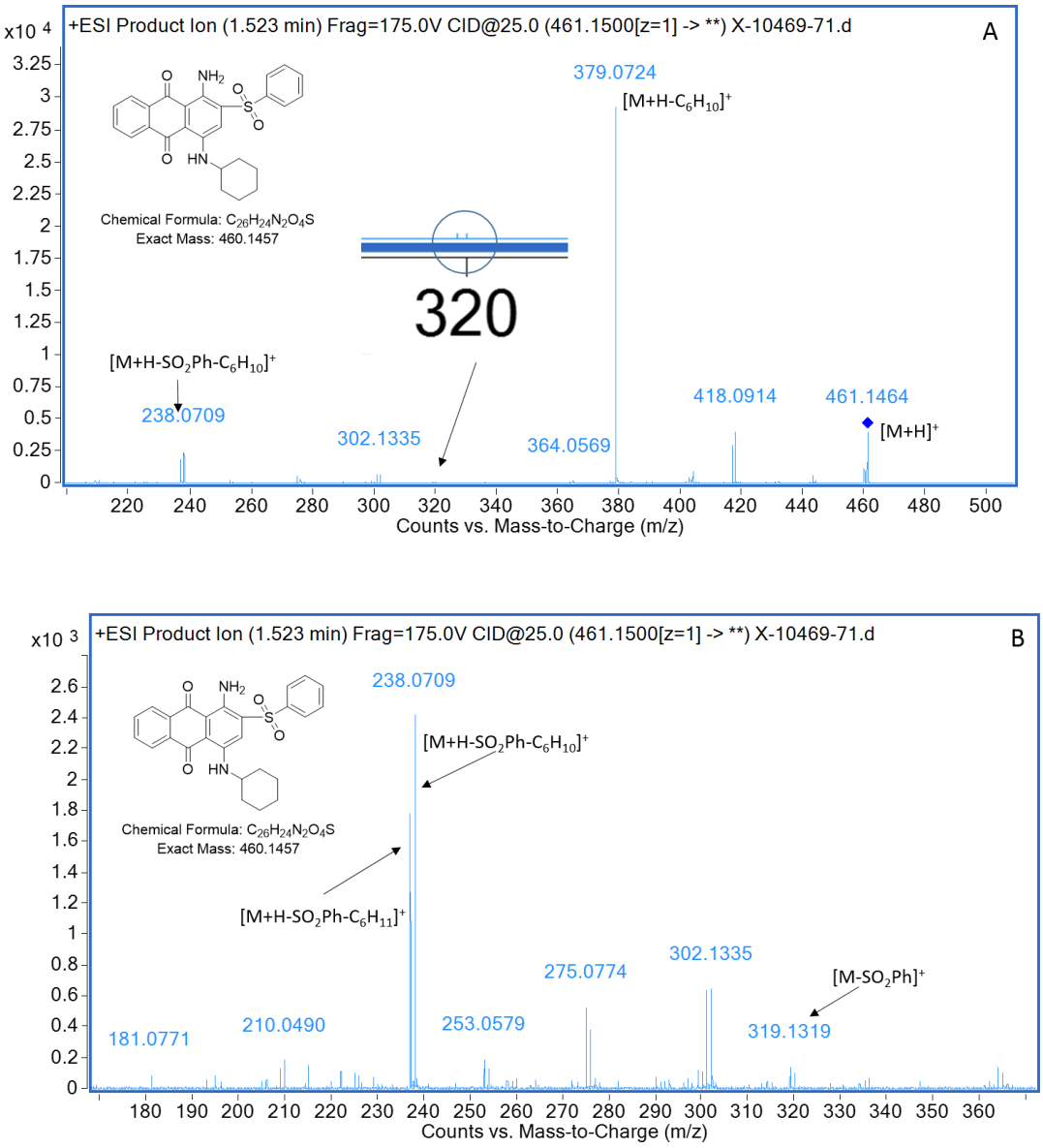

Figure 18 Fragment pathway of Aq-SO_2Ph, from sample X-10469-71

Unlike Aq-SO2-Ni-ring, Aq-SO2-Ph has only one type of fragment with very low abundance. A possible reason is that the conjugated system improved the ion stability. Figure 17AB shows the low abundant -SO2Ph loss from X-10469-71. 17B is zoomed-in of 17A.

5.3.5 Position B, fragment pathway from Aq-SO_2-NRPh

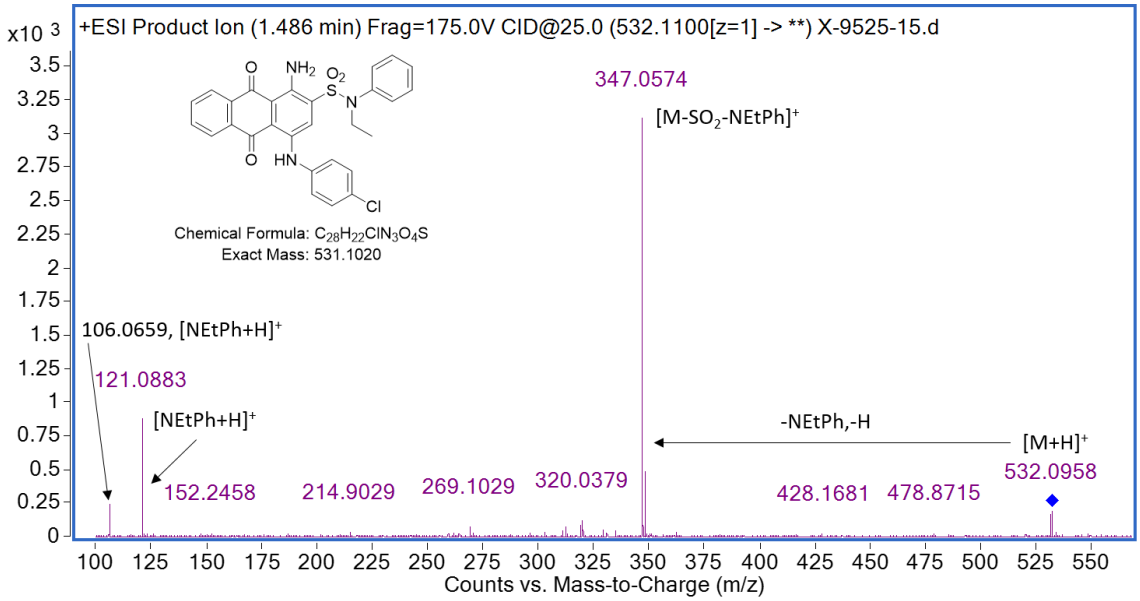

Figure 19 Fragment pathway of Aq-SO_2NEtPh, from sample X-9525-15

-SO_2-NEtPh loss of Aq-SO_2-NEtPh and $[NEtPh+H]^+$ were observed in X-9525-13, X-9525-15 and X-9525-16, but the demethylation of –NEtPh was only observed in X-9525-18. In X-9525-15, the signal 106.0659 indicates a $[CH_2NPh+H]^+$ ion which is dimethylated from $[NEtPh+H]^+$. See Figure 17 above.

5.3.6 Position B, fragment pathway from Aq-S-Ph

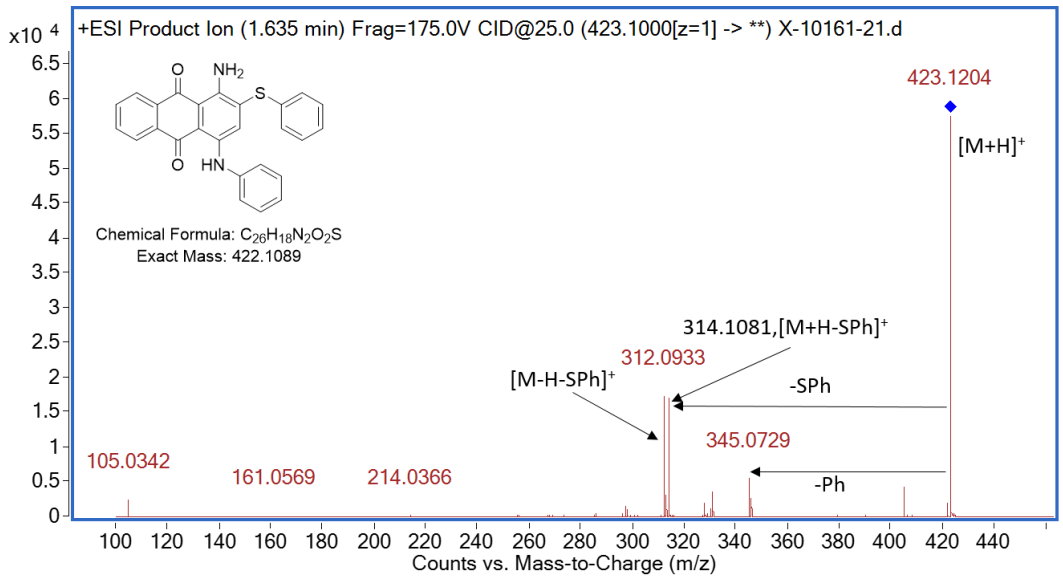

Figure 20 Fragment pathway of Aq-S-Ph, from sample X-10161-21

Main fragment is –S-Ph loss and –Ph loss. Observed in X-10161-21 and X-10161-70. X-10161-70 has –NO2 group on the phenyl group attached to suffer. X-10161-71 has lower –Ph-NO2 loss fragment abundance than that of X-10161-21. Fragment pathway shows in Figure 19 Above.

5.3.7 Position B, fragment pathway from Aq-Br

No fragments were observed.

5.3.8 Position C, fragment pathway from Aq-NH-Ph

No fragments were observed.

5.3.9 Position C, fragment pathway from Aq-NH-Ph-tail

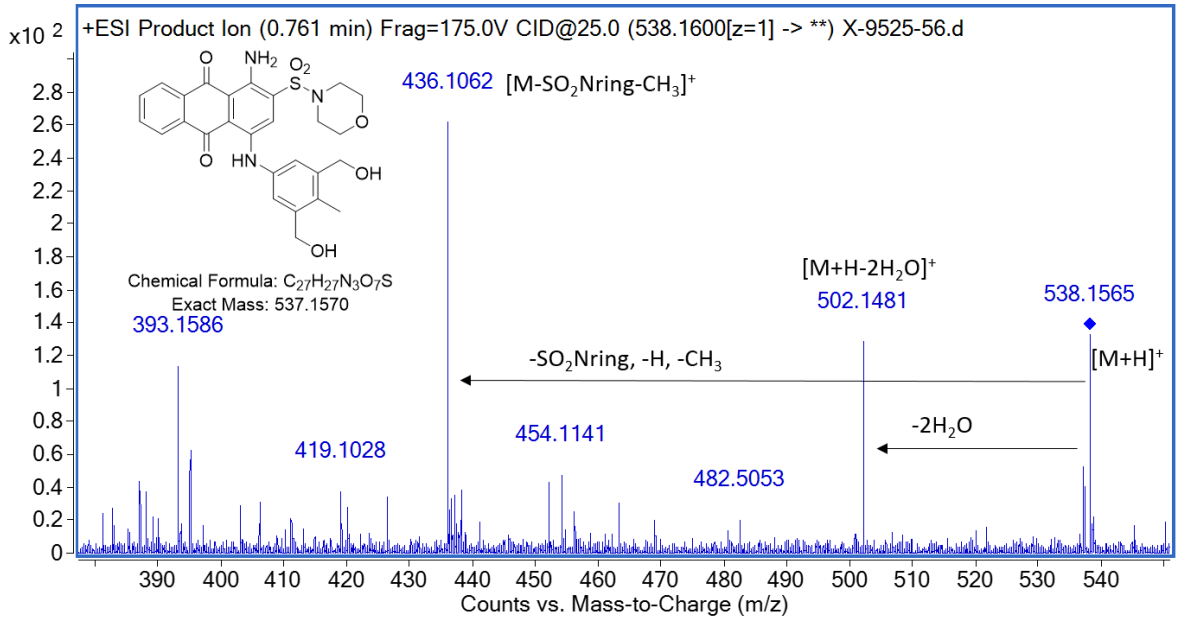

Figure 21 Fragment pathway of Aq-N-Ph-tail, from sample X-9525-56

All observed fragments were from the different aromatic substitutions that were related to the aliphatic group attached to the phenyl amine group. These results agree with section 5.3.8. Sample X-9525-9, X-9525-10, X-9525-11, X-9525-12, X-9525-14, X-9525-16, X-9525-71, X-9525-51, X-9525-56, X-9525-60; X-9525-102 and X-9525-103 have the behavior. Figure 20 shows the MS/MS spectrum.

5.3.10 Position C, fragment pathway from Aq-NH-R

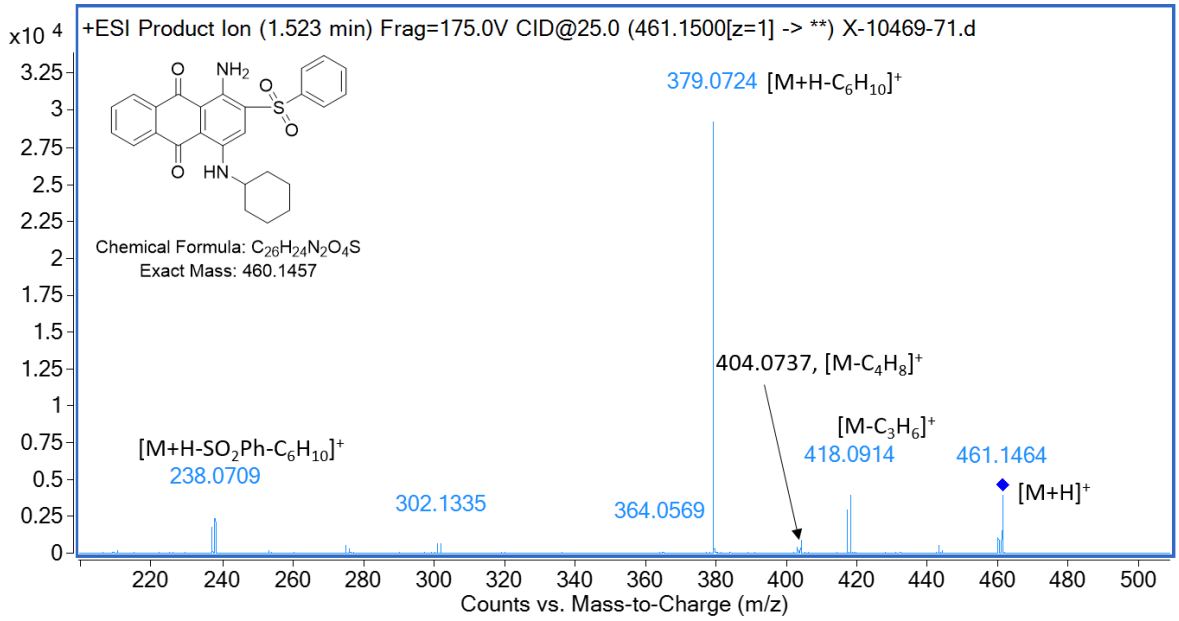

Figure 22 Fragment pathway of Aq-NH-R, from sample X-10469-71

In this case, the R group can be an aliphatic chain or ring (X-10469-71; X-10469-103, X-10469-110). Normally the aliphatic chains have fragmentation common to alkanes. The aliphatic ring will fragment by ring cleavage depending on the size of the ring generating alkene fragments. Figure 21 shows various fragment pathways of the ring.

5.3.11 Position C, fragment pathway from Aq-S-Ph

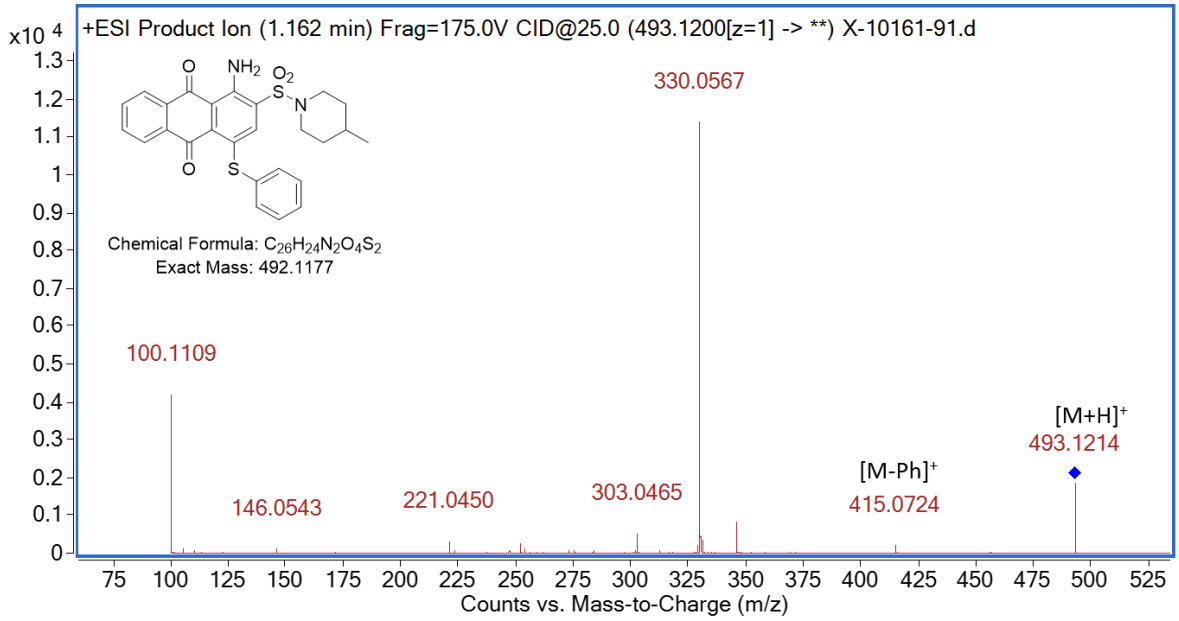

Figure 23 Fragment pathway of Aq-S-Ph, from sample X-1161-91

The –S-Ph group on position B and C (which are α and β positions of anthraquinone) demonstrates different behavior. Although they have the same –Ph loss, the –S-Ph on position C could not be cleaved. 415.0724 signal which is $[M-Ph]^+$ in Figure 22 indicates the –Ph loss from –S-Ph group.

6. Conclusion

DAD chromatograms and MS spectrums verified the collected dyes have the correct formulas on the labels. The HPLC purification method was suitable for all of the samples, and helped to avoid ion suppression. All of the samples formed stable protonated molecules ($[M+H]^+$) in ESI positive mode. Some of them also formed $[M]^+$ ions in ESI which agrees with previous discoveries seen in other research groups.[49-51] The protonated molecules formed in

positive-mode ESI were subjected to several consecutive ion isolation and CID events, which revealed fragmentation patterns that facilitate the identification of amino, methylamino , sulfamide (with aliphatic amine and/or aromatic amine), sulfone and thioether group, aromatic or aliphatic amine).

Based on CID results, structure elucidation based on certain compounds has been established as a way to identify group functionalities attached to the anthraquinone. Based on Agilent MassHunter Qualitative Analysis software, a database of both MS and MS/MS has been developed, this database is able to be extended to other new Agilent Q-TOF MS instruments. Aromatic and aliphatic functionalities have different contributions to the ion stability of the fragments produced by CID, which lead to different fragment abundance and even different fragment pathways. Random ring opening of aliphatic rings was found when attached to aq-amine. Rearrangement of the -SO2- group was found among most of the selected compounds with the B1 group. Loss of -S-Ph group varies with different positions.

7. Recommendation and future work

A new HPLC separation method is needed. As a powerful separation technique, HPLC is not only good for the purification of single commercial dyes, but also good for separation of mixtures.

Quantitative analysis is needed for forensic analysis and trace analysis purposes.

Continued analysis of anthraquinone dyes is needed to extend the dye database. More types of structures are needed to be involved.

Statistic methods such as cluster analysis is potentially appropriate to be introduced to the development of the database.

REFERENCES

1. Delmulle L, Demeyer K. *Anthraquinones in plants: Source, safety and applications in gastrointestinal health.* Nottingham University Press; 2010.

2. McKelvey RD, Malcolm EW. Anthraquinone/alkali pulping, a literature review. .

3. Bien H, Stawitz J, Wunderlich K. Anthraquinone dyes and intermediates. *Ullmann's Encyclopedia of Industrial Chemistry*. 2000.

4. Pickhardt M, Gazova Z, von Bergen M, et al. Anthraquinones inhibit tau aggregation and dissolve alzheimer's paired helical filaments in vitro and in cells. *J Biol Chem*. 2005;280(5):3628-3635. doi: M410984200 [pii].

5. Hedenus M. Eugen goldstein and his laboratory work at berlin observatory. *Astronomische Nachrichten*. 2002;323(6):567-569.

6. Kragh H. *Quantum generations: A history of physics in the twentieth century.* Princeton University Press; 2002.

7. Thomson J. LXXXIII. rays of positive electricity. *The London, Edinburgh, and Dublin Philosophical Magazine and Journal of Science*. 1910;20(118):752-767.

8. Griffiths J. A brief history of mass spectrometry. *Anal Chem*. 2008;80(15):5678-5683.

9. Dass C. *Fundamentals of contemporary mass spectrometry.* Vol 16. John Wiley & Sons; 2007.

10. Hu Q, Noll RJ, Li H, Makarov A, Hardman M, Graham Cooks R. The orbitrap: A new mass spectrometer. *Journal of mass spectrometry*. 2005;40(4):430-443.

11. Baldwin MA, McLafferty FW. Liquid chromatography-mass spectrometry interface-I: The direct introduction of liquid solutions into a chemical ionization mass spectrometer. *Org Mass Spectrom*. 1973;7(9):1111-1112. doi: 10.1002/oms.1210070913.

12. Gross JH, SpringerLink (Online service). *Mass spectrometry: A textbook.* Berlin, Heidelberg: Springer Berlin Heidelberg; 2011. 10.1007/978-3-642-10711-5.

13. Dawson PH. *Quadrupole mass spectrometry and its applications.* Elsevier; 2013.

14. Chernushevich IV, Loboda AV, Thomson BA. An introduction to quadrupole–time‐of‐flight mass spectrometry. *Journal of Mass Spectrometry*. 2001;36(8):849-865.

15. Stephens W. A pulsed mass spectrometer with time dispersion. . 1946;69(11-1):691-691.

16. Cotter RJ. Time-of-flight mass spectrometry for the structural analysis of biological molecules. *Anal Chem*. 1992;64(21):1027A-1039A.

17. Mamyrin B. Laser assisted reflectron time-of-flight mass spectrometry. *International Journal of Mass Spectrometry and Ion Processes.* 1994;131:1-19.

18. Cotter RJ. *Time-of-flight mass spectrometry: Instrumentation and applications in biological research.* Amer Chemical Society; 1997.

19. Guilhaus M. Principles and instrumentation in time-of-flight mass spectrometry. *J Mass Spectrom*. 1995;30(11):1519-1532.

20. Ioanoviciu D. Ion‐Optical solutions in time‐of‐flight mass spectrometry. *Rapid communications in mass spectrometry*. 1995;9(11):985-997.

21. Mamyrin B. Time-of-flight mass spectrometry (concepts, achievements, and prospects). *International Journal of Mass Spectrometry*. 2001;206(3):251-266.

22. Fuerstenau SD, Benner WH. Molecular weight determination of megadalton DNA electrospray ions using charge detection time‐of‐flight mass spectrometry. *Rapid Communications in Mass Spectrometry*. 1995;9(15):1528-1538.

23. Vestal ML. Modern MALDI time‐of‐flight mass spectrometry. *Journal of mass spectrometry*. 2009;44(3):303-317.

24. Douglas D, French J. Collisional focusing effects in radio frequency quadrupoles. *J Am Soc Mass Spectrom*. 1992;3(4):398-408.

25. Krutchinsky A, Chernushevich I, Spicer V, Ens W, Standing K. Collisional damping interface for an electrospray ionization time-of-flight mass spectrometer. *J Am Soc Mass Spectrom*. 1998;9(6):569-579.

26. Watson JT, Sparkman OD. *Introduction to mass spectrometry: Instrumentation, applications, and strategies for data interpretation.* John Wiley & Sons; 2007.

27. Fernández de La Mora, Juan. The fluid dynamics of taylor cones. *Annu Rev Fluid Mech*. 2007;39:217-243.

28. Taylor G, McEwan A. The stability of a horizontal fluid interface in a vertical electric field. *J Fluid Mech*. 1965;22(01):1-15.

29. Cloupeau M, Prunet-Foch B. Electrohydrodynamic spraying functioning modes: A critical review. *J Aerosol Sci*. 1994;25(6):1021-1036.

30. Rayleigh L. XX. on the equilibrium of liquid conducting masses charged with electricity. *The London, Edinburgh, and Dublin Philosophical Magazine and Journal of Science*. 1882;14(87):184-186.

31. Gomez A, Tang K. Charge and fission of droplets in electrostatic sprays. *Physics of Fluids (1994-present)*. 1994;6(1):404-414.

32. Smith JN, Flagan RC, Beauchamp J. Droplet evaporation and discharge dynamics in electrospray ionization. *The Journal of Physical Chemistry A*. 2002;106(42):9957-9967.

33. Grimm RL, Beauchamp J. Evaporation and discharge dynamics of highly charged droplets of heptane, octane, and p-xylene generated by electrospray ionization. *Anal Chem*. 2002;74(24):6291-6297.

34. Kebarle P, Verkerk UH. Electrospray: From ions in solution to ions in the gas phase, what we know now. *Mass Spectrom Rev*. 2009;28(6):898-917.

35. Dole M, Mack L, Hines R, Mobley R, Ferguson L, Alice Md. Molecular beams of macroions. *J Chem Phys*. 1968;49(5):2240-2249.

36. Iribarne J, Thomson B. On the evaporation of small ions from charged droplets. *J Chem Phys*. 1976;64(6):2287-2294.

37. Znamenskiy V, Marginean I, Vertes A. Solvated ion evaporation from charged water nanodroplets. *The Journal of Physical Chemistry A*. 2003;107(38):7406-7412.

38. Tswett M. Physikalisch-chemische studien über das chlorophyll. die adsorptionen. *Berichte der Deutschen botanischen Gesellschaft*. 1906;24(316-323):20.

39. Lough WJ, Wainer IW. *High performance liquid chromatography: Fundamental principles and practice.* CRC Press; 1995.

40. Neue UD. *HPLC columns: Theory, technology, and practice.* Wiley-VcH; 1997.

41. Ritter JK, Chen F, Sheen YY, et al. A novel complex locus UGT1 encodes human bilirubin, phenol, and other UDP-glucuronosyltransferase isozymes with identical carboxyl termini. *J Biol Chem*. 1992;267(5):3257-3261.

42. Zollinger H. Color chemistry. . 1987.

43. Mock G. Fundamentals of dyeing and printing. *Lecture notebook, College of Textiles, NCSU*. 1997.

44. Perkin AG, Everest AE. *The natural organic colouring matters.* Longmans, Green and Company; 1918.

45. Rustemeyer P. *Cellulose acetates: Properties and applications; GAMA workshop, heidelberg, germany, september 29-october 1, 2003.* Vol 208. Wiley-VCH; 2004.

46. Moody V, Needles HL. *Tufted carpet: Textile fibers, dyes, finishes and processes.* William Andrew; 2004.

47. Broadbent AD. *Basic principles of textile coloration.* Vol 132. Society of Dyers and Colorists West Yorkshire; 2001.

48. Aspland JR. *Textile dyeing and coloration.* AATCC; 1997.

49. Moriwaki H. Electrospray mass spectrometric determination of 1-nitropyrene and non-substituted polycyclic aromatic hydrocarbons using tropylium cation as a post-column HPLC reagent. *Analyst*. 2000;125(3):417-420. doi: 10.1039/a908944f.

50. Van Berkel GJ, McLuckey SA, Glish GL. Electrochemical origin of radical cations observed in electrospray ionization mass spectra. *Anal Chem*. 1992;64(14):1586-1593. doi: 10.1021/ac00038a015.

51. Schäfer M, Drayss M, Springer A, Zacharias P, Meerholz K. Radical cations in electrospray mass spectrometry: Formation of Open‐Shell species, examination of the fragmentation behaviour in ESI‐MSn and reaction mechanism studies by detection of transient radical cations. *European Journal of Organic Chemistry*. 2007;2007(31):5162-5174.

APPENDICES

APPENDIX. A

Structures of all selected anthraquinone dyes

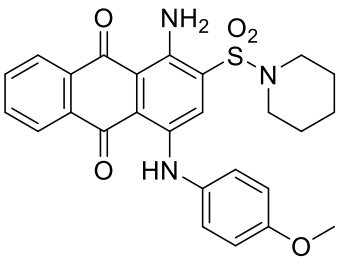

X-9525-9
Chemical Formula: $C_{26}H_{25}N_3O_5S$
Exact Mass: 491.1515

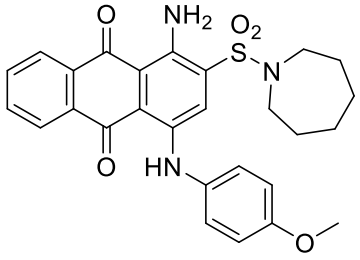

X-9525-10
Chemical Formula: $C_{27}H_{27}N_3O_5S$
Exact Mass: 505.1671

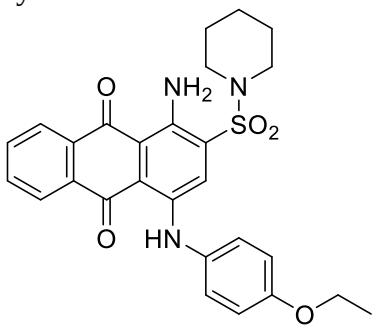

X-9525-11
Chemical Formula: $C_{27}H_{27}N_3O_5S$
Exact Mass: 505.1671

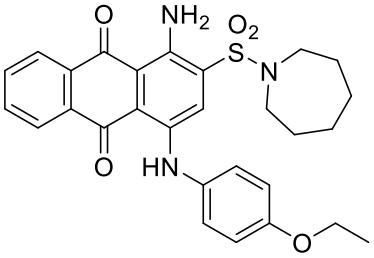

X-9525-12
Chemical Formula: $C_{28}H_{29}N_3O_5S$
Exact Mass: 519.1828

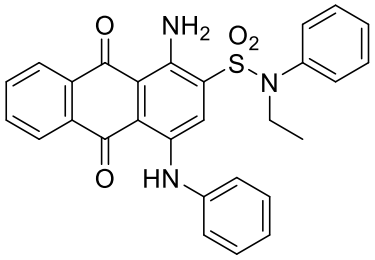

X-9525-13
Chemical Formula: $C_{28}H_{23}N_3O_4S$
Exact Mass: 497.1409

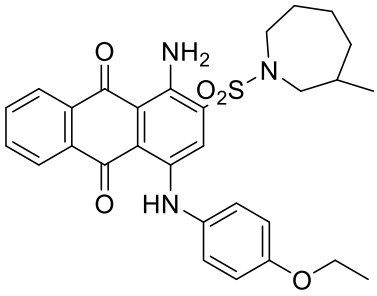

X-9525-14
Chemical Formula: $C_{29}H_{31}N_3O_5S$
Exact Mass: 533.1984

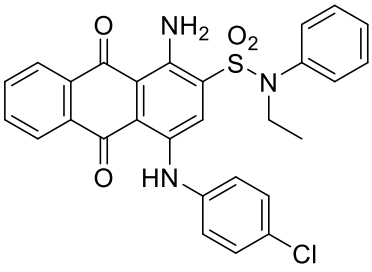

X-9525-15
Chemical Formula: $C_{28}H_{22}ClN_3O_4S$
Exact Mass: 531.1020

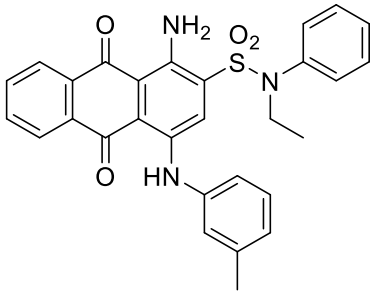

X-9525-16
Chemical Formula: $C_{29}H_{25}N_3O_4S$
Exact Mass: 511.1566

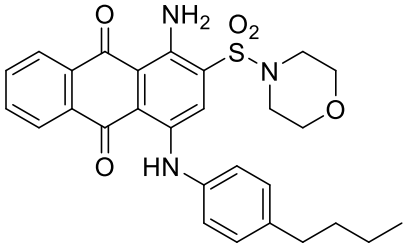

X-9525-71
Chemical Formula: $C_{28}H_{29}N_3O_5S$
Exact Mass: 519.1828

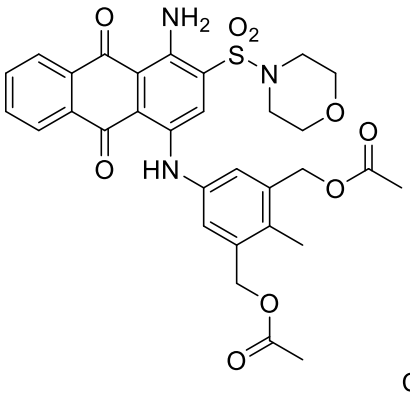

X-9525-51
Chemical Formula: $C_{31}H_{31}N_3O_9S$
Exact Mass: 621.1781

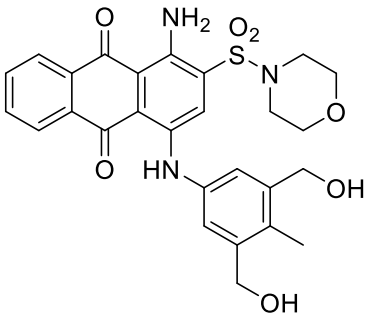

X-9525-56
Chemical Formula: $C_{27}H_{27}N_3O_7S$
Exact Mass: 537.1570

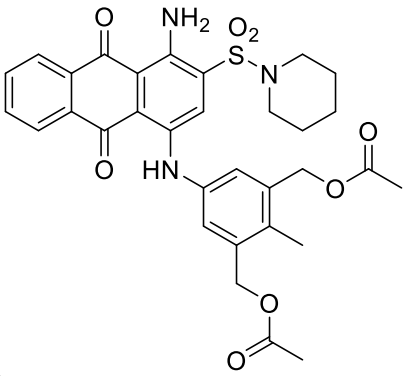

X-9525-60
Chemical Formula: $C_{32}H_{33}N_3O_8S$
Exact Mass: 619.1988

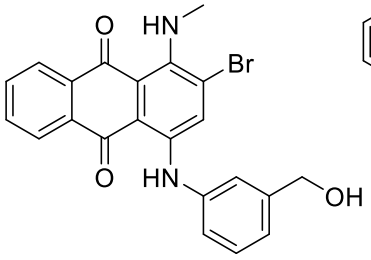

X-9525-102
Chemical Formula: $C_{22}H_{17}BrN_2O_3$
Exact Mass: 436.0423

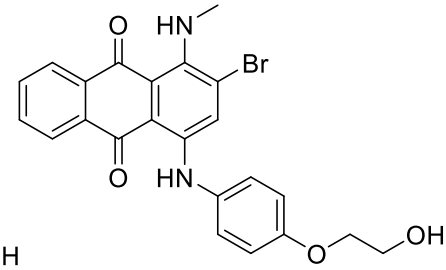

X-9525-103
Chemical Formula: $C_{23}H_{19}BrN_2O_4$
Exact Mass: 466.0528

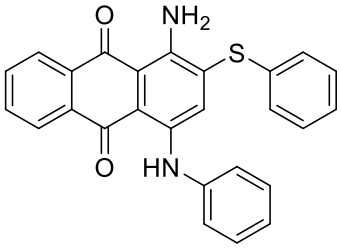

X-10161-21
Chemical Formula: $C_{26}H_{18}N_2O_2S$
Exact Mass: 422.1089

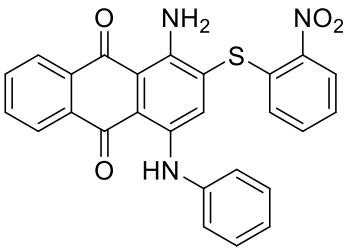

X-10161-70
Chemical Formula: $C_{26}H_{17}N_3O_4S$
Exact Mass: 467.0940

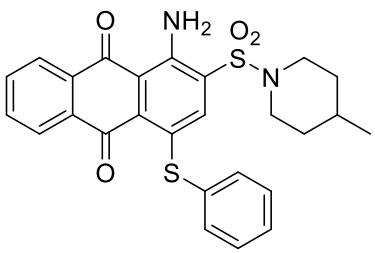

X-10161-91
Chemical Formula: $C_{26}H_{24}N_2O_4S_2$
Exact Mass: 492.1177

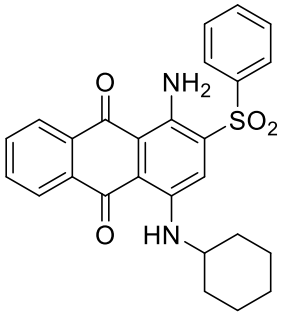

X-10469-71
Chemical Formula: $C_{26}H_{24}N_2O_4S$
Exact Mass: 460.1457

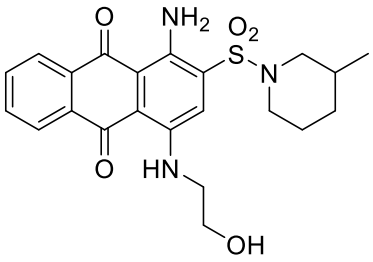

X-10469-103

Chemical Formula: $C_{22}H_{25}N_3O_5S$

Exact Mass: 443.1515

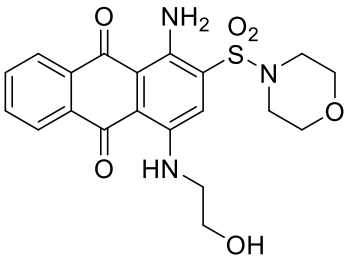

X-10469-110

Chemical Formula: $C_{20}H_{21}N_3O_6S$

Exact Mass: 431.1151

APPENDIX. B

254nm DAD chromatogram and MS spectrum at retention time

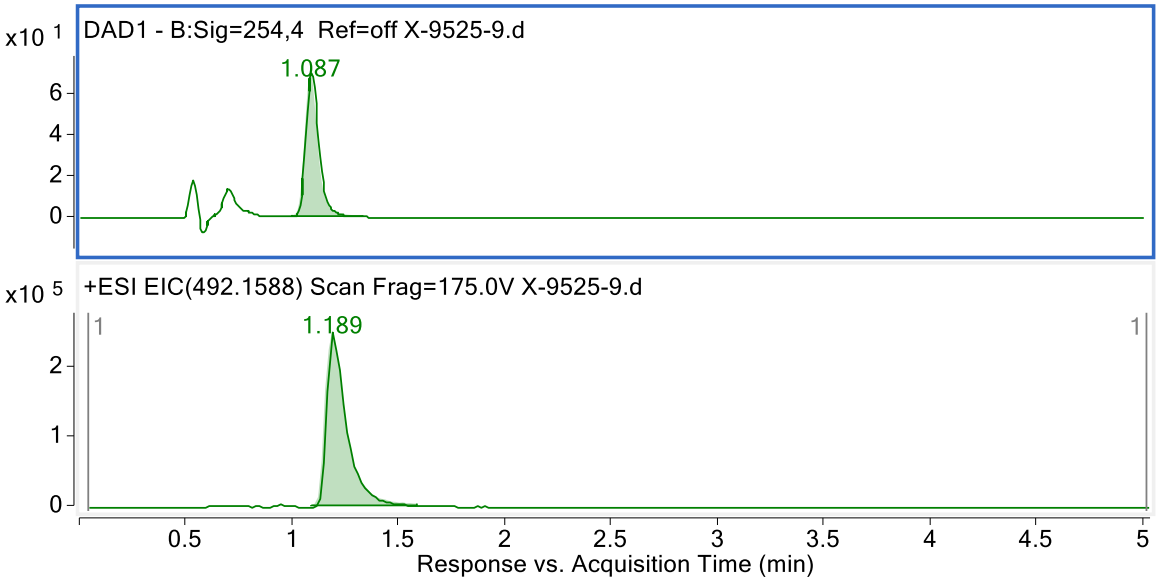

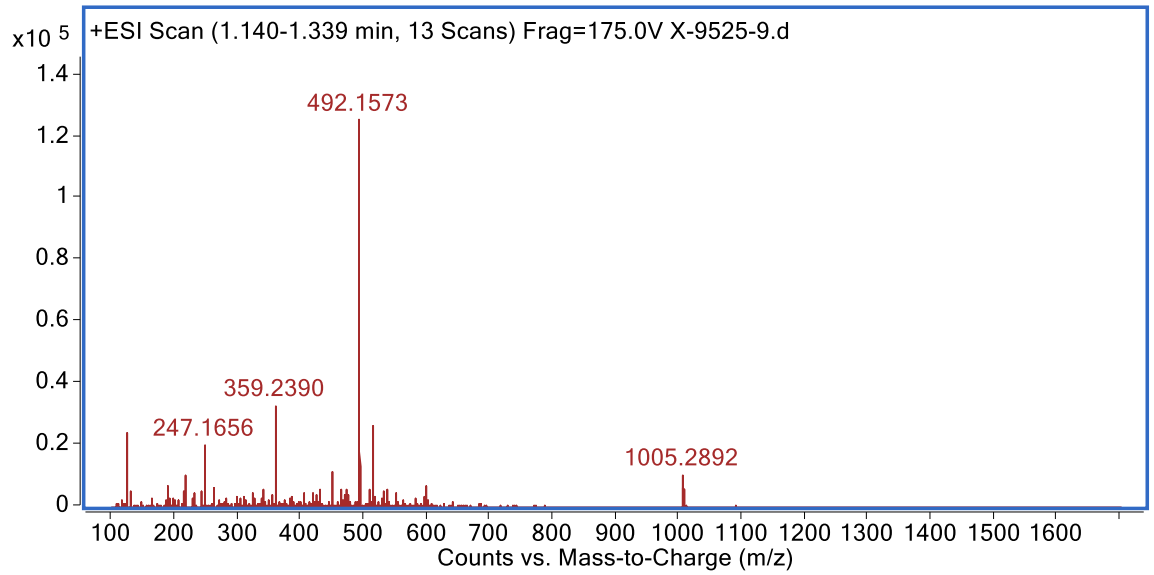

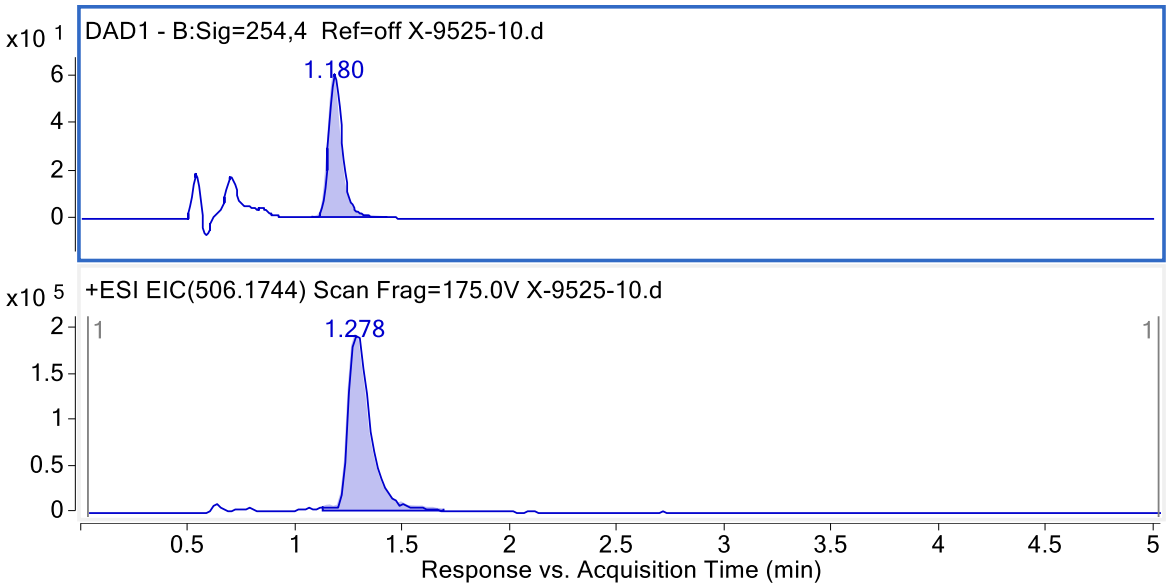
DAD1 - B:Sig=254,4 Ref=off X-9525-10.d
1.180
x10 1
+ESI EIC(506.1744) Scan Frag=175.0V X-9525-10.d
1.278
x10 5
Response vs. Acquisition Time (min)

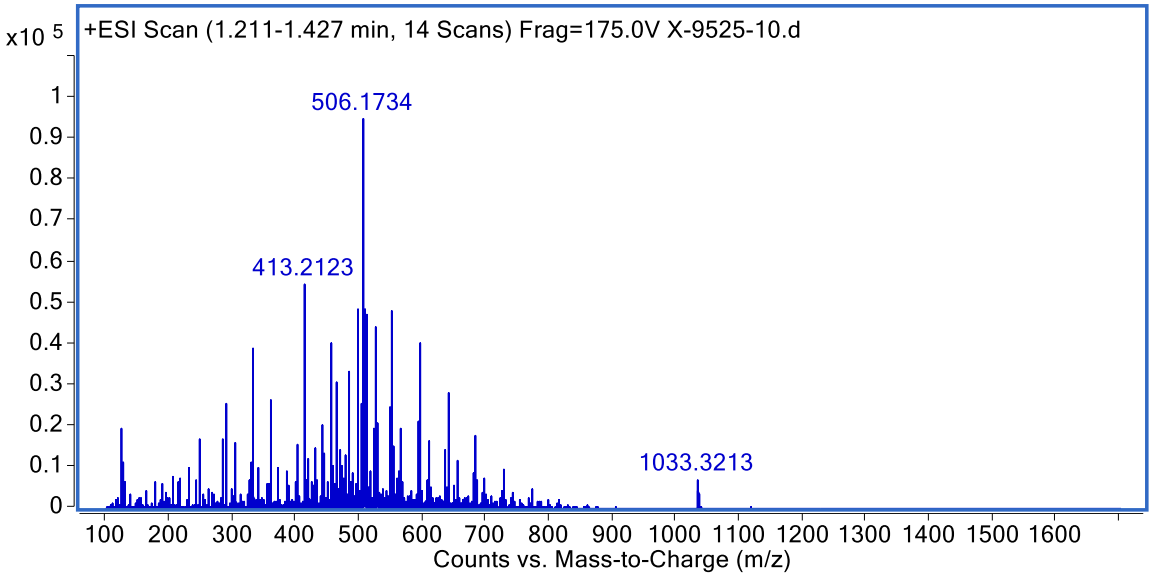
+ESI Scan (1.211-1.427 min, 14 Scans) Frag=175.0V X-9525-10.d
506.1734
413.2123
1033.3213
x10 5
Counts vs. Mass-to-Charge (m/z)

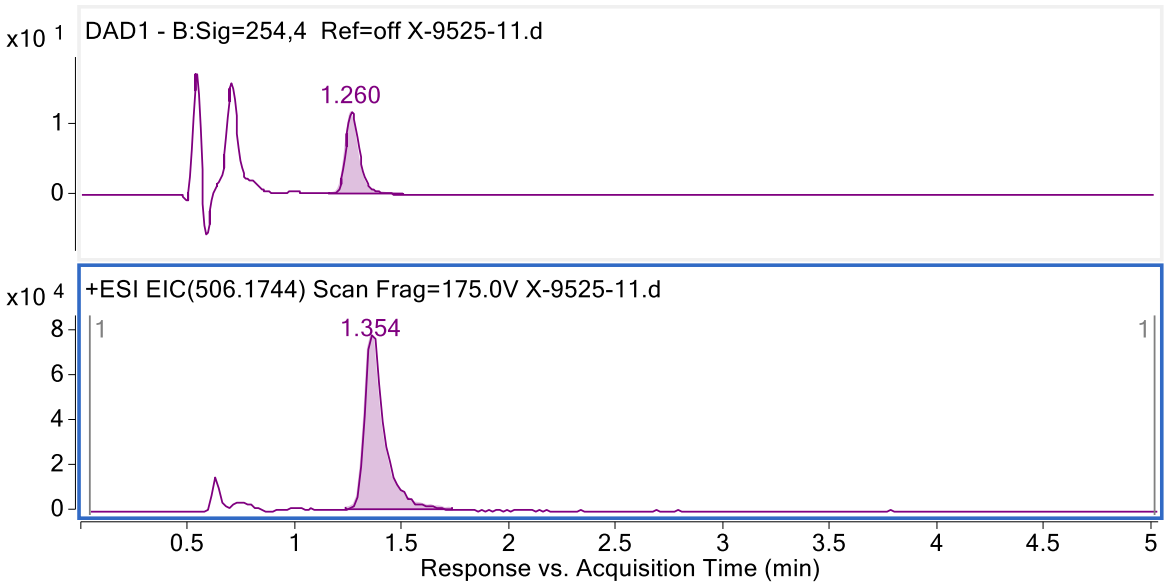
x10 1
DAD1 - B:Sig=254,4 Ref=off X-9525-11.d
1.260
1
0
x10 4
+ESI EIC(506.1744) Scan Frag=175.0V X-9525-11.d
1.354
8
6
4
2
0
0.5
1
1.5
2
2.5
3
3.5
4
4.5
5
Response vs. Acquisition Time (min)

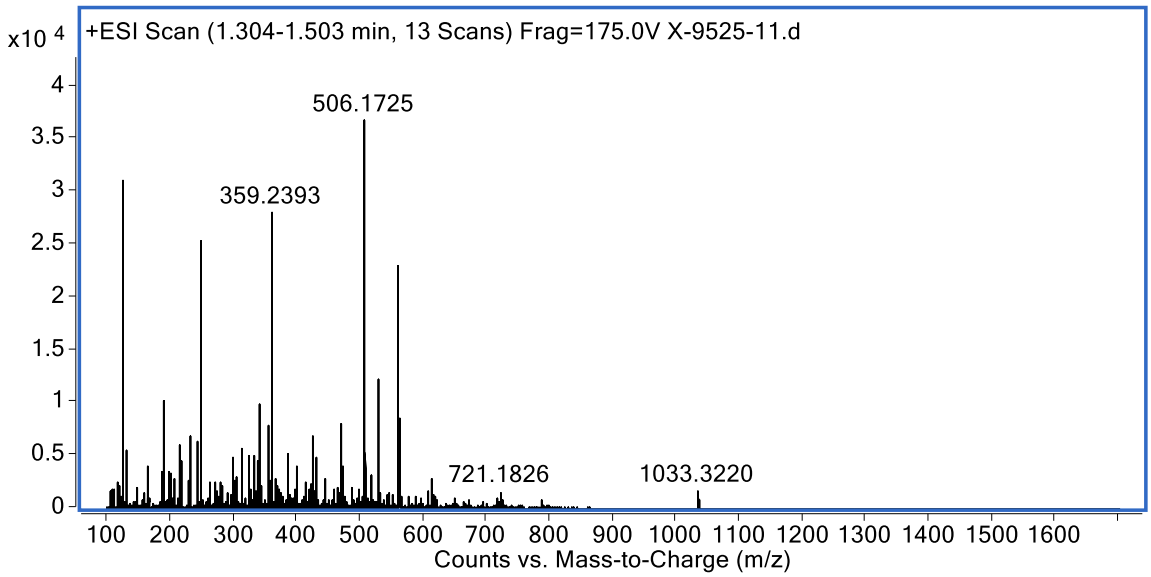
x10 4
+ESI Scan (1.304-1.503 min, 13 Scans) Frag=175.0V X-9525-11.d
506.1725
359.2393
721.1826
1033.3220
4
3.5
3
2.5
2
1.5
1
0.5
0
100 200 300 400 500 600 700 800 900 1000 1100 1200 1300 1400 1500 1600
Counts vs. Mass-to-Charge (m/z)

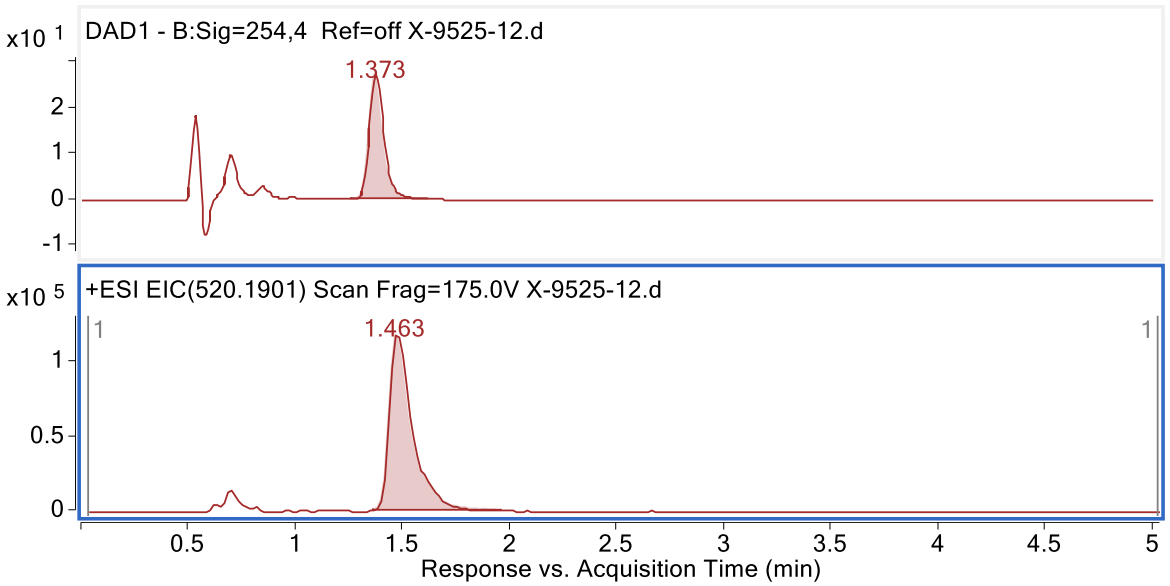
x10 1
DAD1 - B:Sig=254,4 Ref=off X-9525-12.d
1.373
2
1
0
-1
x10 5
+ESI EIC(520.1901) Scan Frag=175.0V X-9525-12.d
1
1.463
1
1
0.5
0
0.5
1
1.5
2
2.5
3
3.5
4
4.5
5
Response vs. Acquisition Time (min)

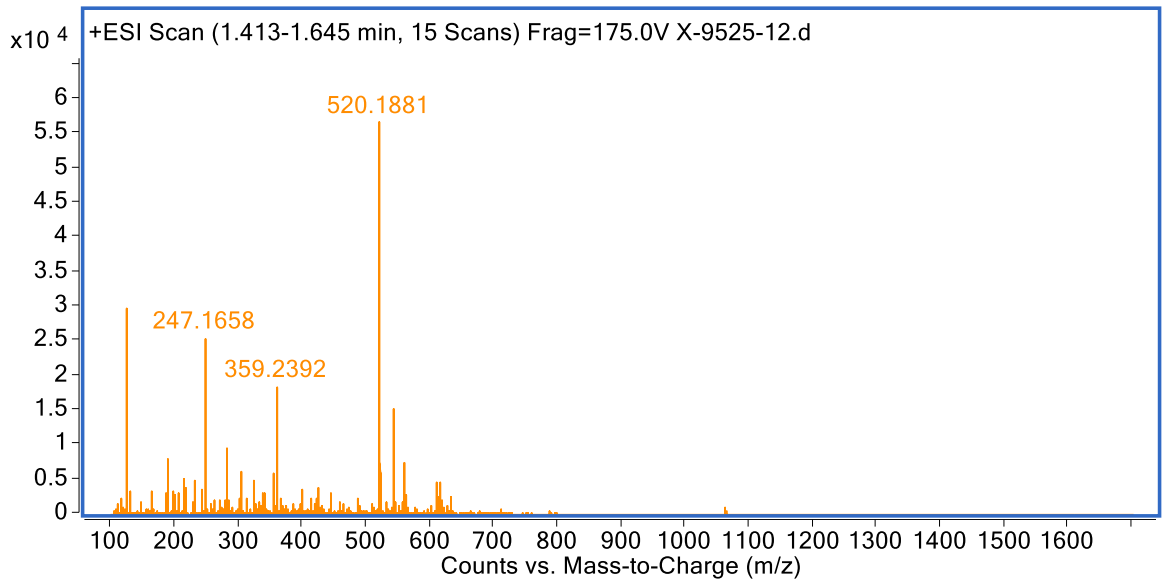
x10 4
+ESI Scan (1.413-1.645 min, 15 Scans) Frag=175.0V X-9525-12.d
520.1881
247.1658
359.2392
6
5.5
5
4.5
4
3.5
3
2.5
2
1.5
1
0.5
0
100
200
300
400
500
600
700
800
900
1000
1100
1200
1300
1400
1500
1600
Counts vs. Mass-to-Charge (m/z)

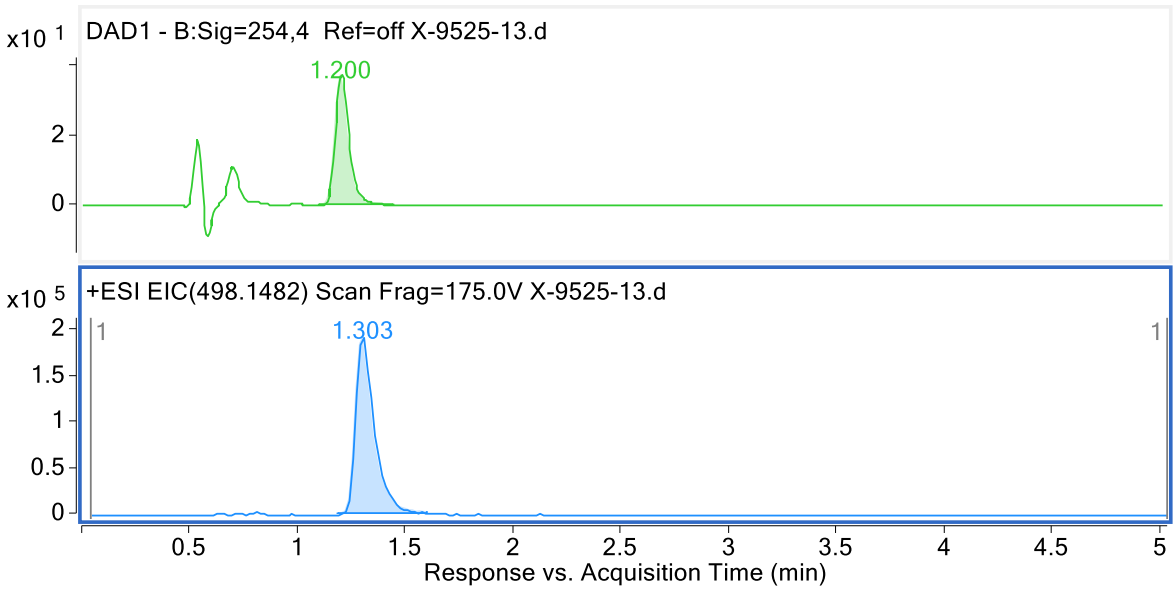
x10 1
DAD1 - B:Sig=254,4 Ref=off X-9525-13.d
1.200
2
0
x10 5
+ESI EIC(498.1482) Scan Frag=175.0V X-9525-13.d
1
1.303
1
2
1.5
1
0.5
0
0.5
1
1.5
2
2.5
3
3.5
4
4.5
5
Response vs. Acquisition Time (min)

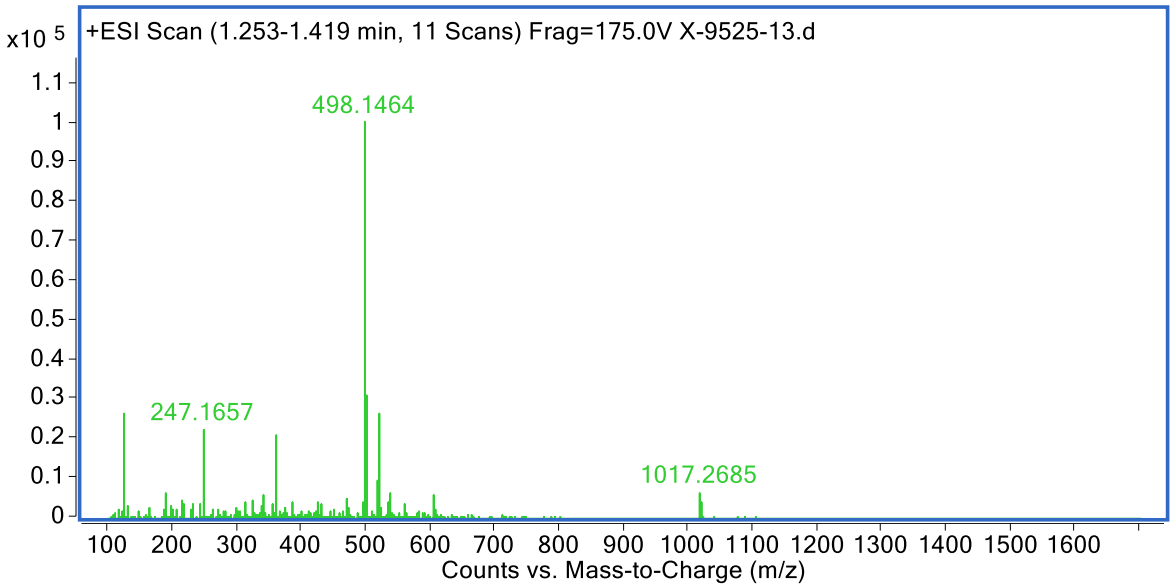
x10 5
+ESI Scan (1.253-1.419 min, 11 Scans) Frag=175.0V X-9525-13.d
498.1464
247.1657
1017.2685
1.1
1
0.9
0.8
0.7
0.6
0.5
0.4
0.3
0.2
0.1
0
100
200
300
400
500
600
700
800
900
1000
1100
1200
1300
1400
1500
1600
Counts vs. Mass-to-Charge (m/z)

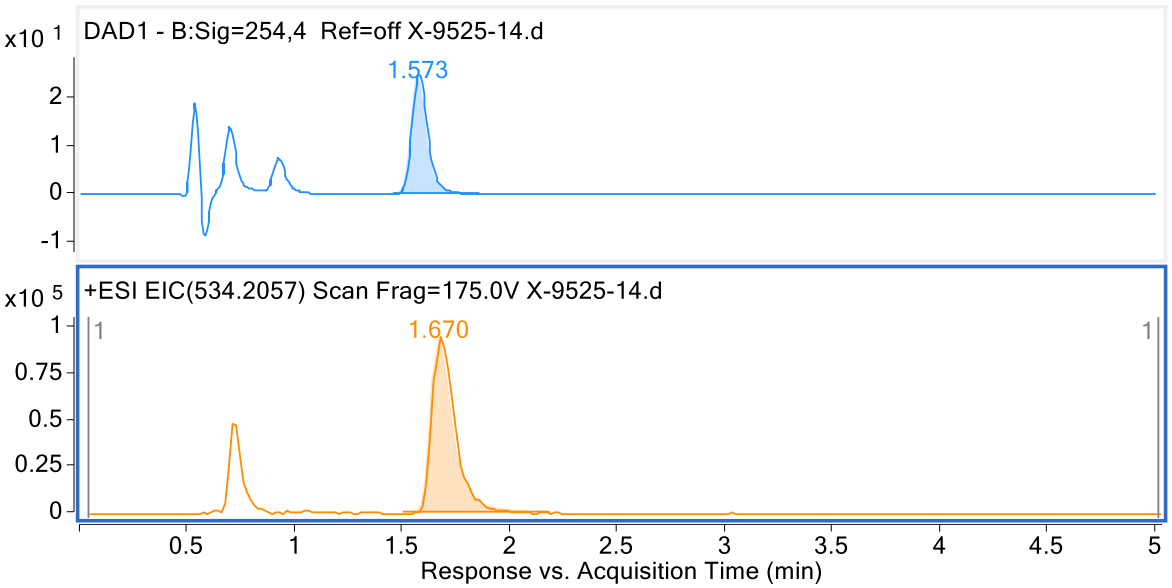
DAD1 - B:Sig=254,4 Ref=off X-9525-14.d
x10 1
1.573
+ESI EIC(534.2057) Scan Frag=175.0V X-9525-14.d
x10 5
1.670
Response vs. Acquisition Time (min)

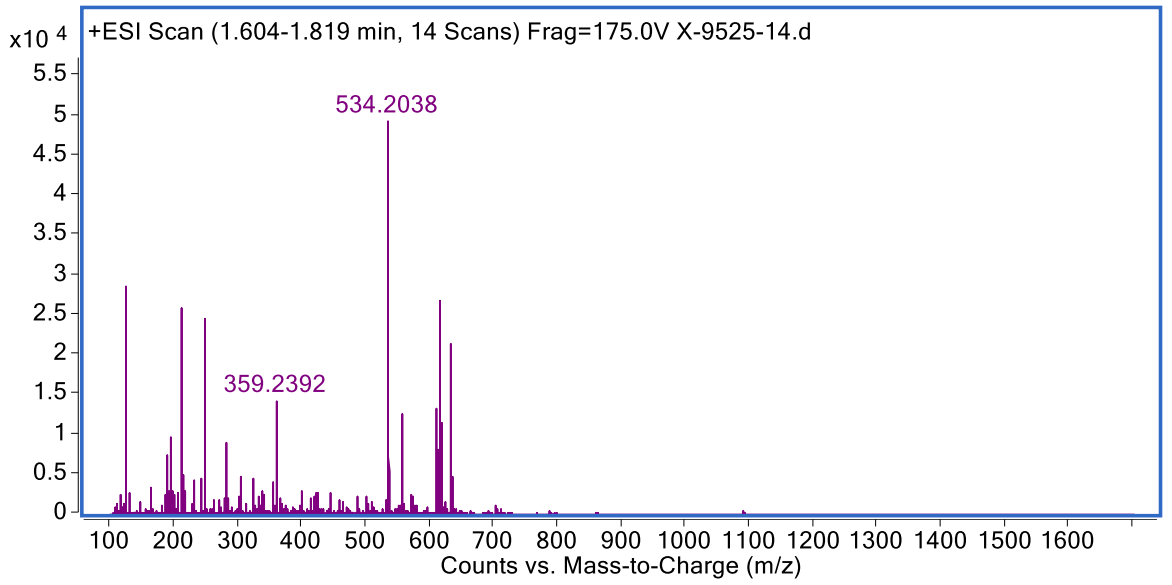
+ESI Scan (1.604-1.819 min, 14 Scans) Frag=175.0V X-9525-14.d
x10 4
534.2038
359.2392
Counts vs. Mass-to-Charge (m/z)

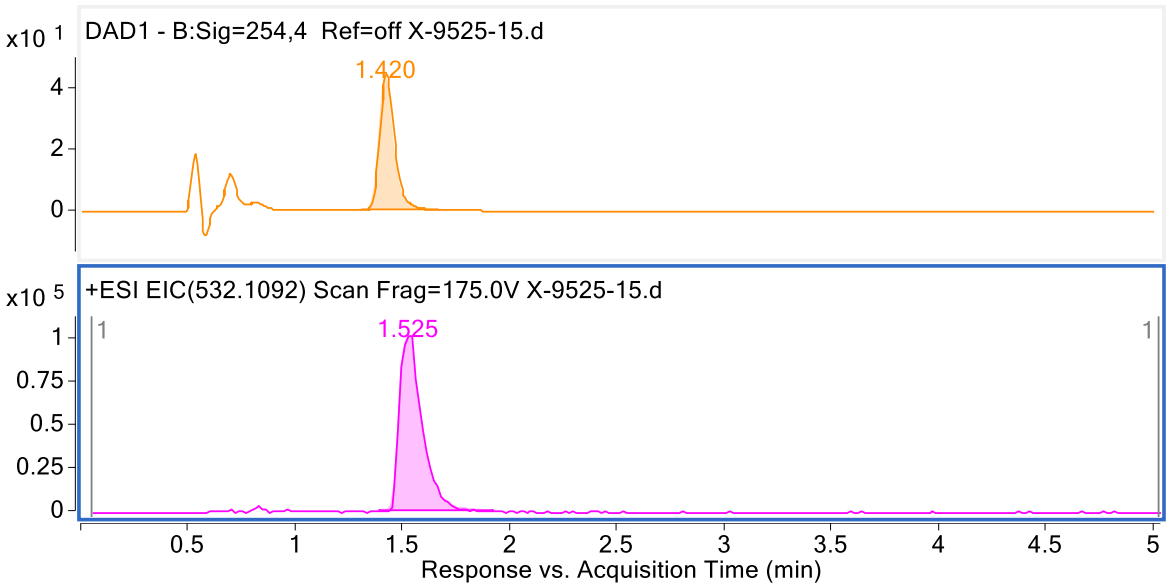
x10 1
DAD1 - B:Sig=254,4 Ref=off X-9525-15.d
1.420
4
2
0
x10 5
+ESI EIC(532.1092) Scan Frag=175.0V X-9525-15.d
1
1.525
1
1
0.75
0.5
0.25
0
0.5
1
1.5
2
2.5
3
3.5
4
4.5
5
Response vs. Acquisition Time (min)

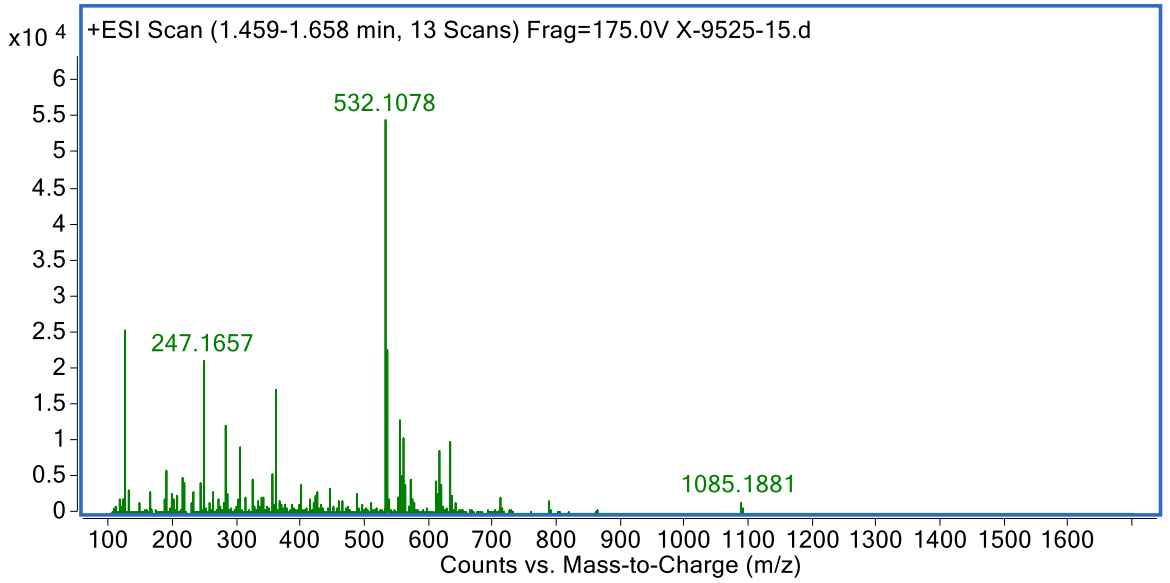
x10 4
+ESI Scan (1.459-1.658 min, 13 Scans) Frag=175.0V X-9525-15.d
532.1078
247.1657
1085.1881
6
5.5
5
4.5
4
3.5
3
2.5
2
1.5
1
0.5
0
100 200 300 400 500 600 700 800 900 1000 1100 1200 1300 1400 1500 1600
Counts vs. Mass-to-Charge (m/z)

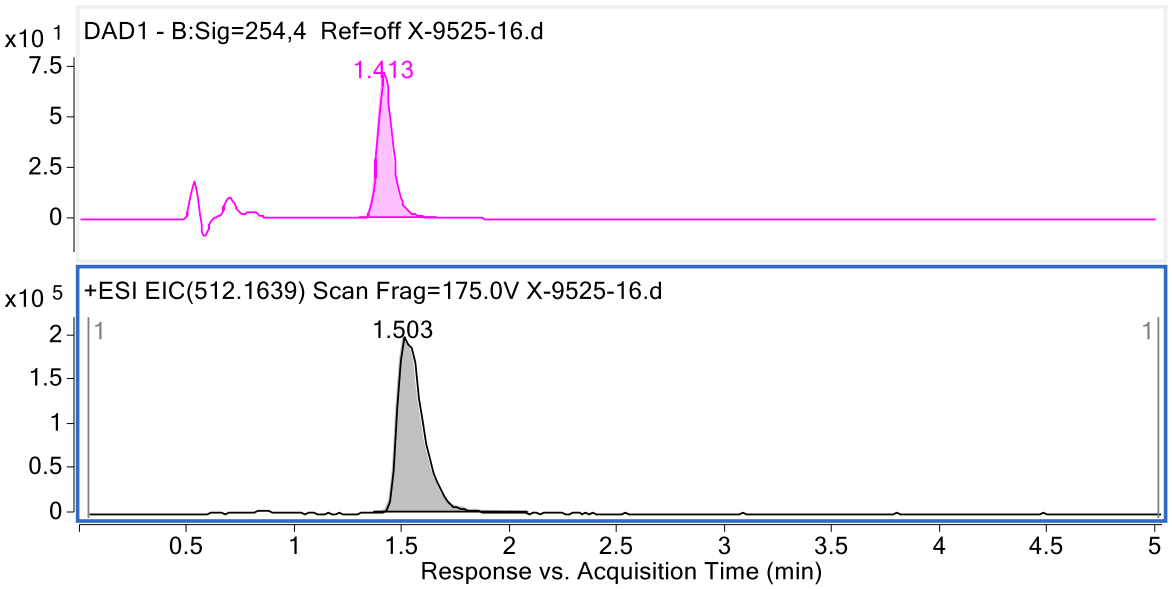
x10 1
DAD1 - B:Sig=254,4 Ref=off X-9525-16.d
1.413
7.5
5
2.5
0
x10 5
+ESI EIC(512.1639) Scan Frag=175.0V X-9525-16.d
1.503
2
1.5
1
0.5
0
0.5 1 1.5 2 2.5 3 3.5 4 4.5 5
Response vs. Acquisition Time (min)

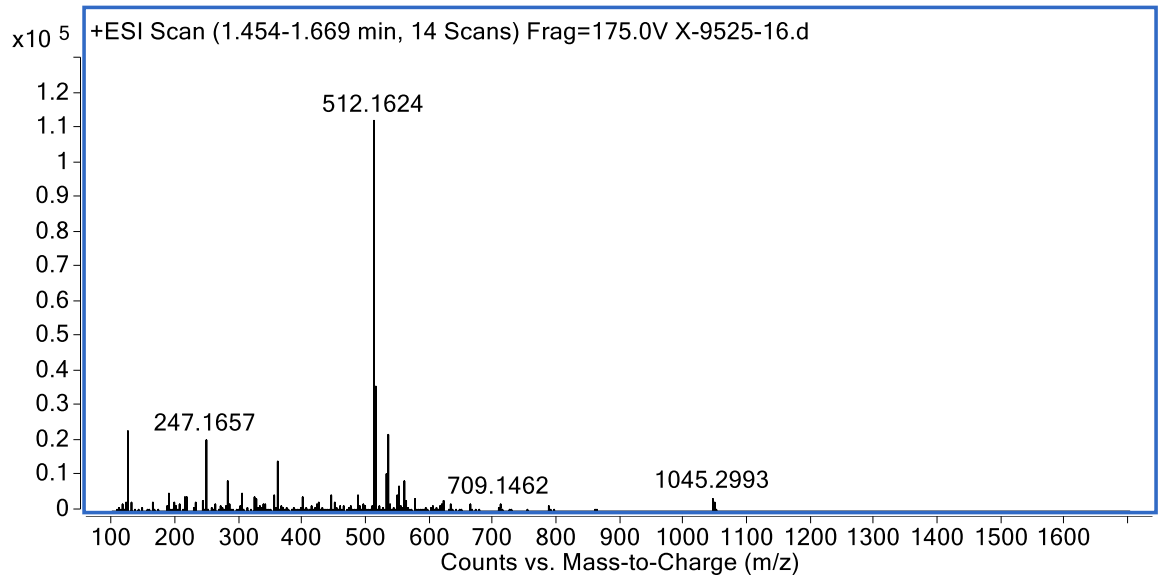
x10 5
+ESI Scan (1.454-1.669 min, 14 Scans) Frag=175.0V X-9525-16.d
512.1624
247.1657
709.1462
1045.2993
1.2
1.1
1
0.9
0.8
0.7
0.6
0.5
0.4
0.3
0.2
0.1
0
100 200 300 400 500 600 700 800 900 1000 1100 1200 1300 1400 1500 1600
Counts vs. Mass-to-Charge (m/z)

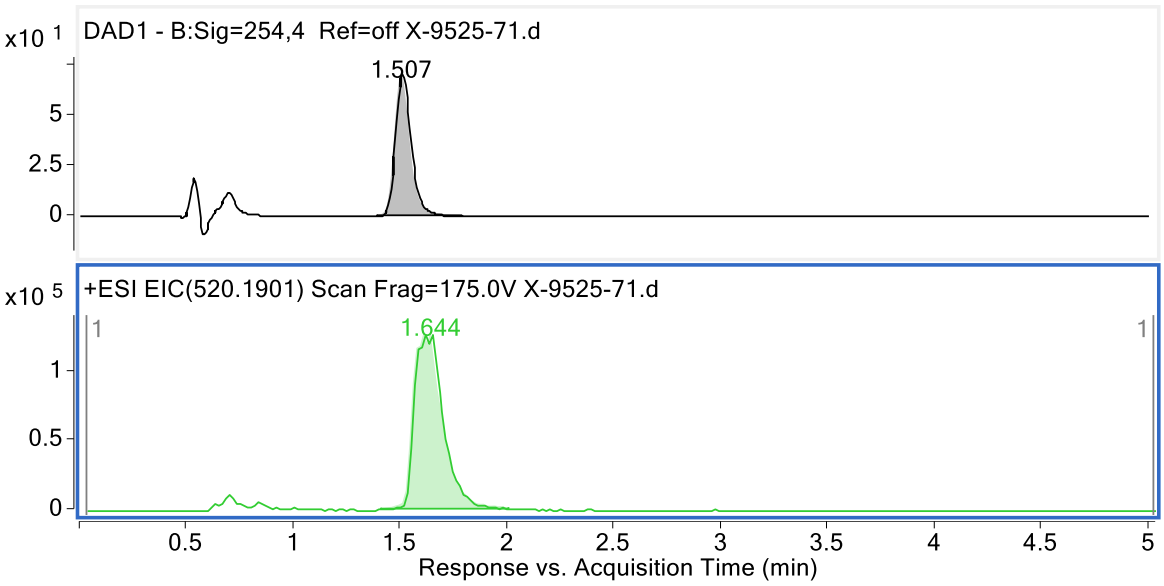
x10 1
DAD1 - B:Sig=254,4 Ref=off X-9525-71.d
1.507
5
2.5
0
x10 5
+ESI EIC(520.1901) Scan Frag=175.0V X-9525-71.d
1
1.644
1
1
0.5
0
0.5
1
1.5
2
2.5
3
3.5
4
4.5
5
Response vs. Acquisition Time (min)

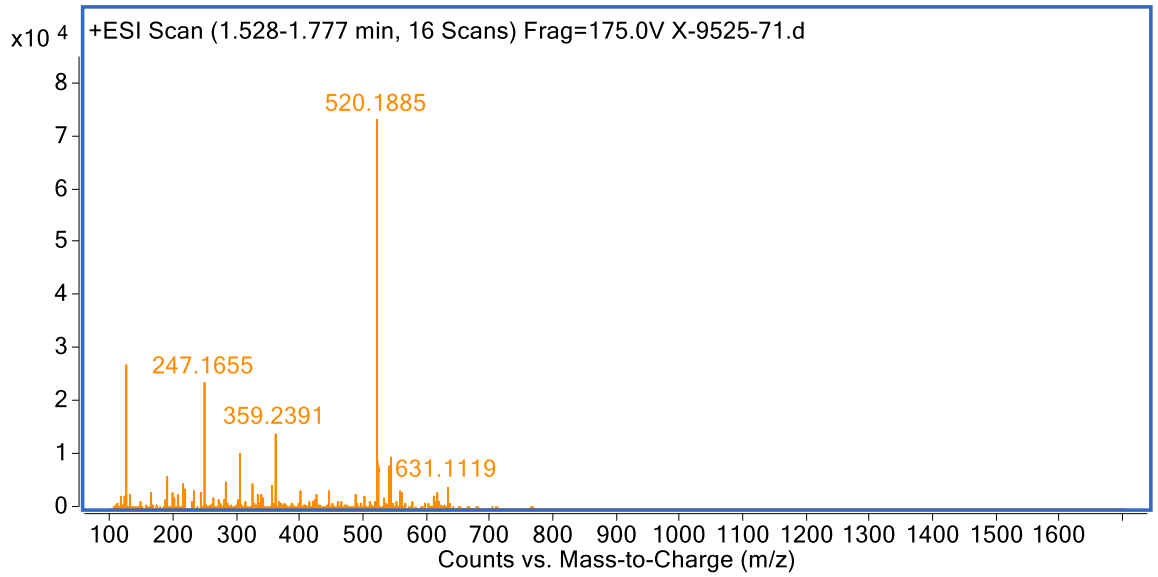
x10 4
+ESI Scan (1.528-1.777 min, 16 Scans) Frag=175.0V X-9525-71.d
520.1885
8
7
6
5
4
3
2
1
0
247.1655
359.2391
631.1119
100
200
300
400
500
600
700
800
900
1000
1100
1200
1300
1400
1500
1600
Counts vs. Mass-to-Charge (m/z)

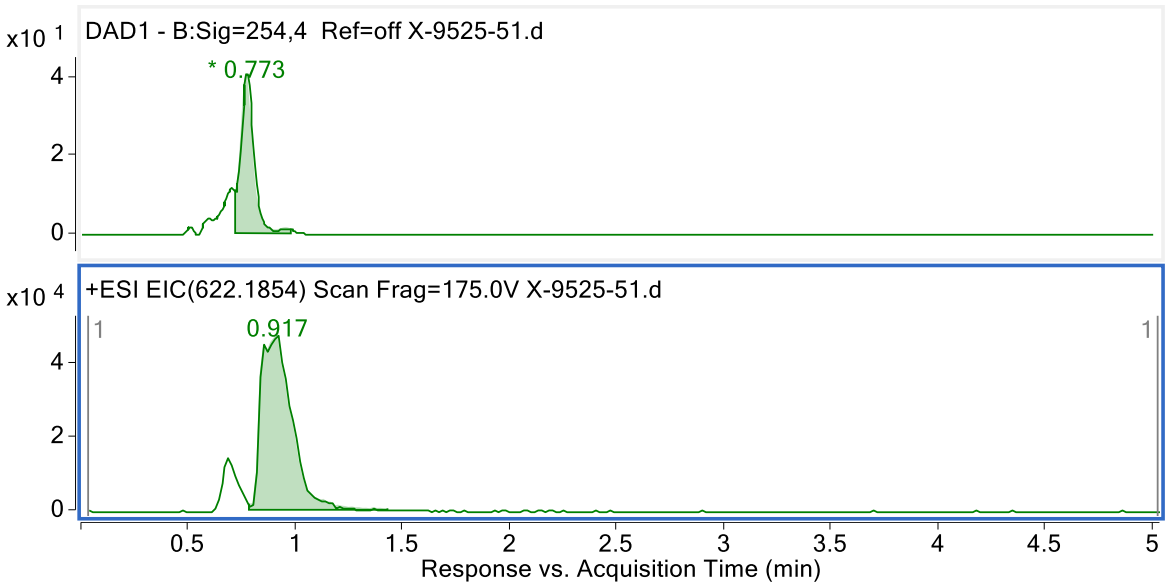
x10 1
DAD1 - B:Sig=254,4 Ref=off X-9525-51.d
* 0.773
4
2
0
x10 4
+ESI EIC(622.1854) Scan Frag=175.0V X-9525-51.d
1
0.917
1
4
2
0
0.5
1
1.5
2
2.5
3
3.5
4
4.5
5
Response vs. Acquisition Time (min)

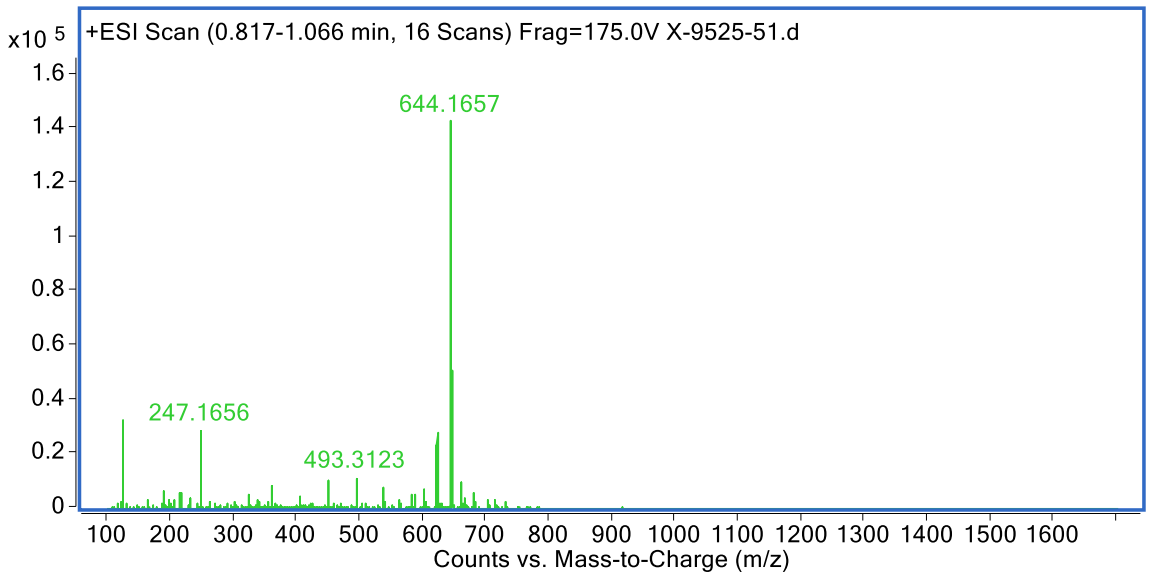
x10 5
+ESI Scan (0.817-1.066 min, 16 Scans) Frag=175.0V X-9525-51.d
644.1657
247.1656
493.3123
1.6
1.4
1.2
1
0.8
0.6
0.4
0.2
0
100
200
300
400
500
600
700
800
900
1000
1100
1200
1300
1400
1500
1600
Counts vs. Mass-to-Charge (m/z)

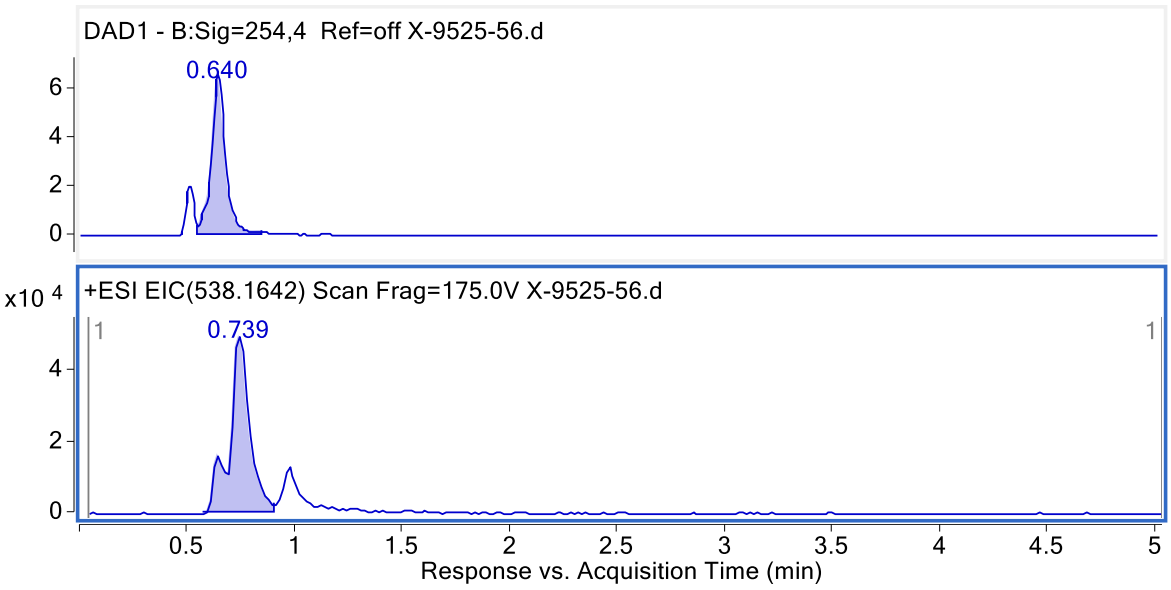
DAD1 - B:Sig=254,4 Ref=off X-9525-56.d
0.640
6
4
2
0
x10 4
+ESI EIC(538.1642) Scan Frag=175.0V X-9525-56.d
1
0.739
1
4
2
0
0.5
1
1.5
2
2.5
3
3.5
4
4.5
5
Response vs. Acquisition Time (min)

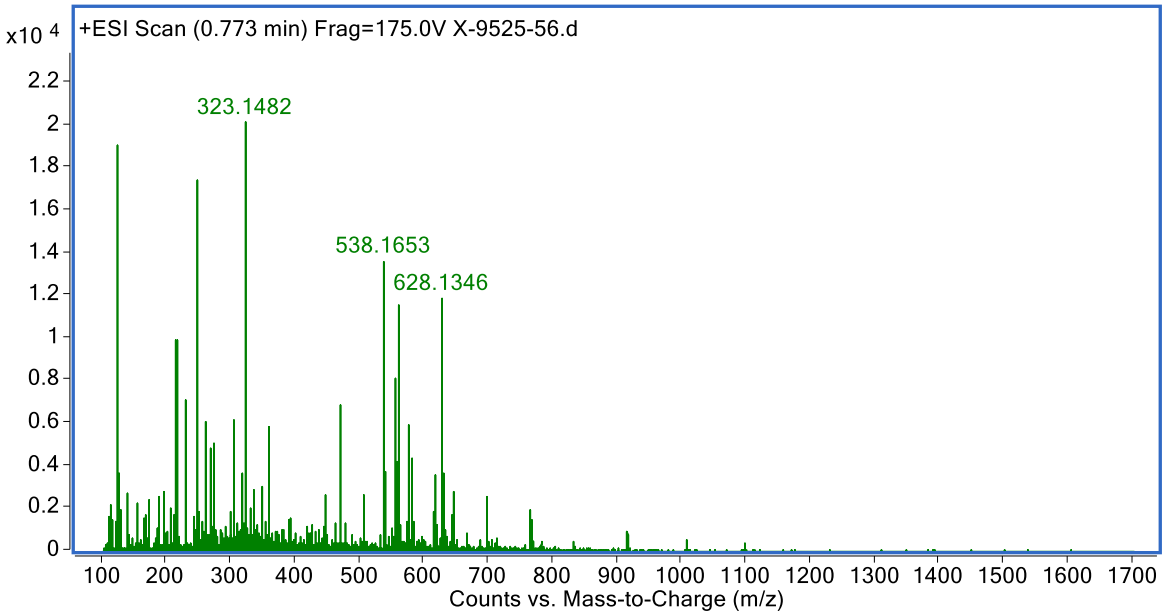
x10 4
+ESI Scan (0.773 min) Frag=175.0V X-9525-56.d
323.1482
538.1653
628.1346
2.2
2
1.8
1.6
1.4
1.2
1
0.8
0.6
0.4
0.2
0
100
200
300
400
500
600
700
800
900
1000
1100
1200
1300
1400
1500
1600
1700
Counts vs. Mass-to-Charge (m/z)

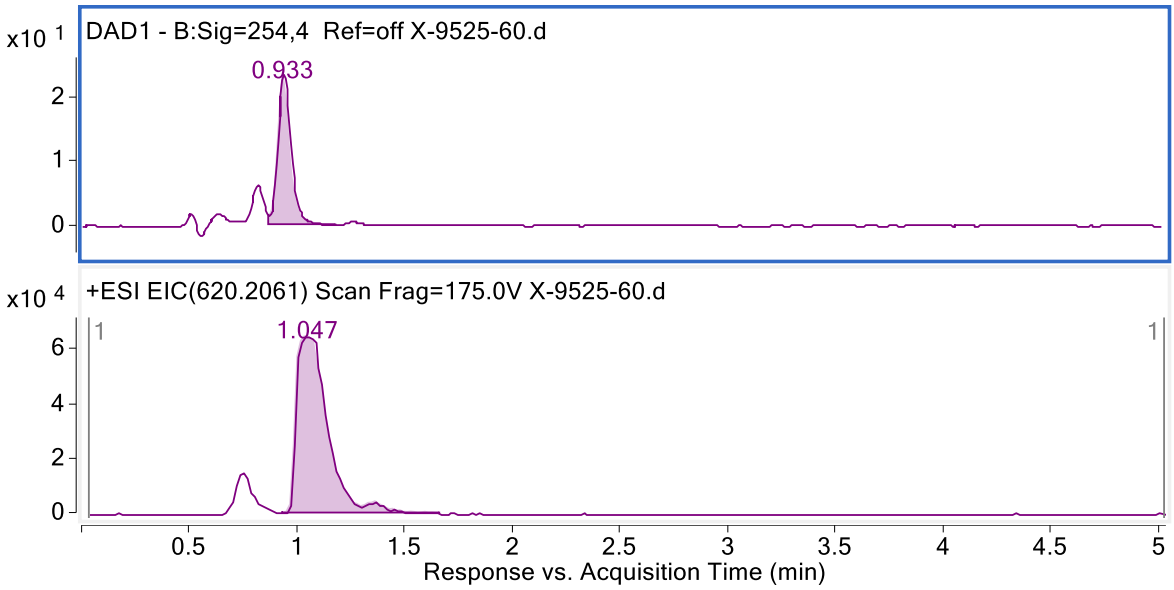
DAD1 - B:Sig=254,4 Ref=off X-9525-60.d
0.933
+ESI EIC(620.2061) Scan Frag=175.0V X-9525-60.d
1.047
Response vs. Acquisition Time (min)

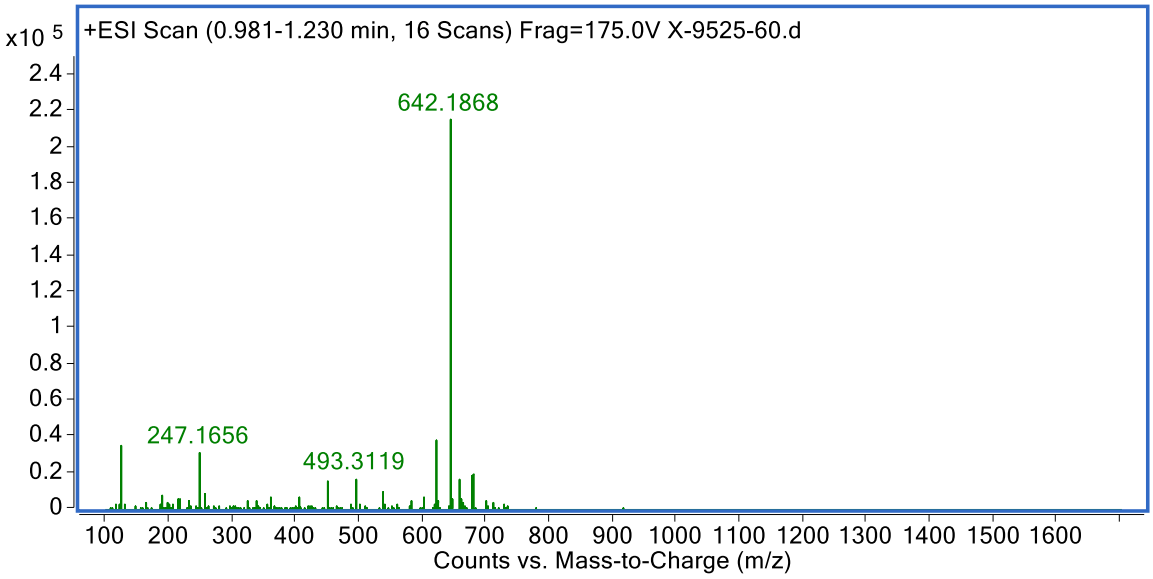
+ESI Scan (0.981-1.230 min, 16 Scans) Frag=175.0V X-9525-60.d
642.1868
247.1656
493.3119
Counts vs. Mass-to-Charge (m/z)

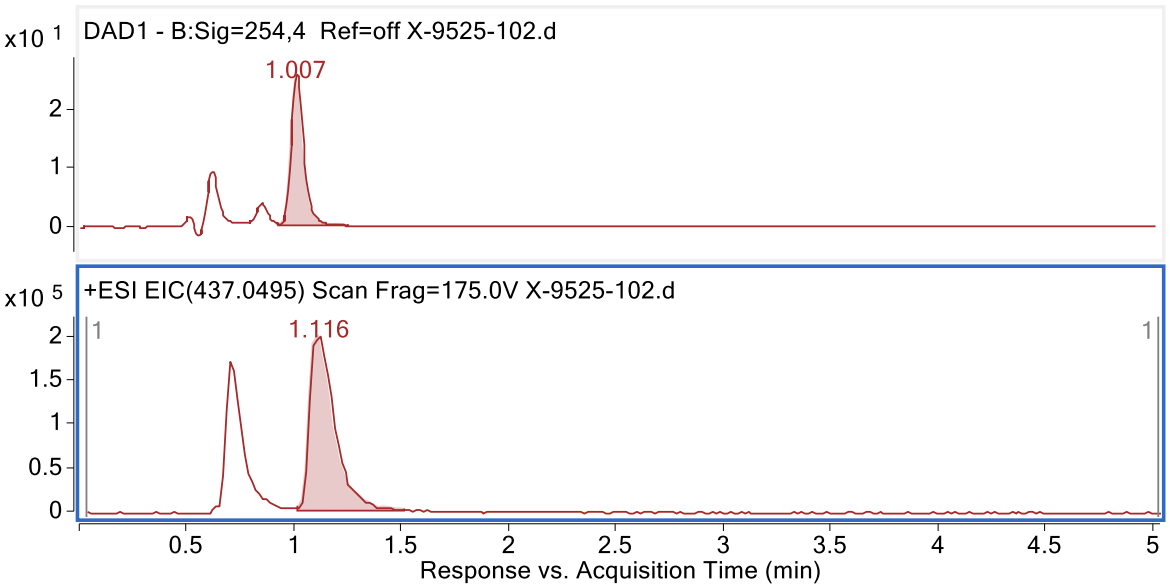
x10 1
DAD1 - B:Sig=254,4 Ref=off X-9525-102.d
1.007
2
1
0
x10 5
+ESI EIC(437.0495) Scan Frag=175.0V X-9525-102.d
1
1.116
1
2
1.5
1
0.5
0
0.5
1
1.5
2
2.5
3
3.5
4
4.5
5
Response vs. Acquisition Time (min)

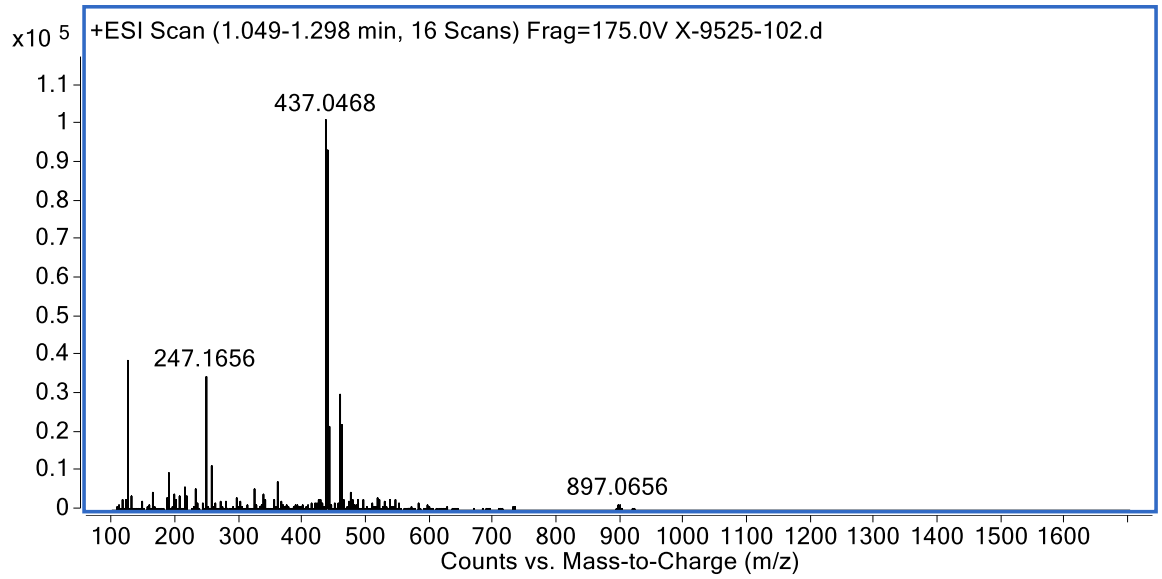
x10 5
+ESI Scan (1.049-1.298 min, 16 Scans) Frag=175.0V X-9525-102.d
437.0468
247.1656
897.0656
1.1
1
0.9
0.8
0.7
0.6
0.5
0.4
0.3
0.2
0.1
0
100
200
300
400
500
600
700
800
900
1000
1100
1200
1300
1400
1500
1600
Counts vs. Mass-to-Charge (m/z)

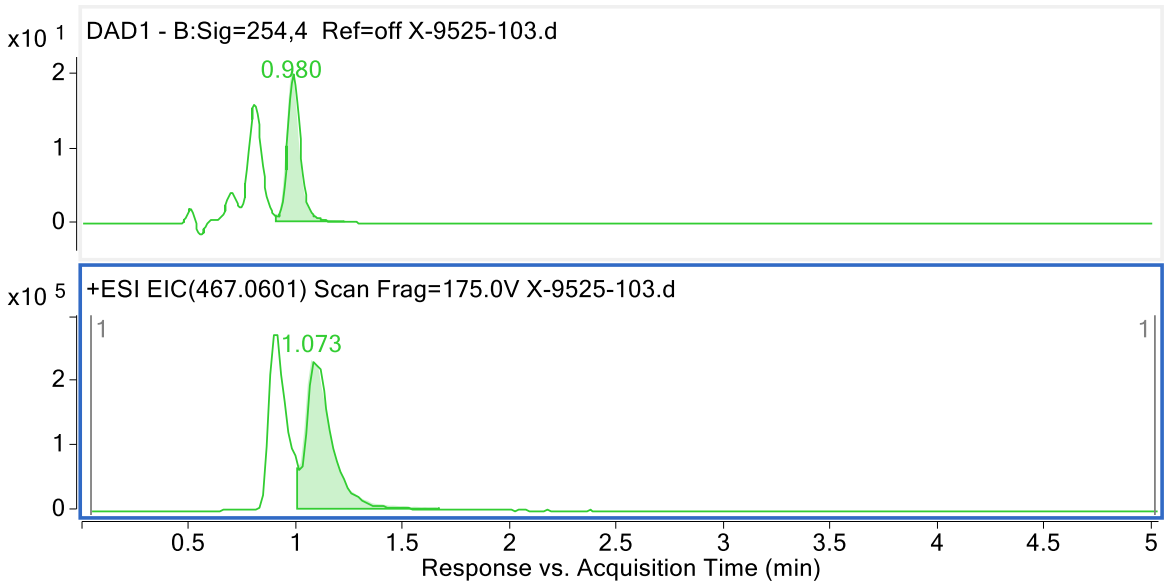
x10 1
DAD1 - B:Sig=254,4 Ref=off X-9525-103.d
0.980
x10 5
+ESI EIC(467.0601) Scan Frag=175.0V X-9525-103.d
1.073
Response vs. Acquisition Time (min)

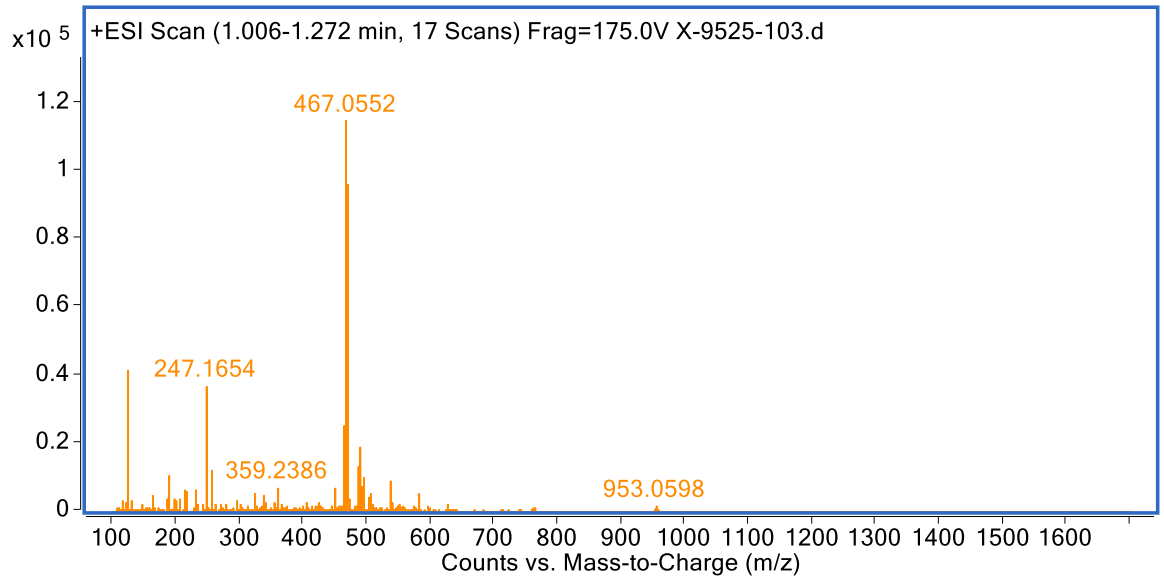
x10 5
+ESI Scan (1.006-1.272 min, 17 Scans) Frag=175.0V X-9525-103.d
467.0552
247.1654
359.2386
953.0598
Counts vs. Mass-to-Charge (m/z)

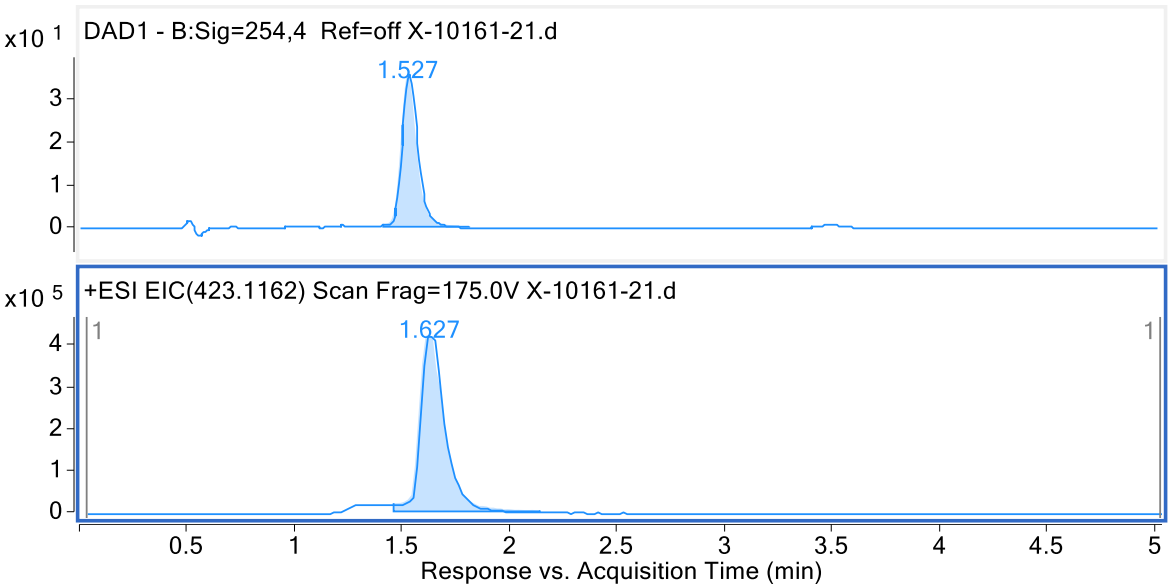
x10 1
DAD1 - B:Sig=254,4 Ref=off X-10161-21.d
1.527
3
2
1
0
x10 5
+ESI EIC(423.1162) Scan Frag=175.0V X-10161-21.d
1
1.627
1
4
3
2
1
0
0.5
1
1.5
2
2.5
3
3.5
4
4.5
5
Response vs. Acquisition Time (min)

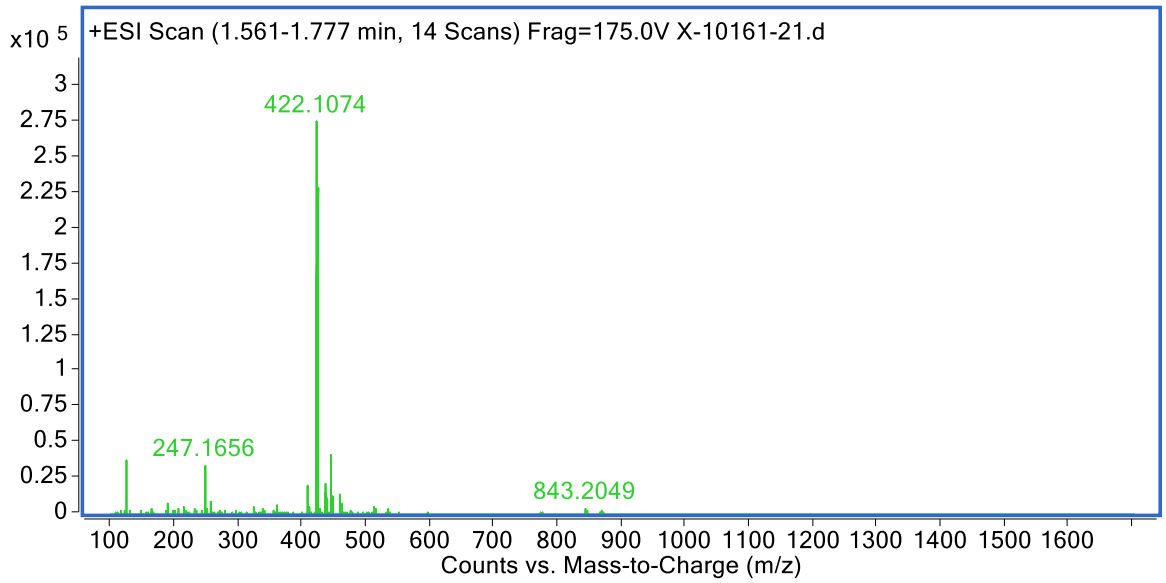
x10 5
+ESI Scan (1.561-1.777 min, 14 Scans) Frag=175.0V X-10161-21.d
422.1074
247.1656
843.2049
3
2.75
2.5
2.25
2
1.75
1.5
1.25
1
0.75
0.5
0.25
0
100 200 300 400 500 600 700 800 900 1000 1100 1200 1300 1400 1500 1600
Counts vs. Mass-to-Charge (m/z)

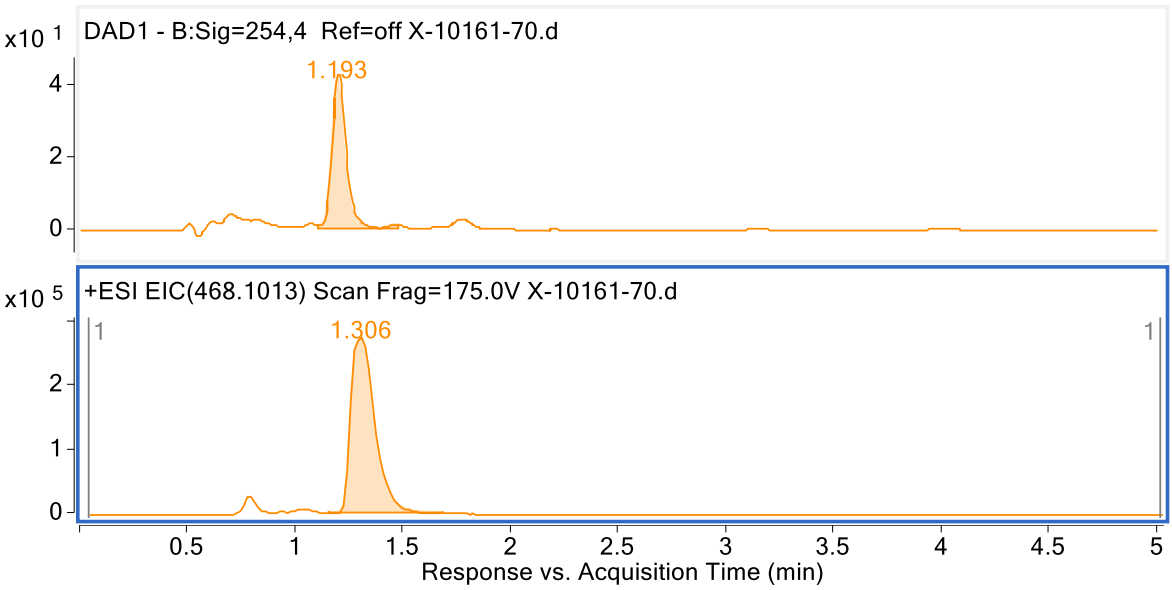
x10 1
DAD1 - B:Sig=254,4 Ref=off X-10161-70.d
1.193
4
2
0
x10 5
+ESI EIC(468.1013) Scan Frag=175.0V X-10161-70.d
1
1.306
1
2
1
0
0.5
1
1.5
2
2.5
3
3.5
4
4.5
5
Response vs. Acquisition Time (min)

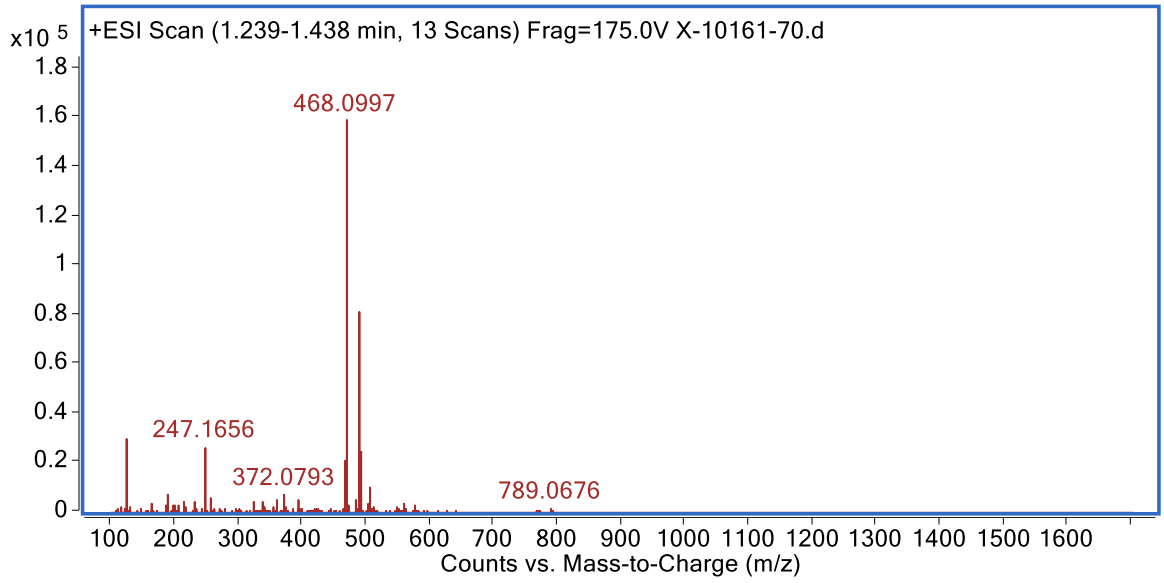
x10 5
+ESI Scan (1.239-1.438 min, 13 Scans) Frag=175.0V X-10161-70.d
1.8
1.6
1.4
1.2
1
0.8
0.6
0.4
0.2
0
468.0997
247.1656
372.0793
789.0676
100
200
300
400
500
600
700
800
900
1000
1100
1200
1300
1400
1500
1600
Counts vs. Mass-to-Charge (m/z)

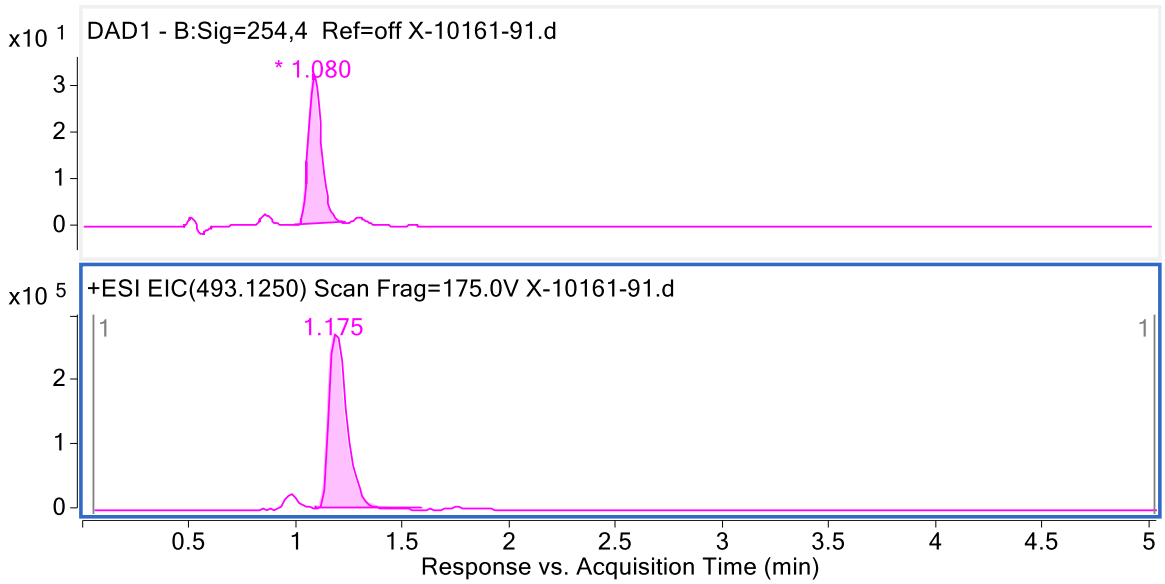
x10 1
DAD1 - B:Sig=254,4 Ref=off X-10161-91.d
* 1.080
3
2
1
0
x10 5
+ESI EIC(493.1250) Scan Frag=175.0V X-10161-91.d
1
1.175
1
2
1
0
0.5
1
1.5
2
2.5
3
3.5
4
4.5
5
Response vs. Acquisition Time (min)

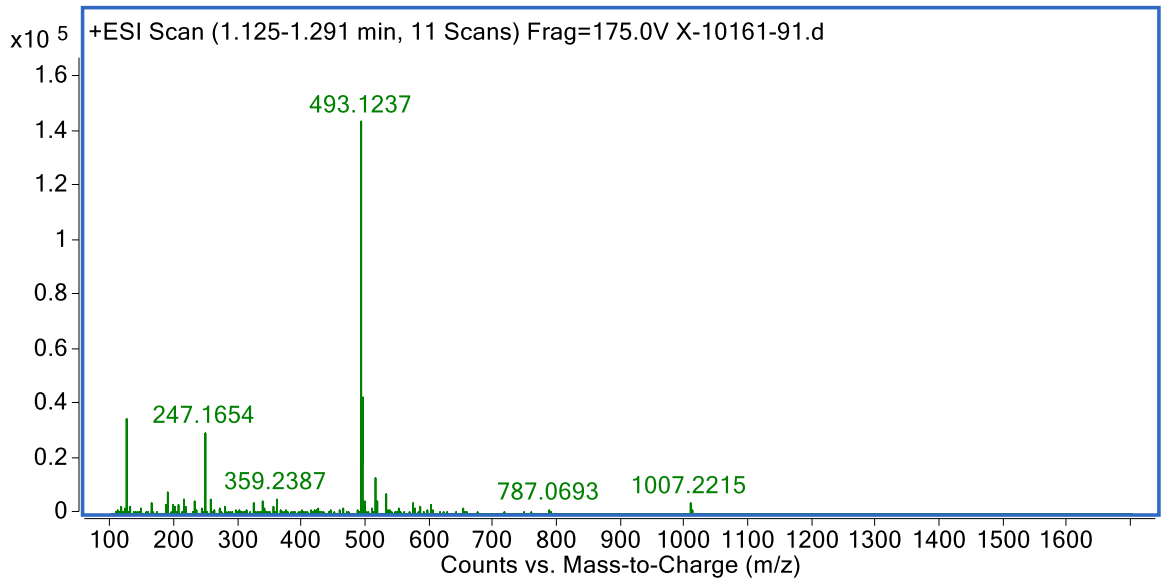
x10 5
+ESI Scan (1.125-1.291 min, 11 Scans) Frag=175.0V X-10161-91.d
493.1237
1.6
1.4
1.2
1
0.8
0.6
0.4
0.2
0
247.1654
359.2387
787.0693
1007.2215
100
200
300
400
500
600
700
800
900
1000
1100
1200
1300
1400
1500
1600
Counts vs. Mass-to-Charge (m/z)

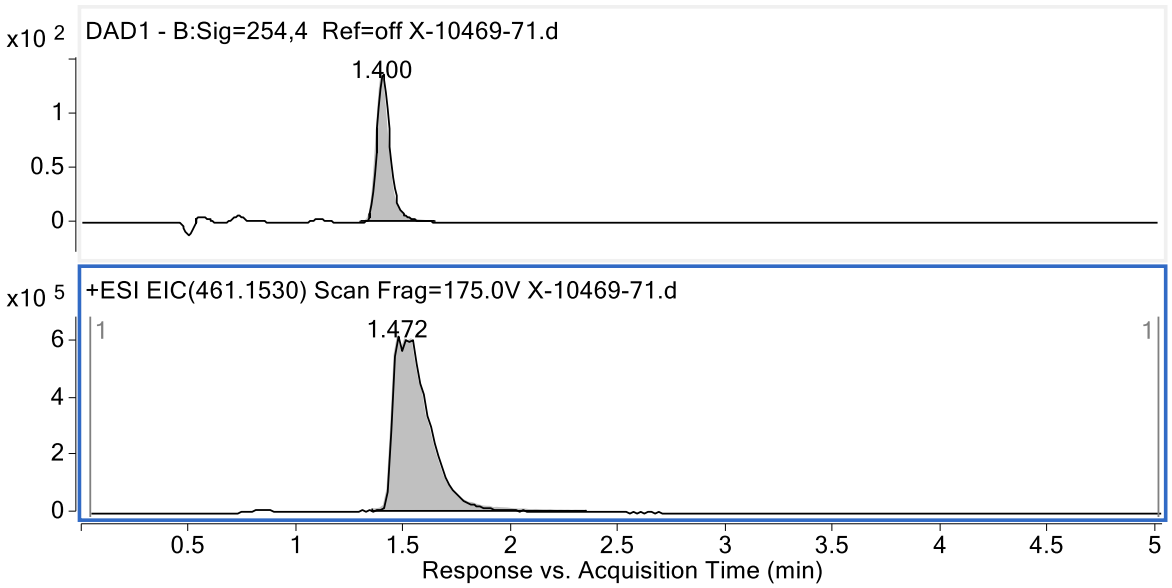
x10 2
DAD1 - B:Sig=254,4 Ref=off X-10469-71.d
1.400
1
0.5
0
x10 5
+ESI EIC(461.1530) Scan Frag=175.0V X-10469-71.d
1
1.472
1
6
4
2
0
0.5
1
1.5
2
2.5
3
3.5
4
4.5
5
Response vs. Acquisition Time (min)

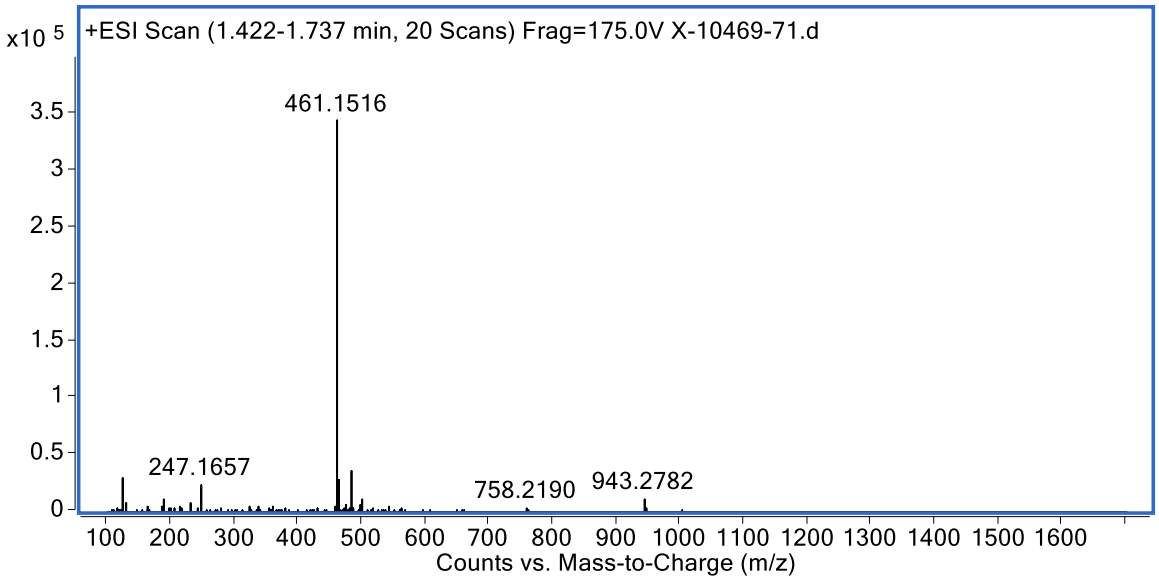
x10 5
+ESI Scan (1.422-1.737 min, 20 Scans) Frag=175.0V X-10469-71.d
461.1516
3.5
3
2.5
2
1.5
1
0.5
0
247.1657
758.2190
943.2782
100
200
300
400
500
600
700
800
900
1000
1100
1200
1300
1400
1500
1600
Counts vs. Mass-to-Charge (m/z)

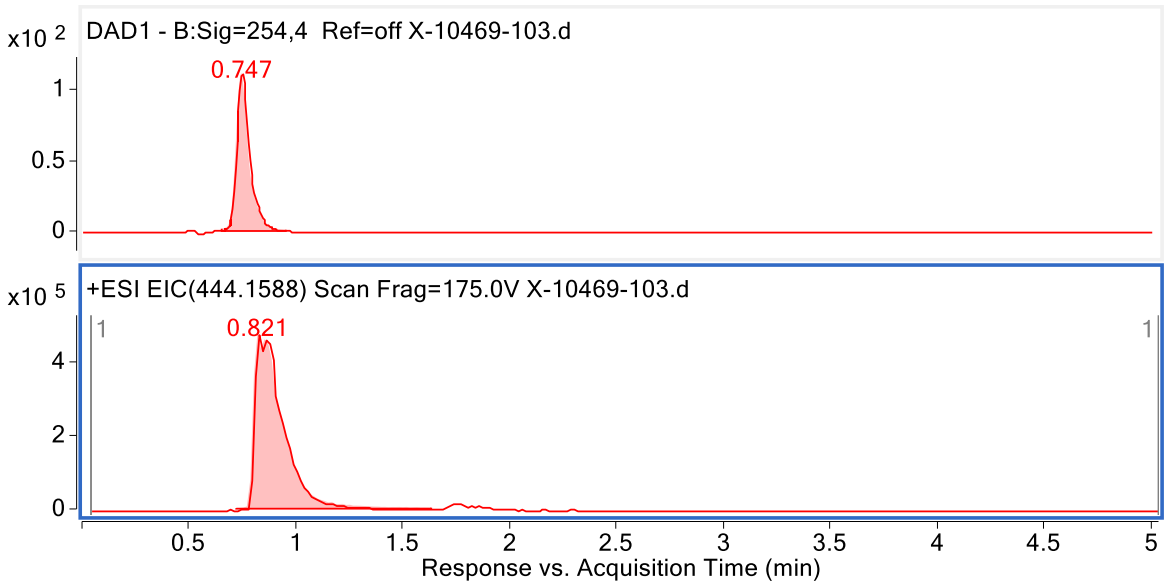
DAD1 - B:Sig=254,4 Ref=off X-10469-103.d
0.747
+ESI EIC(444.1588) Scan Frag=175.0V X-10469-103.d
0.821
Response vs. Acquisition Time (min)

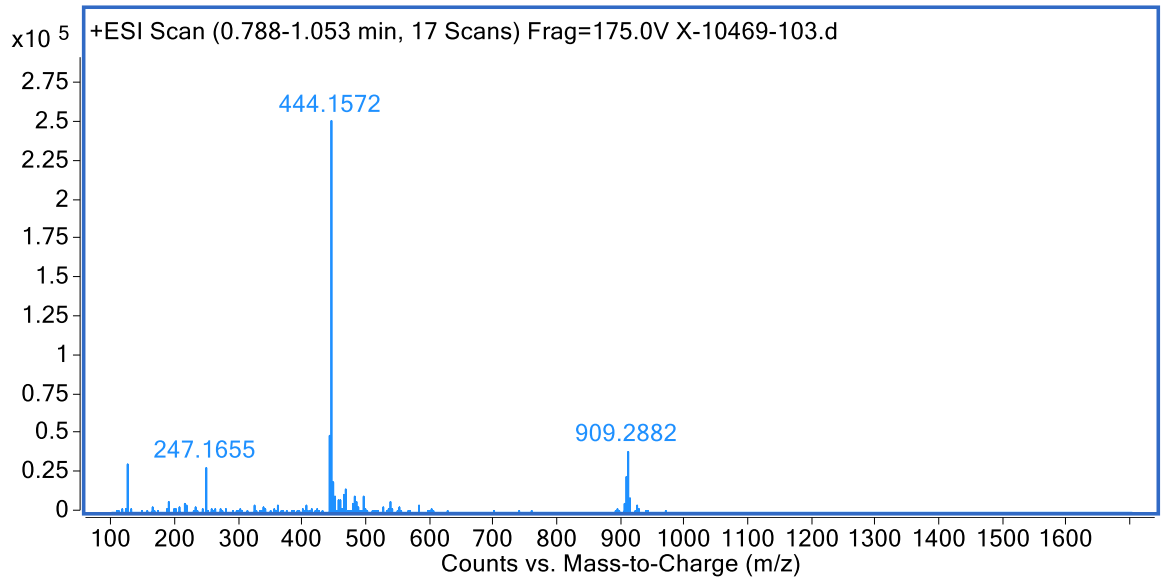
+ESI Scan (0.788-1.053 min, 17 Scans) Frag=175.0V X-10469-103.d
444.1572
247.1655
909.2882
Counts vs. Mass-to-Charge (m/z)

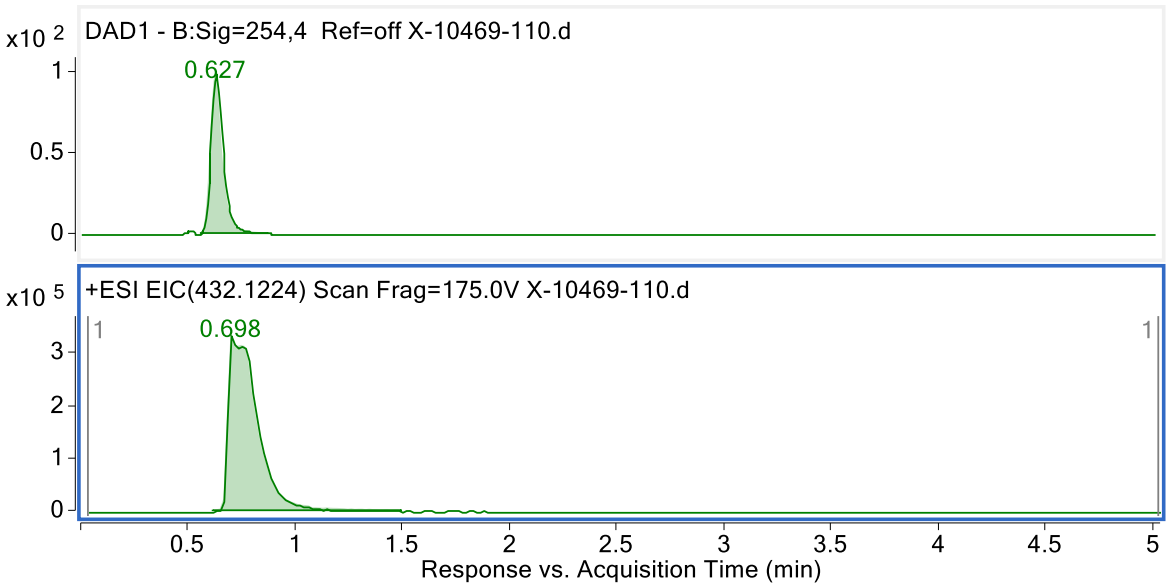
DAD1 - B:Sig=254,4 Ref=off X-10469-110.d
0.627
+ESI EIC(432.1224) Scan Frag=175.0V X-10469-110.d
0.698
Response vs. Acquisition Time (min)

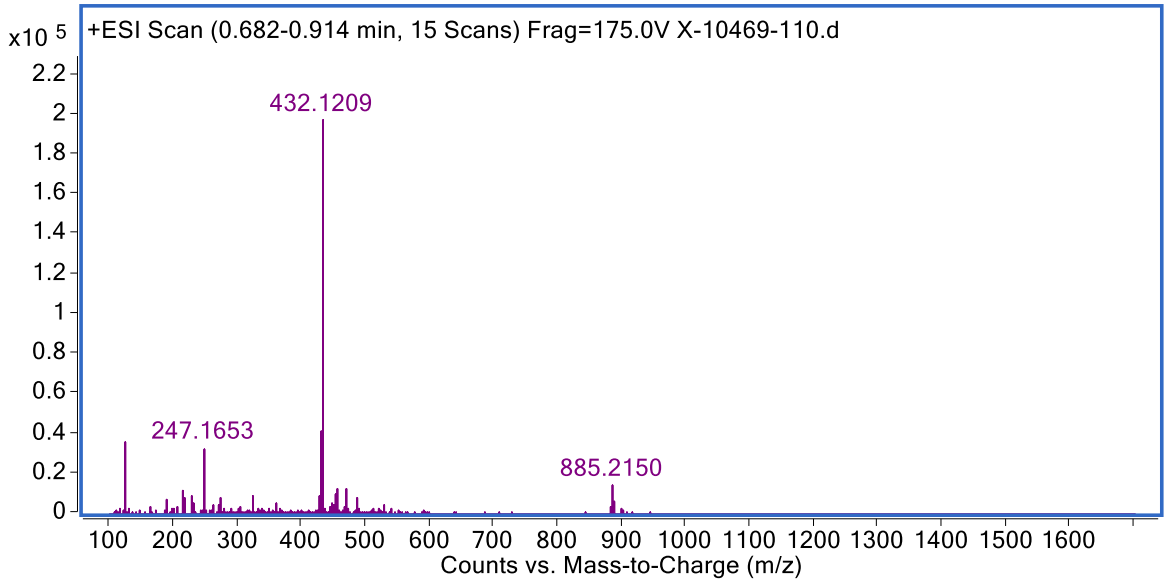
+ESI Scan (0.682-0.914 min, 15 Scans) Frag=175.0V X-10469-110.d
432.1209
247.1653
885.2150
Counts vs. Mass-to-Charge (m/z)

APPENDIX. C

All MS/MS spectra of all selected anthraquinone dyes, respective

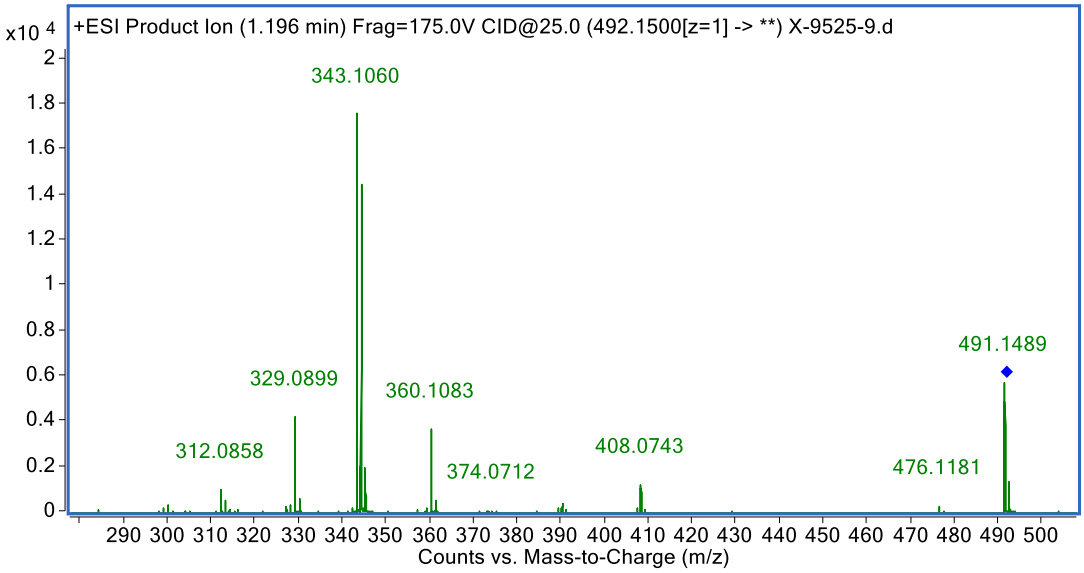

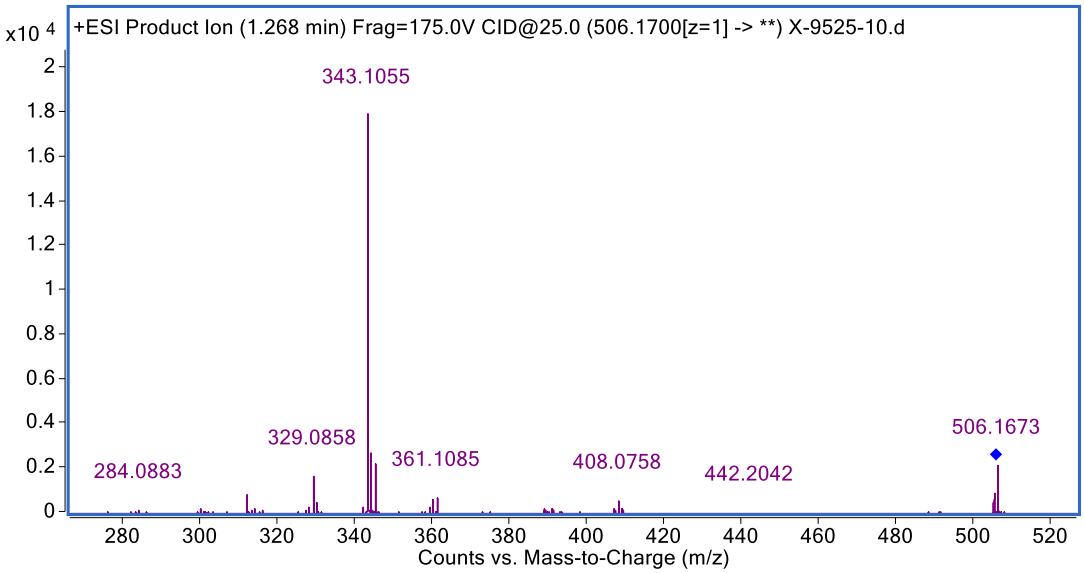

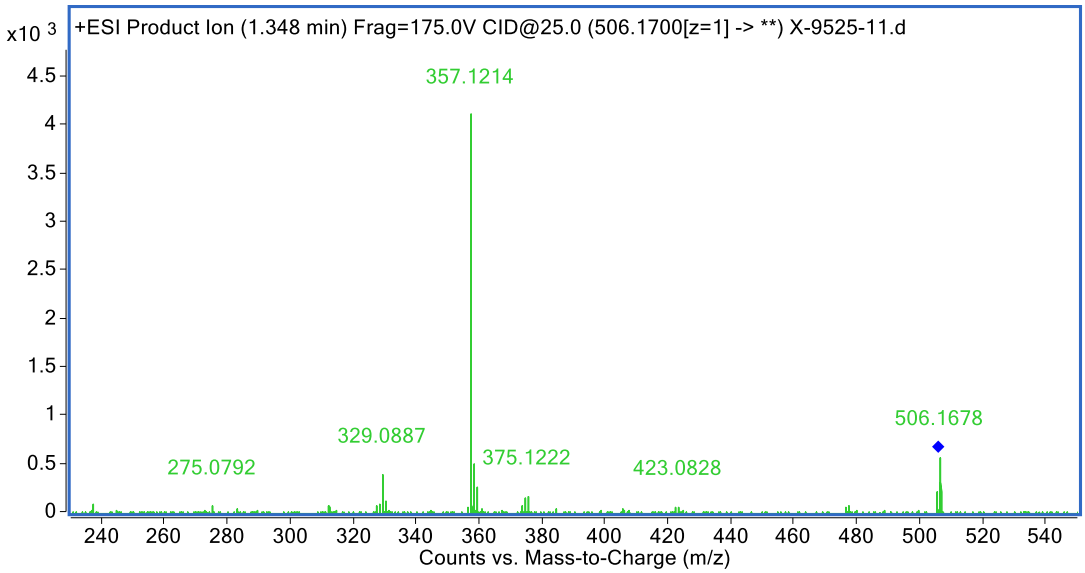
+ESI Product Ion (1.348 min) Frag=175.0V CID@25.0 (506.1700[z=1] -> **) X-9525-11.d
x10 3
357.1214
329.0887
275.0792
375.1222
423.0828
506.1678
Counts vs. Mass-to-Charge (m/z)

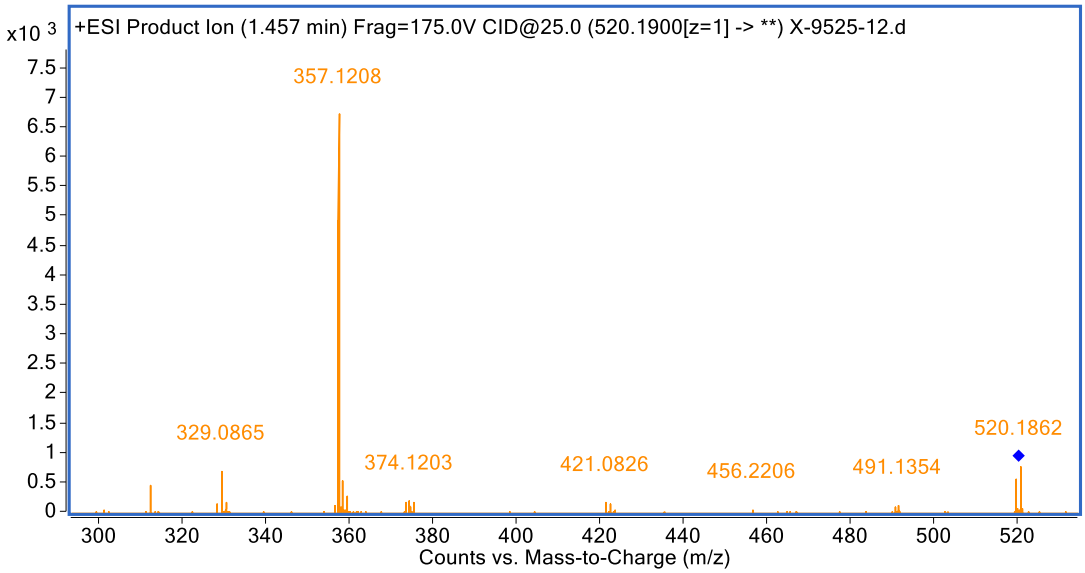
+ESI Product Ion (1.457 min) Frag=175.0V CID@25.0 (520.1900[z=1] -> **) X-9525-12.d
x10 3
357.1208
329.0865
374.1203
421.0826
456.2206
491.1354
520.1862
Counts vs. Mass-to-Charge (m/z)

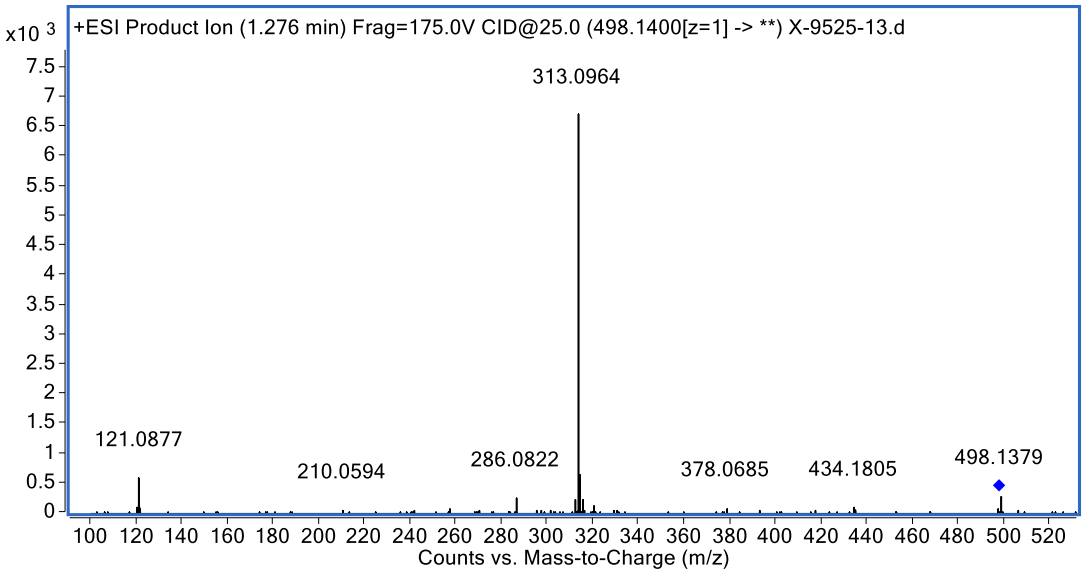
+ESI Product Ion (1.276 min) Frag=175.0V CID@25.0 (498.1400[z=1] -> **) X-9525-13.d
x10 3
313.0964
121.0877
210.0594
286.0822
378.0685
434.1805
498.1379
Counts vs. Mass-to-Charge (m/z)

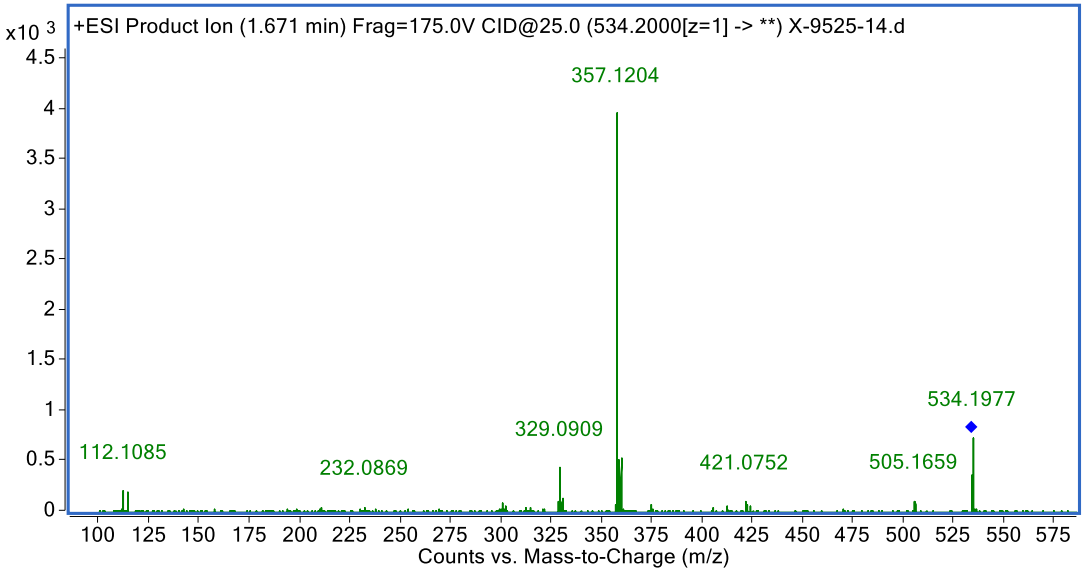
+ESI Product Ion (1.671 min) Frag=175.0V CID@25.0 (534.2000[z=1] -> **) X-9525-14.d
x10 3
357.1204
534.1977
329.0909
112.1085
232.0869
421.0752
505.1659
Counts vs. Mass-to-Charge (m/z)

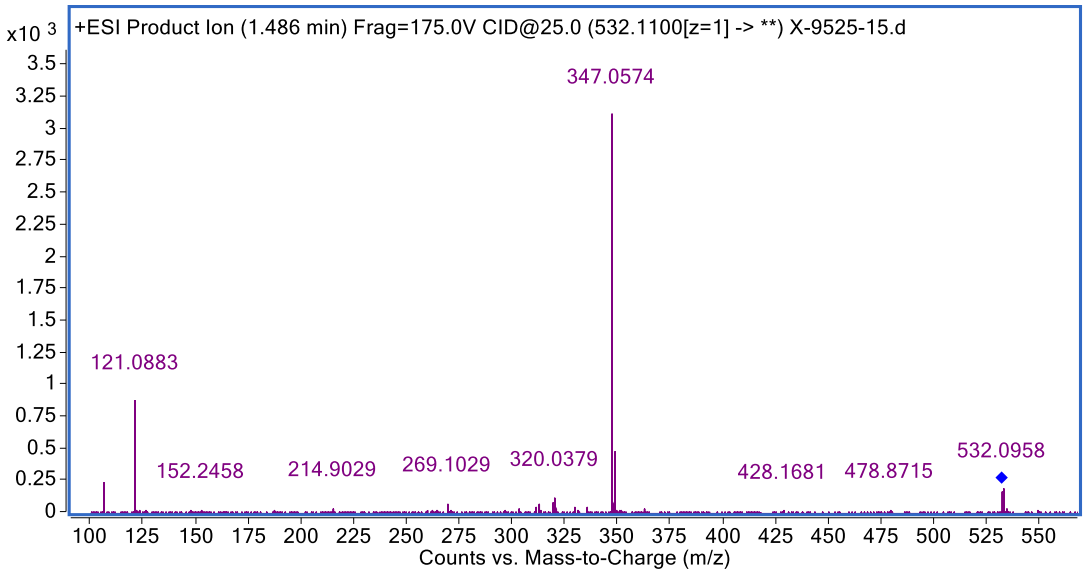
x10 3
+ESI Product Ion (1.486 min) Frag=175.0V CID@25.0 (532.1100[z=1] -> **) X-9525-15.d
347.0574
121.0883
152.2458
214.9029
269.1029
320.0379
428.1681
478.8715
532.0958
Counts vs. Mass-to-Charge (m/z)

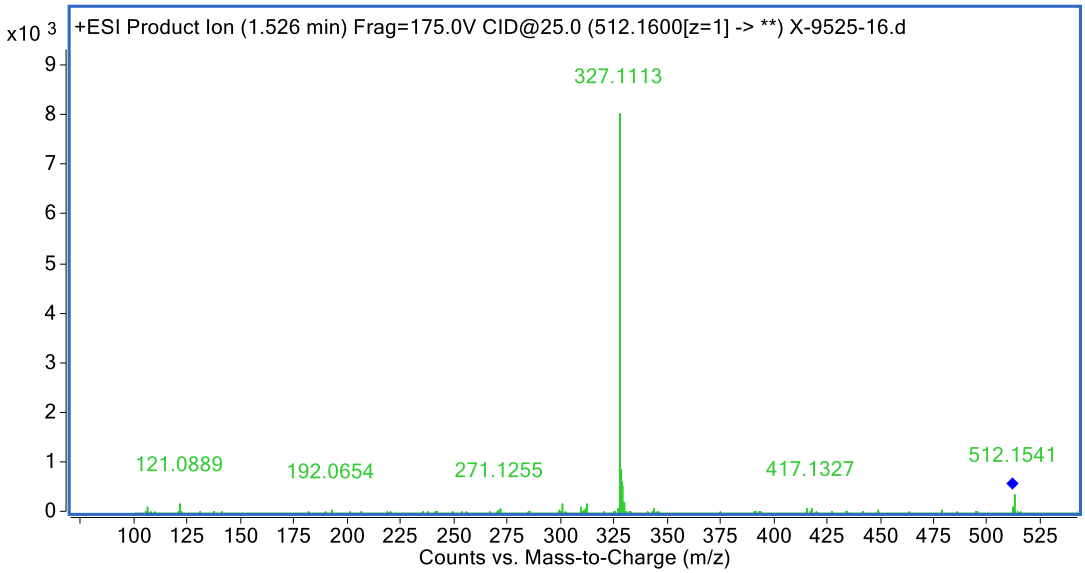
x10 3
+ESI Product Ion (1.526 min) Frag=175.0V CID@25.0 (512.1600[z=1] -> **) X-9525-16.d
327.1113
121.0889
192.0654
271.1255
417.1327
512.1541
Counts vs. Mass-to-Charge (m/z)

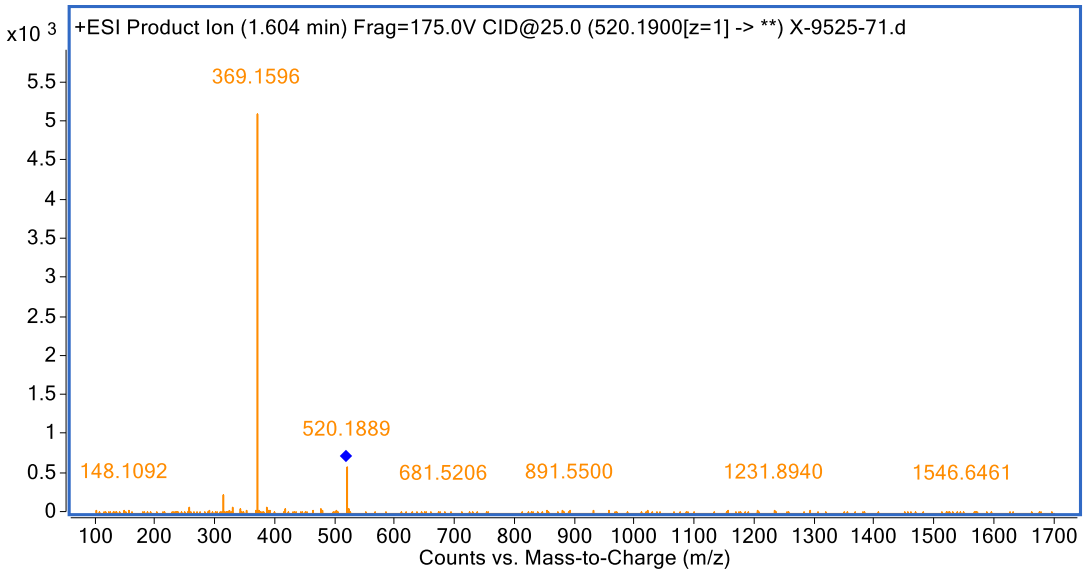
x10 3
+ESI Product Ion (1.604 min) Frag=175.0V CID@25.0 (520.1900[z=1] -> **) X-9525-71.d
369.1596
520.1889
148.1092
681.5206
891.5500
1231.8940
1546.6461
Counts vs. Mass-to-Charge (m/z)

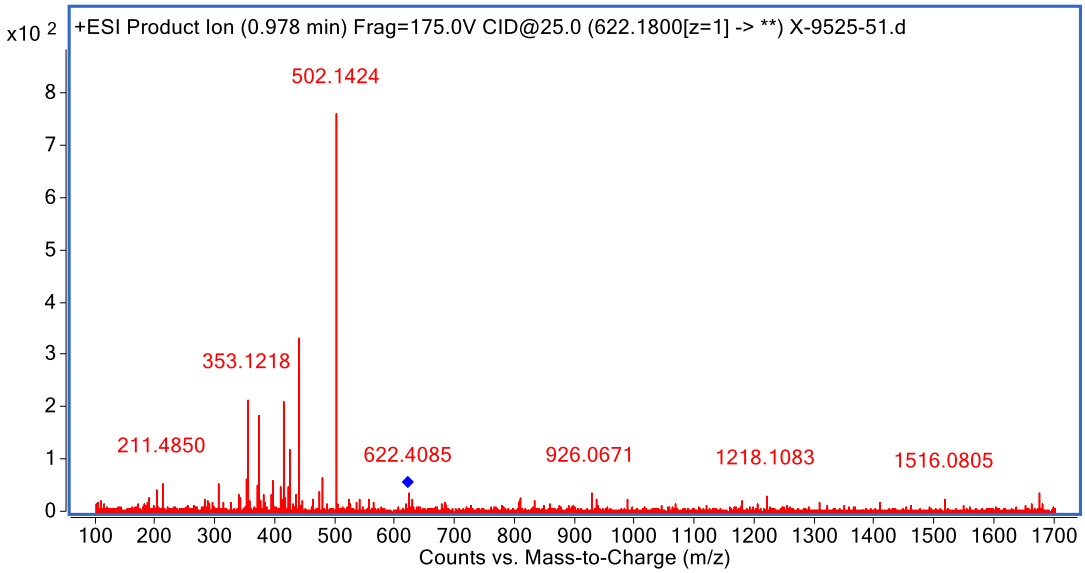
x10 2
+ESI Product Ion (0.978 min) Frag=175.0V CID@25.0 (622.1800[z=1] -> **) X-9525-51.d
502.1424
353.1218
211.4850
622.4085
926.0671
1218.1083
1516.0805
Counts vs. Mass-to-Charge (m/z)

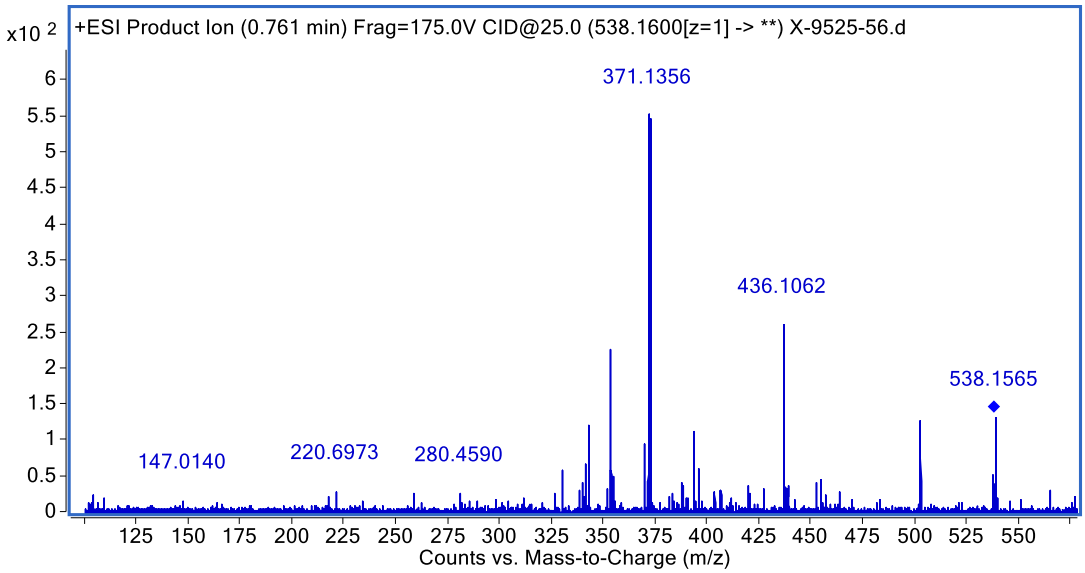
x10 2
+ESI Product Ion (0.761 min) Frag=175.0V CID@25.0 (538.1600[z=1] -> **) X-9525-56.d
371.1356
436.1062
538.1565
147.0140
220.6973
280.4590
Counts vs. Mass-to-Charge (m/z)

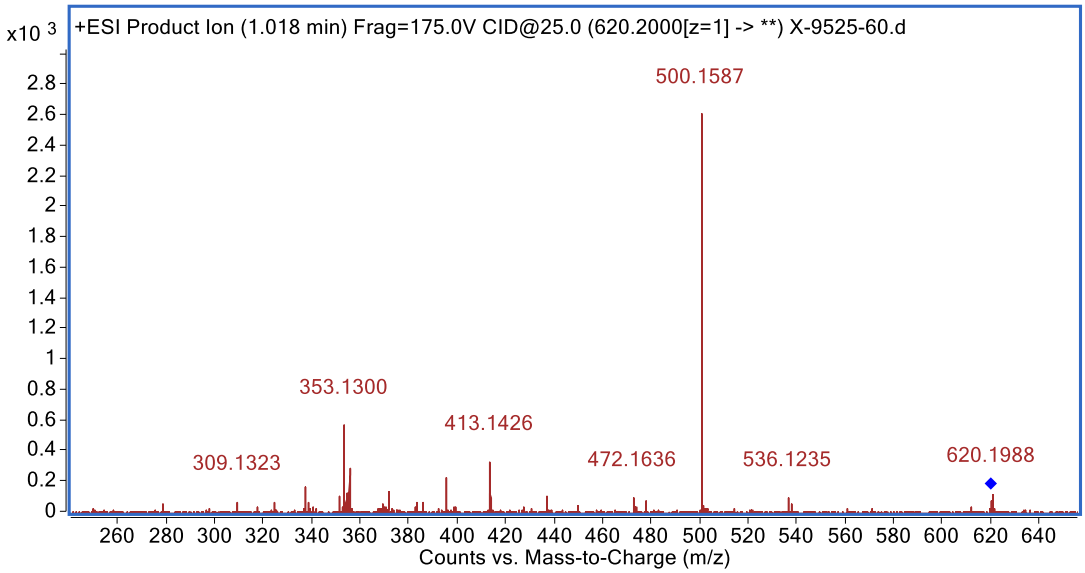
x10 3
+ESI Product Ion (1.018 min) Frag=175.0V CID@25.0 (620.2000[z=1] -> **) X-9525-60.d
500.1587
353.1300
413.1426
309.1323
472.1636
536.1235
620.1988
Counts vs. Mass-to-Charge (m/z)

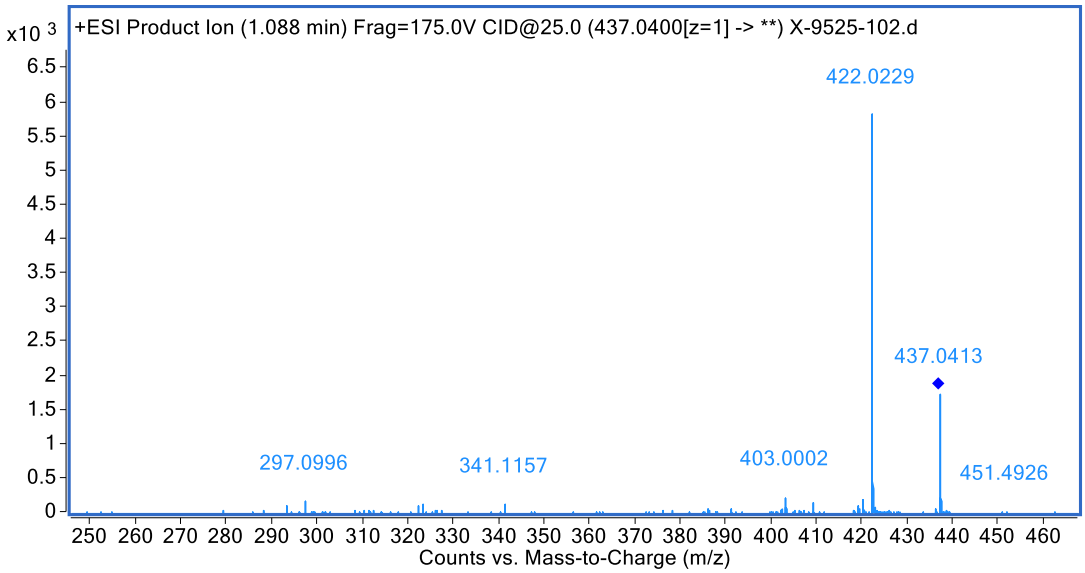
+ESI Product Ion (1.088 min) Frag=175.0V CID@25.0 (437.0400[z=1] -> **) X-9525-102.d
x10 3
422.0229
437.0413
297.0996
341.1157
403.0002
451.4926
Counts vs. Mass-to-Charge (m/z)

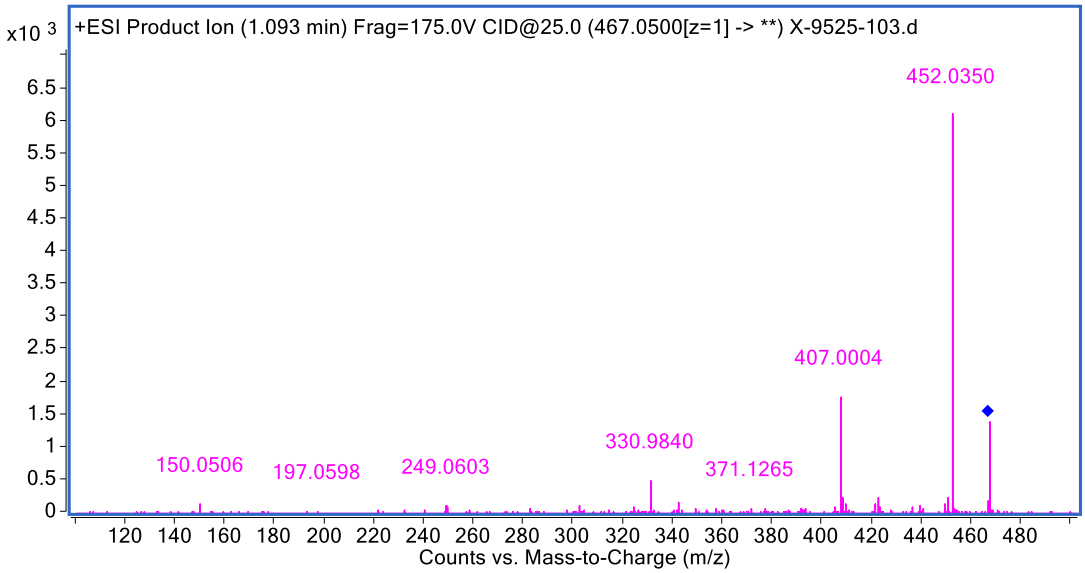
+ESI Product Ion (1.093 min) Frag=175.0V CID@25.0 (467.0500[z=1] -> **) X-9525-103.d
x10 3
452.0350
407.0004
330.9840
150.0506
197.0598
249.0603
371.1265
Counts vs. Mass-to-Charge (m/z)

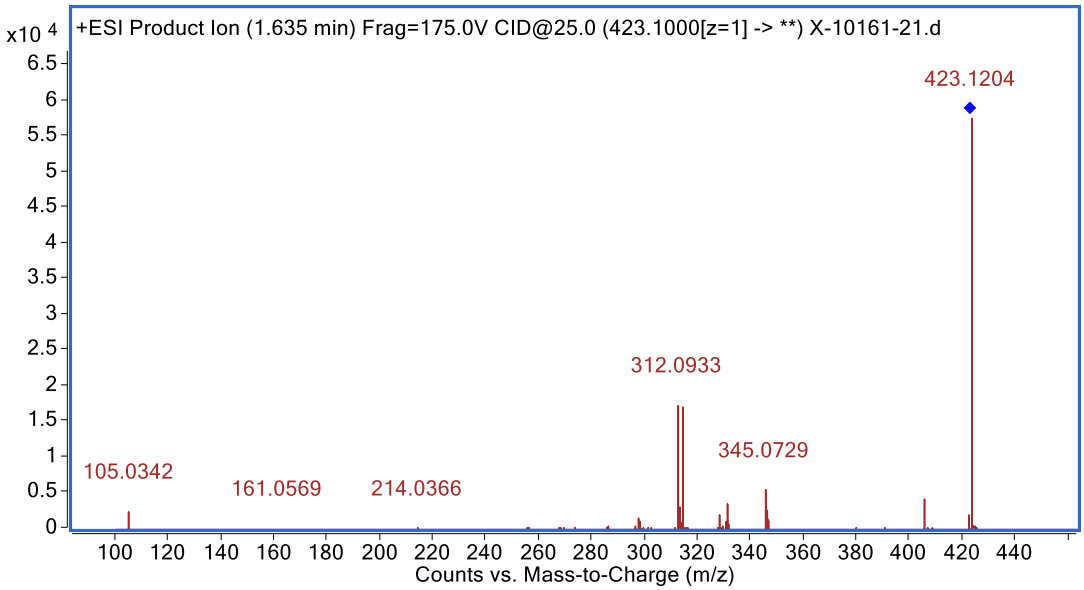
x10 4
+ESI Product Ion (1.635 min) Frag=175.0V CID@25.0 (423.1000[z=1] -> **) X-10161-21.d
423.1204
312.0933
345.0729
105.0342
161.0569
214.0366
Counts vs. Mass-to-Charge (m/z)

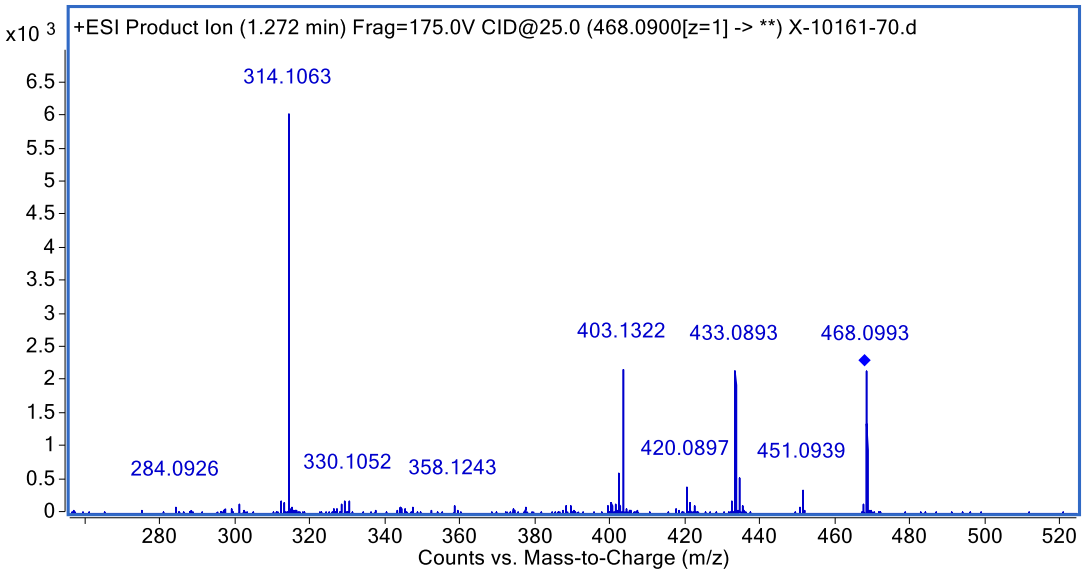
x10 3
+ESI Product Ion (1.272 min) Frag=175.0V CID@25.0 (468.0900[z=1] -> **) X-10161-70.d
314.1063
403.1322
433.0893
468.0993
420.0897
451.0939
284.0926
330.1052
358.1243
Counts vs. Mass-to-Charge (m/z)

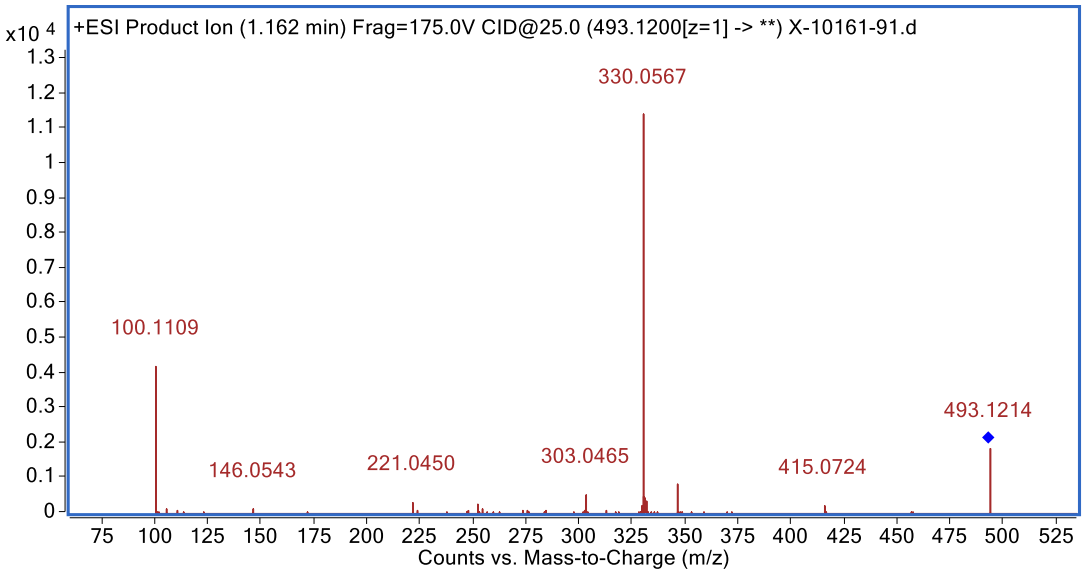
x10 4
+ESI Product Ion (1.162 min) Frag=175.0V CID@25.0 (493.1200[z=1] -> **) X-10161-91.d
330.0567
100.1109
493.1214
146.0543
221.0450
303.0465
415.0724
Counts vs. Mass-to-Charge (m/z)

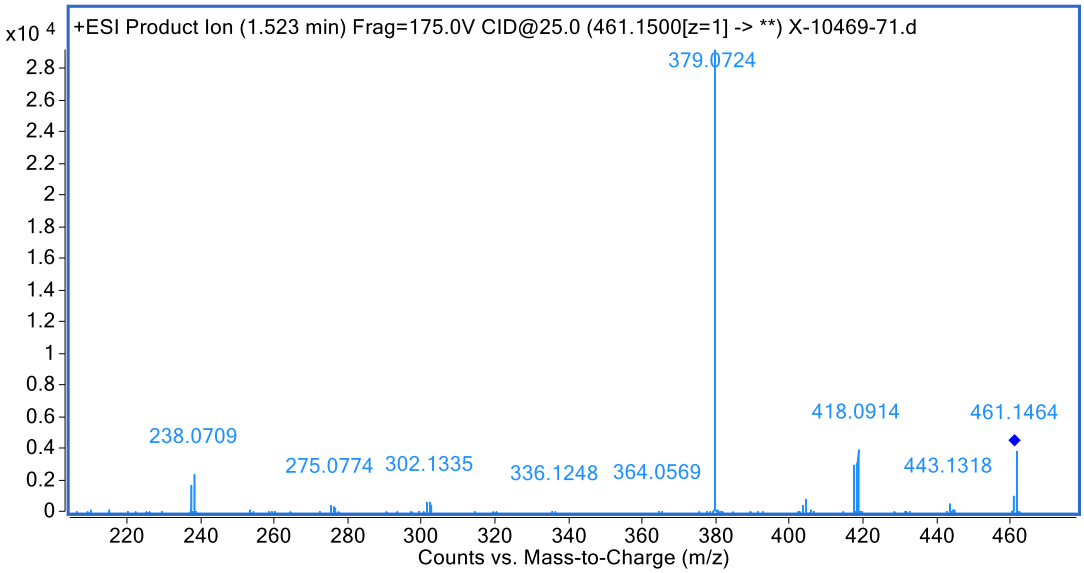
x10 4
+ESI Product Ion (1.523 min) Frag=175.0V CID@25.0 (461.1500[z=1] -> **) X-10469-71.d
379.0724
418.0914
461.1464
238.0709
275.0774
302.1335
336.1248
364.0569
443.1318
Counts vs. Mass-to-Charge (m/z)

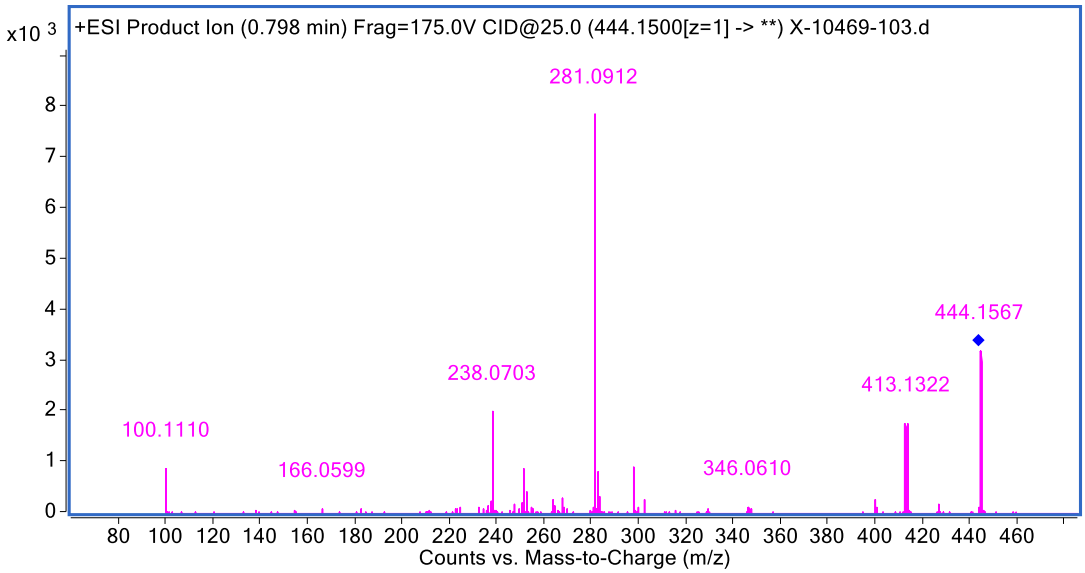
x10 3
+ESI Product Ion (0.798 min) Frag=175.0V CID@25.0 (444.1500[z=1] -> **) X-10469-103.d
281.0912
444.1567
238.0703
413.1322
100.1110
166.0599
346.0610
Counts vs. Mass-to-Charge (m/z)

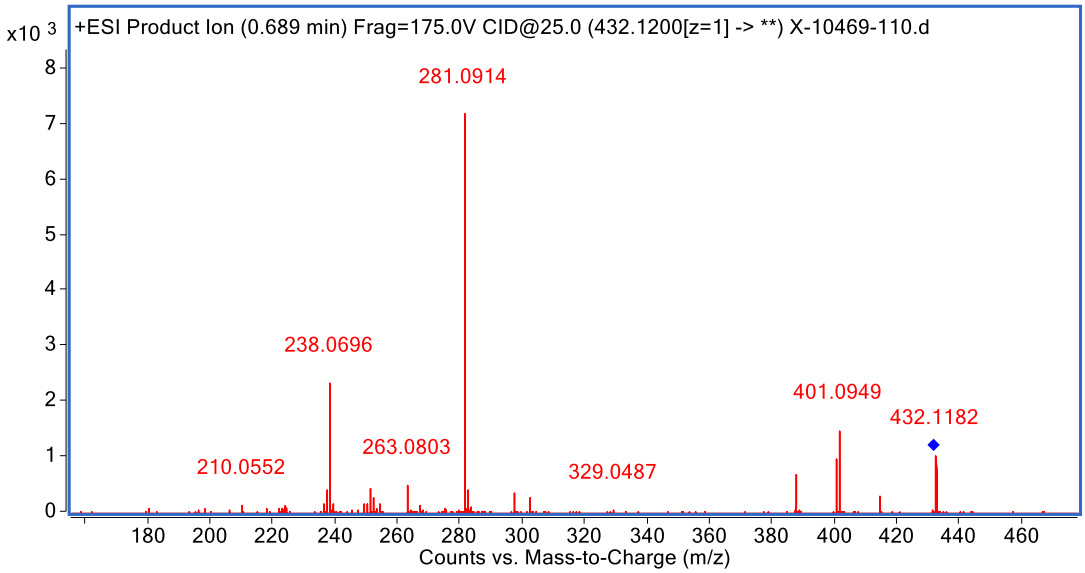
x10 3
+ESI Product Ion (0.689 min) Frag=175.0V CID@25.0 (432.1200[z=1] -> **) X-10469-110.d
281.0914
238.0696
401.0949
432.1182
263.0803
210.0552
329.0487
Counts vs. Mass-to-Charge (m/z)